ALMA MATER STUDIORUM
UNIVERSITÀ DI BOLOGNA

DOTTORATO DI RICERCA IN

FISICA

Ciclo 37

Settore Concorsuale: 02/A1 - FISICA SPERIMENTALE DELLE INTERAZIONI FONDAMENTALI

Settore Scientifico Disciplinare: FIS/01 - FISICA SPERIMENTALE

MEASUREMENT OF (ANTI)HELIUM PRODUCTION IN PP COLLISIONS WITH ALICE AT THE LHC

Presentata da: Giovanni Malfattore

Coordinatore Dottorato

Alessandro Gabrielli

Supervisore

Francesca Bellini

Co-supervisore

Nicolò Jacazio

Esame finale anno 2025

Contents

Abstract

The formation of light (anti)nuclei in high-energy hadronic collisions remains an open question under active theoretical and experimental investigation. An equal amount of matter and antimatter is produced at the LHC energies, enabling the investigation of (anti)nuclei formation mechanisms across several collision systems. However, with respect to simple nucleons, production rates for bound states are suppressed by about a factor 1000 in small systems for every added nucleon. For this reason, the currently available measurements are limited by large statistical uncertainties and poor granularity, warranting new studies focusing on the heavier states as ^{3}He and $^3\overline{\text{He}}$, a fundamental proving ground to test statistical hadronisation and coalescence models.

This work discusses the production of ^{3}He and $^3\overline{\text{He}}$ in pp collisions at $\sqrt{s} = 13.6$ TeV. The measurement is carried out using data collected by ALICE in 2022, using the first pp collisions of the Run 3 of LHC. Thanks to this wealth of data, the yield of ^{3}He and $^3\overline{\text{He}}$ is measured with unprecedented granularity, improving on the statistical precision with respect to results in literature by more than a factor 10. The challenges faced for the measurement with the new ALICE detector are detailed in this thesis.

The thesis is structured as follows. First, an introduction is given on the history of antimatter research and the critical antinuclei measurements in pp collisions; the models that describe the production of antinuclei in high-energy collisions are discussed. The repercussion of these measurements in dark matter searches with cosmic antinuclei from space-born experiments is discussed. A detailed description of the ALICE apparatus and its upgrades needed for the Run 3 is given. The techniques used to measure the (anti)nuclei production will be presented, together with the analysis rationale. In the last part of this work, the analysis will be discussed in all its steps, from the event and track selections, to the corrections applied, to the uncertainties estimation. Finally, the results will be discussed and compared with the previous measurements and expectations from the theoretical predictions from the canonical statistical model (CSM). The results of this analysis are found to be compatible with previous measurements performed during the Run 2. These results contribute to clarifying the formation mechanisms of light antinuclei, providing a precise constrain for production models, paving the road for future measurements that will, in the longer term, be used as input to the modelling for the production of cosmic antinuclei for indirect dark matter searches.

Introduction

The formation mechanism of light nuclei and antinuclei in high-energy hadronic collisions remains an open question that is being addressed both theoretically and experimentally. In particular, light (anti)nuclei are weakly-bound composite objects, held together by a binding energy of the order of a few MeV per nucleon. It is still not completely understood how they are produced in high-energy heavy-ion collisions and outlive extreme conditions in the final state, in which the average temperature, of the order of 100 MeV, is much higher than their binding energy. In particular, the study of helium-3 production (and of its antimatter partner) is a topic of great interest. Due to the heavier mass with respect to protons (or deuterons), the production of helium-3 is a million times (a thousand times) rarer and hence requires much larger data samples to be measured. For this reason, an in-depth characterisation of its production - with a precision comparable to the one reached for antideuteron at the Large Hadron Collider (LHC) in recent years - is an exciting prospective at present. Moreover, recent theoretical developments in the sector of dark matter searches have suggested that the observation of antinuclei content of cosmic rays could offer a promising channel to indirectly investigate Dark Matter existence. In this respect, the study of the (anti)helium production at colliders is fundamental as it is crucial to characterise the main background in searches for cosmic antinuclei from dark matter particle interactions, represented by hadronic interactions between primary cosmic rays and the interstellar medium, as well as to constrain light nucleus formation models. The goal of this thesis is the measurement of the (anti)helium-3 production in pp collision at $\sqrt{s} = 13.6$ TeV. A Large Ion Collider Experiment (ALICE) detector at the LHC is particularly suited to study light (anti)nuclei produced in high-energy collisions between hadrons thanks to its detectors that allow for charged-particle tracking down to low momenta and particle identification in a broad kinematic range with complementary techniques. The ALICE Collaboration has measured the production of the production of (anti)deuteron in different collision systems, providing the most comprehensive multi-differential and high-precision set of measurements to date. Despite being accessible to measurement, more data are instead needed to characterise and understand the production of heavier $A = 3$ nuclei and antinuclei. As the LHC Run 3 data taking campaign began at the end of 2021, the ALICE experiment was able to collect data of pp collisions at the record energy of $\sqrt{s} = 13.6$ TeV. In year 2022 alone, more than 500 billion minimum bias pp collisions were collected, a sample which is much larger than all the previous data taking campaigns, thus enabling the study the (anti)helium-3 production with unprecedented precision.

The first chapter of this thesis begins with a historical excursus about the discovery of antimatter, from the first observation of the positron until the discovery of $A = 4$

antinuclei in heavy-ion collisions. Part of the chapter is dedicated to the production of antinuclei in pp collisions. The second half of the first chapter introduces the motivation to search for antinuclei in cosmic rays and an overview description of the state-of-the-art cosmic antinuclei detectors.

The second chapter begins with a brief introduction to quantum chromodynamics and the properties of the phase transition of nuclear matter to quark–gluon plasma produced in high-energy heavy-ion collisions. This sets the stage for the second part of the chapter, which introduces two of the most popular (anti)nuclei formation models - the statistical hadronisation models and the coalescence model - and the main observables to characterise the (anti)nuclei formation and compare models: the coalescence parameter and the ratio between (anti)nuclei yield and the nucleons yield.

The third chapter is dedicated to the ALICE experiment, after a brief introduction to the LHC and the CERN accelerator complex. The ALICE apparatus design and performance are discussed in details. An extensive portion of the chapter is dedicated to the upgrades that the ALICE apparatus underwent between Run 2 and Run 3.

The fourth chapter introduces the techniques used to perform (anti)nuclei identification used in this analysis. The analysis is performed with the Time Projection Chamber (TPC) detector, which identifies the particles through measurements of loss of energy in the material ($\mathrm{d}E/\mathrm{d}x$), and with the Time-Of-Flight (TOF) detector, which identifies the particles through measurements of the particle time-of-flight. The chapter describes the particle identification methods that are used with these detectors in details.

The fifth chapter eventually describes the analysis work in its whole. The chapter lists the choices performed to select events and tracks, the process of measurement - which uses the techniques introduced in the previous chapter - and the corrections needed to estimate the production yield of (anti)helium. The results of the work are finally presented, commented in detail and compared with the theoretical predictions discussed in the second chapter.

Chapter 1

Light antinuclei

Antinuclei are defined as the antimatter partners of ordinary nuclei. The concept of antimatter is introduced in Section 1.1, from its discovery to the measurements of the production of light antinuclei in particle accelerators at different energies and with different colliding systems, up to the highest collision energies in reach nowadays at the CERN Large Hadron Collider (LHC). At particle accelerators, the study of light antinuclei is fundamental to understand properties of matter and antimatter, as well as to investigate their formation mechanisms. On the other hand, searches for light antinuclei heavier than antiprotons in cosmic rays have been carried out since few decades with space-borne and air-borne experiments. The relevance of these searches for indirect searches for Dark Matter particle candidates is discussed in Section 1.3, together with an overview of the most relevant experiments for this purpose.

1.1 The discovery of antimatter

The existence of antimatter is known since the 1930s. Before the discovery, its existence was questioned for more than thirty years. The word *antimatter* has been introduced by Arthur Schuster in a letter [1] sent to *Nature* and was used to describe a hypothetical state of matter that possessed a *negative gravitational attraction* and could annihilate with ordinary matter. Schuster's idea reflected the needs of his times to investigate the (Newtonian) gravity effects on atoms and molecules in a period of time in which electrodynamics and statistical mechanics were at the peak of their classical descriptions.

The modern physical hypothesis of antimatter is due to Paul Adrien Maurice Dirac [2]. In 1926, the Klein-Gordon equation [3] combined the non-relativistic quantum description for particles introduced by Schrödinger with the relativistic energy of bodies introduced by Einstein. Let's now introduce the Schrödinger wave equation for a quantum particle $\psi(\vec{x}, t)$ of mass m. If we consider the energy acting on a particle written via differential operators

$$E \rightarrow -\frac{\nabla^2}{2m} + V(\vec{x}, t)\,, \tag{1.1}$$

the Schrödinger equation for the wavefunction ψ is

$$\left(i\frac{\partial}{\partial t} + \frac{\nabla^2}{2m}\right)\psi(\vec{x}, t) = V(\vec{x}, t)\,. \tag{1.2}$$

If the relativistic energy $E^2 = p^2 + m^2$ is introduced, the Klein-Gordon equation for a free spin 0 particle can be written as

$$\left(\nabla^2 - \frac{\partial^2}{\partial t^2}\right)\psi(\vec{x}, t) = m^2\psi(\vec{x}, t) \quad . \tag{1.3}$$

The equation presents issues as it is not linear in ∂t, as required by the Schrödinger equation. Additionally, it admits negative energy solutions

$$E = \pm\sqrt{p^2 + m^2}\,, \tag{1.4}$$

which can be explained as related to negative probability density states $\rho = |\psi|^2 < 0$. This is not allowed within the Copenhagen interpretation of quantum mechanics and has remained an unsolved question for a couple of years. Also, the equation could not correctly describe particles with half-integer spin.

In 1928, Pauli found an alternative solution to this problem. He wrote a relativity-consistent formulation of the Hamiltonian - which describes the energy of a system, starting from the premise that it has a quadratic dependence on momentum. He factorised the eigenvalue of the Hamiltonian, the relativistic energy $E^2 = p^2 + m^2$, using the covariant formalism and the four-momentum $p^\mu = (E, \vec{p})$, he wrote an equation [3] based on the covariant formalism:

$$p^\alpha p_\alpha - m^2 = (\gamma^\lambda p_\lambda + m)(\gamma^\mu p_\mu - m) = 0 \tag{1.5}$$

where γ^λ are 4×4 matrices (*gamma matrices*):

$$\gamma^0 = \begin{pmatrix} 1 & 0 \\ 0 & -1 \end{pmatrix}, \qquad \gamma^i = \begin{pmatrix} 0 & \sigma^i \\ -\sigma^i & 0 \end{pmatrix} \tag{1.6}$$

where σ^i are the known Pauli matrices. Through the use of the gamma matrices notation, the Dirac equation can be written in a covariant form:

$$(i\gamma^\mu\partial_\mu - m)\psi = 0 \tag{1.7}$$

where ψ is the four-component wave function called *Dirac spinor* and ∂_μ is the four-gradient operator. The equation has two positive solutions that correspond to the two $\pm 1/2$ spin states of fermions. As in the Klein-Gordon equation, the Dirac equation has two negative energy solutions, but if the associated current

$$j^\mu = \overline{\psi}\gamma^\mu\psi \tag{1.8}$$

is expressed as a contravariant four-vector $j^m = (\rho, j^i)$, the first component of the current, the probability density, is defined always positive, as

$$j^0 = \rho = \overline{\psi}\gamma^0\psi = \Sigma_1^4|\psi_i|^2 \tag{1.9}$$

which is compatible with the Copenhagen interpretation of quantum mechanics. For this reason, the negative energy solutions cannot be disregarded as they contribute to a complete set of states. The details of Dirac's interpretation of the existence of these states (*Dirac's*

sea) exceeds the bounds of this thesis (and also it introduced issues - like the infinite negative charge of the Universe - that only the modern quantum field theories can correctly handle), but his solution implied that there must be a particle with an opposite charge with respect to that of the electron: at the beginning, Dirac hypothesised this particle to be the proton. However, this option had to be soon discharged due to its mass. Robert Oppenheimer and Hermann Weyl showed that the mass of this hypothetical particle had to be comparable with the electron mass. In a very short time, Dirac and the scientific community of the time proposed the existence of an *antielectron*, an *antiparticle* that differed from the ordinary electron only for the electric charge.

The discovery of the positron The discovery of the positron (the antimatter version of the electron) happened in 1932 by Carl David Anderson [4]. Anderson designed a cloud chamber with the purpose of measuring the energy of cosmic ray particles (travelling at speed v). The cloud chamber (also known as the Wilson chamber) was equipped with a lead plate for decelerating the cosmic rays and was immersed in a magnetic field (B) to deflect the particles according to the charge (e). According to the curvature, it is possible to determine the kinetic energy of the particle as it enters the bubble; the curvature radius ($R = \frac{mv}{eB}$) decreases as the particle loses energy via ionisation in the gas. Anderson observed a track compatible with a particle of 300 keV energy and positive charge (Fig. 1.1): the track could not have been left by a proton, as the observed track was 10 times longer than the one expected from a 300 keV proton. According to Anderson, the particle had to be the hypothesised antielectron, named after its discovery, the *positron*.

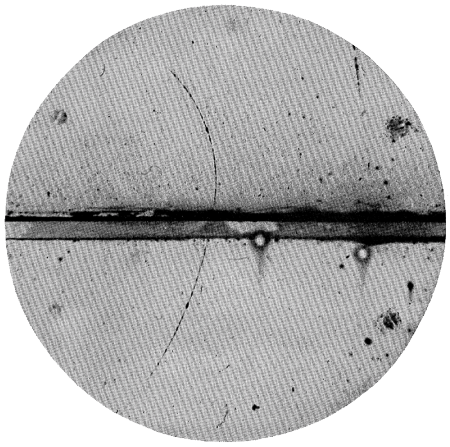

Figure 1.1: A 63 MeV positron passing through a 6 mm lead plate and emerging as a 23 MeV positron, as shown in C. D. Anderson paper [4].

The discovery of the antiproton Anderson's experiment opened an era of new antiparticle discoveries. In 1955, at the Berkeley National Laboratory (LBNL), Owen Chamberlain and Emilio Segré conducted an experiment that observed 60 candidates with the same mass of the proton and opposite charge: the antiprotons [5]. The antiprotons had been produced using the Bevatron accelerator, a weak-focusing synchrotron that produced 6.2 GeV proton

beams and made them collide into a fixed copper target. Chamberlain and Segré estimated that the energy threshold to obtain the production of an antiproton in a proton-nucleon collision was about 4.3 GeV, assuming a target with a Fermi energy of around 25 MeV, and therefore it was kinematically allowed. The detector was placed after the copper target, and it was built using deflecting and focusing magnets, several plastic scintillators and two different types of Cherenkov counters, as seen in Fig. 1.2 a. The detector counted the particles produced via spallation on the target, mainly (negative) pions and reconstructed the masses of the measured particles. A few candidates had a mass compatible with the proton one (Fig. 1.2 b) and opposite charge. The ratio of this candidate production relative to that of pions was extremely low (1/44000).

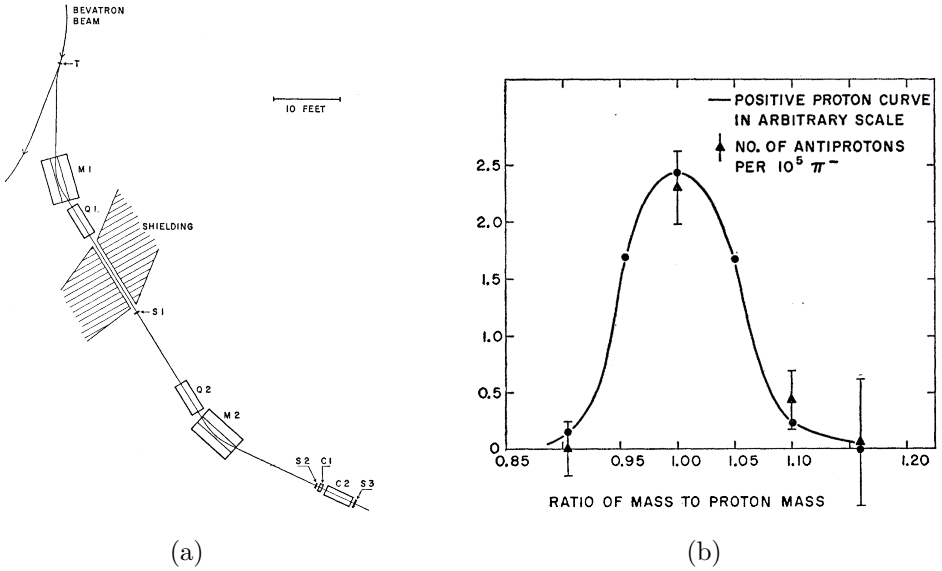

(a) (b)

Figure 1.2: (a) Diagram of the experimental apparatus arrangement at Bevatron. (b) Ratio of measured (antiproton) mass to proton mass. The solid curve is the mass resolution of the apparatus as obtained with protons. The black dots are the experimental points.

The discovery of antideuteron The discovery of the antiproton after the positron greatly impacted the particle physics of its times, as it showed the existence of antiparticle counterparts for both leptons and hadrons. At this point, the existence of antimatter made of antinuclei (and eventually positronic orbitals) was a strongly supported hypothesis. It became rapidly one of the main topics of the scientific community. The existence of the antiprotons was an important hint of the fundamental invariance of the law of physics for the antiparticles, as the CPT invariance was under discussion because of the discovery in 1964 of the CP violation by Cronin & Fitch after the first observation by Chien-Shiung Wu in 1956. The idea of testing the fundamental interactions on these newly discovered antiparticles was thrilling, and researching a bound state of an antiproton and a hypothetical *antineutron*, forming an antideuteron via the strong interaction, was the immediate next step.

The first antinuclei artificially produced were discovered independently in 1965 by a group led by Antonino Zichichi using the Proton Synchrotron (PS) at CERN [6] and by a group directed by Leon Ledermann and Samuel C. C. Ting using the Alternating Gradient Synchrotron (AGS) at the Brookhaven National Laboratory (BNL), New York [7, 8].

The group at CERN used a beam of protons accelerated by the PS up to a momentum $p = 19.2$ GeV/c, impinging on a 1 mm depth beryllium fixed target [6]. The momentum (and velocity) of the charged particles produced via spallation were measured using bending magnets and an electrostatic separator, allowing us to determine the mass spectrum of the produced particles. The collected particles were subsequently analysed using ethylene-filled Cherenkov counters and time-of-flight counters. The setup used for the measurement is shown in Fig. 1.3 a. In Fig. 1.3 b the candidate signal peak measured by the electrostatic separator is shown. The experiment collected candidates with a mass $m = (1867 \pm 80)$ MeV/c^2 and negative charge (determined by the track bending), compatible with the antideuteron hypothesis. The measured antideuteron-over-pion ratio was 8×10^{-9}, three orders of magnitude smaller than the previously measured antiproton-over-pion ratio.

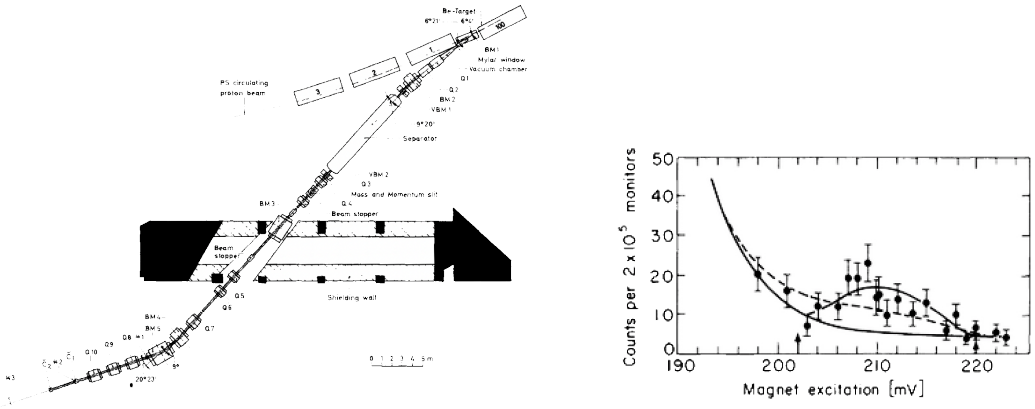

(a) (b)

Figure 1.3: (a) The setup of the PS experiment at CERN of Zichichi *et al.* [6] (b) The antideuteron signal as a peak measured by the electrostatic separator.

The group at Brookhaven accelerated protons using the AGS onto a beryllium fixed target [7, 8]. The beam was tuned to have a momentum range of $p = 4.5 - 6$ GeV/c. The experimental apparatus was composed of a group of seven magnets, additional magnetic quadrupoles, Cherenkov counters and a set of time-of-flight detectors. The results of the measurements are partially shown in Fig. 1.4. The experiment was able to observe particles with a negative charge and a mass of $m = 1.86$ GeV/c^2. The same experiment also looked for antitriton candidates (the antimatter counterpart of triton, formed by one proton and two neutrons) produced using an iron target, but none were found.

The discovery of A = 3 antinuclei The first antinuclei with $A = 3$ (where A is the *atomic number*, the number of nucleons that form a nucleus) were discovered a few years later. In 1970, the first antihelium-3 ($^3\overline{\text{He}}$) nuclei were produced using the U-70 accelerator at Serpukhov, Russia [9]. The U-70 accelerator was a 1480 m long synchrotron that held

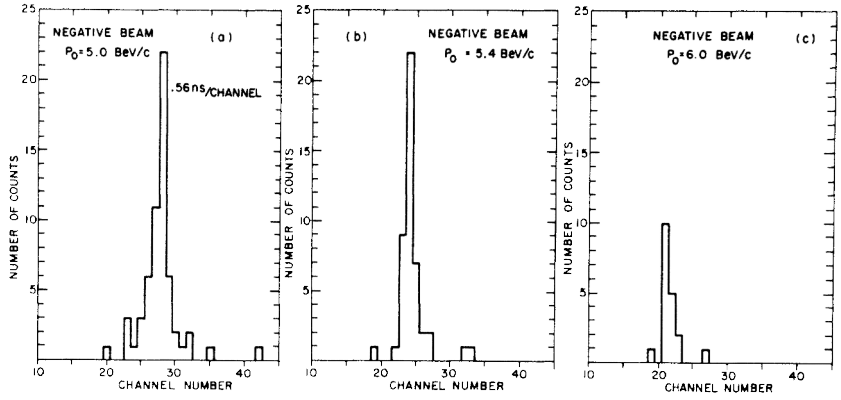

Figure 1.4: Time-of-flight spectra between Cherenkov counters for candidates of the indicated momenta, taken in consecutive runs collected at the BNL [8].

the world record in beam energy at the time of its commissioning, and today, it still holds the status as the highest energy accelerator in Russia. It was able to accelerate protons in pulse mode up to 76 GeV. The group of Antipov *et. al.* estimated that the $^3\overline{\mathrm{He}}$ (and antitritium) production threshold in pp collisions was 28 GeV. The U-70 accelerator was used to produce 70 GeV proton beams and made them collide with an aluminium target. The experimental layout is shown in Fig. 1.5. The four main groups of detectors were spectrometric scintillation counters, gas threshold counters, gas Cherenkov differential counters and time-of-flight detectors.

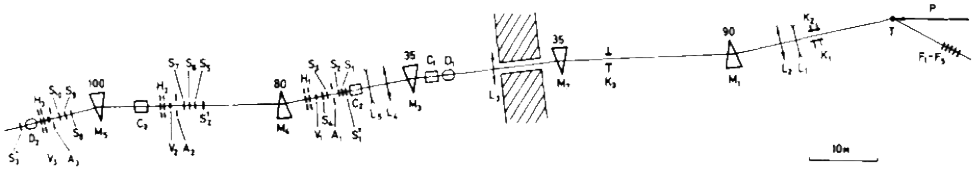

Figure 1.5: The setup of the U-70 experiment at the Institute for High Energy Physics (IHEP) of Serpukhov (Protvino) [9].

An extensive set of measurements of the charge of the particle by ionisation loss in

scintillation counters and by Cherenkov light intensity using differential counters was made: the expected values of these quantities are proportional to the charge squared, so for $^3\overline{\mathrm{He}}$ signal is 4 times bigger with respect to unitary charged particles. The experiment identified 5 $^3\overline{\mathrm{He}}$ among 2.4×10^{11} particles measured. The candidates had a mass of $m = 3 \times (1.00 \pm 0.03)\ m_p$ and charge $q = +2 \times (0.99 \pm 0.03)\ e$, where m_p is the mass of the proton and e is the charge of the electron.

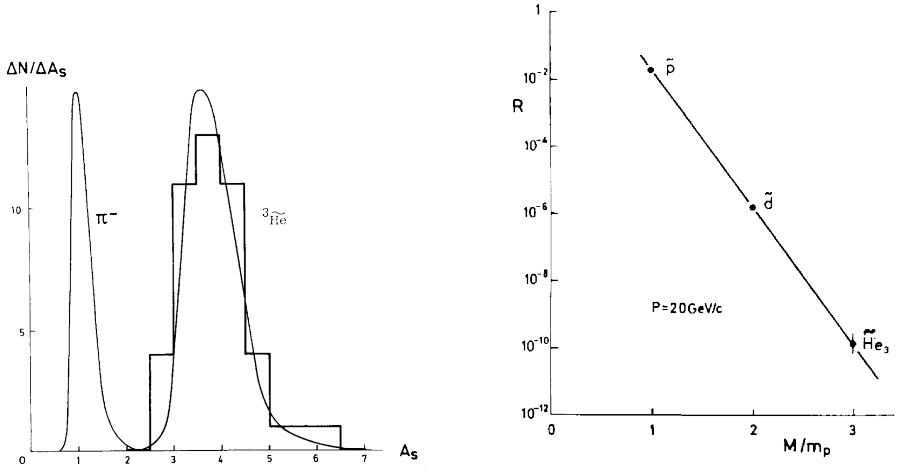

(a) (b)

Figure 1.6: (a) Pulse-height spectrum in the spectrometric counters for the identified $^3\overline{\mathrm{He}}$. (b) The rate of antiparticle production at $p = 20$ GeV/c as a function of M/m_p showing an exponential suppression with the increase of mass number.

The group at Serpukhov, guided by N.K. Vishnevsky, discovered the antitriton in 1974, measuring the first 4 antitritons observed [10]. After the work of Vishnevsky and the observations of the antitriton, the discoveries of antinuclei produced at proton accelerators in pA collisions reached a stall and no new species was discovered. Nevertheless, the quest for understanding the production mechanisms of antinuclei and the research for new antimatter candidates were still extremely popular topics in particle physics. In 1979, Golden *et. al.* [11] reported the first evidence for antiprotons in cosmic rays: it appeared clear that antimatter studies had applications way beyond the fundamental physics study, such as in cosmology and astrophysics. In Section 1.3, more about the state-of-the-art searches for antimatter in cosmic rays will be discussed.

The discovery of the anti-alpha particle At the end of the 1970s, it appeared clear that to better study the properties of antimatter, the production yield had to be dramatically increased. The limitations of the state-of-the-art technology of those times made it impossible for fixed target machines to improve the production yields by order of magnitudes. The first solution was found at the beginning of the 1980s with the upgrade of two of the main proton accelerators, the AGS and the PS, adding the capability to accelerate heavy ions. The team at AGS was able to collide ^{197}Au ions (gold-gold collisions) with a center-of-mass energy per nucleon pair of $\sqrt{s_{\mathrm{NN}}} = 4.8$ GeV. The PS group instead

was able to accelerate ^{208}Pb ion (lead-lead collisions) with a center-of-mass per nucleon pair of $\sqrt{s_{\mathrm{NN}}} = 17$ GeV. Further researches were performed eventually by the NA49 [12] experiment at CERN in Pb–Pb collision with $\sqrt{s_{\mathrm{NN}}} = 17.2$ GeV using the Super Proton Synchrotron (SPS) accelerator. This first phase of heavy-ion collision physics was extremely important and allowed the first observation of new states of matter. The NA50 experiment (also named Dimuons Collaboration) at the SPS used $\sqrt{s_{\mathrm{NN}}} = 18$ GeV Pb–Pb collisions to investigate the nuclear matter under extreme conditions of energy density, with the goal of detecting signals of a phase transition from ordinary matter to a plasma of deconfined quarks and gluons, the quark-gluon plasma (QGP, see more details in Section 2.1). At the beginning of the 2000s, a dedicated heavy-ion collider at BNL, the Relativistic Heavy Ion Collider (RHIC) began its operations, with four experiments displaced along its ring: BRAHMS, PHENIX, PHOBOS and STAR [13]. The STAR apparatus layout is shown in Fig. 1.7. The RHIC operations began with Au–Au collisions up to $\sqrt{s_{\mathrm{NN}}} = 200$ GeV and eventually included Pb–Pb collisions at $\sqrt{s_{\mathrm{NN}}} = 193$ GeV.

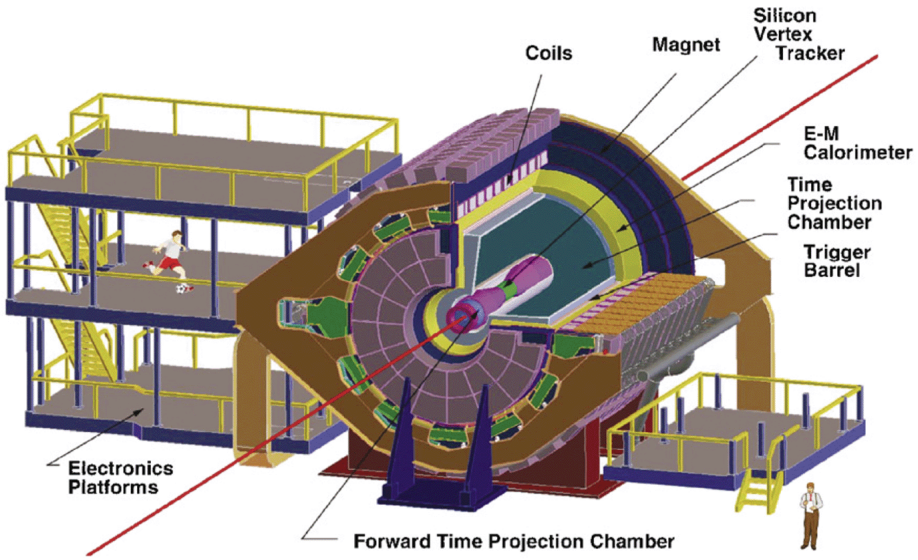

Figure 1.7: Layout of the STAR apparatus [13].

The ultimate goal of the physics programme at RHIC was to study the QGP produced in heavy-ion collisions [14, 15], but the experiments allowed for the discovery of new states of antimatter and the study of their properties. One of the first observations made by the STAR Collaboration was that antideuteron and antihelium-3 production rates are dependent on the energy [16]. A fundamental discovery by the STAR collaboration was the first observation of antinuclei with A = 4, namely the antihelium-4 ($^4\overline{\mathrm{He}}$, or anti-alpha particle or $\overline{\alpha}$). The first 18 antihelium-4 candidates ever observed were produced in $\sqrt{s_{\mathrm{NN}}} = 200$ GeV Au–Au collisions [17]. The candidates were identified using both the STAR Time Projection Chamber (TPC) and STAR Time-Of-Flight (TOF) detector, following a procedure very similar to the one described in Section 4.2. In Fig. 1.8, the average specific energy loss ($\langle \mathrm{d}E/\mathrm{d}x \rangle$) for charged particles measured by the STAR TPC

is reported. The negative (positive) helium candidates are plotted in blue (orange) as a function of the rigidity ($p/|Z|$). The black lines are the expected distribution according to the Bethe-Bloch equation.

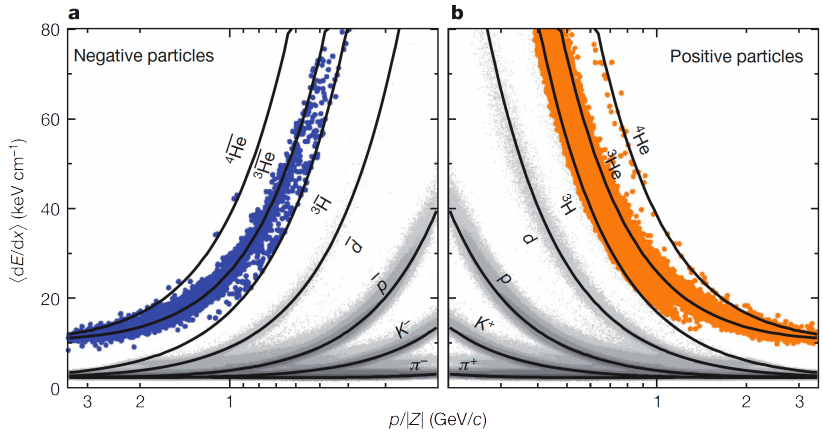

Figure 1.8: $\langle \mathrm{d}E/\mathrm{d}x \rangle$ versus $p/|Z|$ measured in the STAR TPC detector [17]. The black lines represent the expected $\langle \mathrm{d}E/\mathrm{d}x \rangle$ values according to the Bethe-Bloch distributions.

Data from STAR allowed for the study of production of light (anti)nuclei as a function of the baryonic number, confirming up to $A = 4$ the exponential dependence of the yields already observed in previous experiments up to $A = 3$ (Fig. 1.6), later also confirmed at the LHC (see Section 1.2).

1.2 Antinuclei from pp collisions

At the beginning of the 1970s, the search for hadrons heavier than protons produced in pp collisions was being carried out mostly at CERN, at the Intersecting Storage Rings (ISR) [18, 19], the world's first hadron collider. There, the antideuteron production cross section was measured in pp collisions at $\sqrt{s} = 45$ and 53 GeV at low transverse momentum, reported in Fig. 1.9 (left). The measurements suffered from large statistical uncertainties, and led to the measurement of a $\mathrm{d}/\overline{\mathrm{d}}$ ratio of around 3 to 5, (Fig. 1.9, right) suggesting a clear dominance of matter over antimatter production at these energies.

The energy frontier at accelerators was reached about 40 years later, with the beginning of the Large Hadron Collider (LHC) operations, operating at energies between $\sqrt{s} = 900$ GeV and 13.6 TeV in pp collisions and centre-of-mass energies per nucleon pair from $\sqrt{s_{\mathrm{NN}}} = 2.76$ to 5.36 TeV in Pb–Pb collisions. Thanks to the large integrated luminosities provided by the LHC and state-of-the-art detector systems allowing for tracking down to low momenta (of the order of few hundreds of MeVs) and the identification of light (anti)nuclei, the ALICE experiment conducted an unprecedented campaign of measurements of light (anti)nuclei up to $A = 4$ in different collision systems and energies. The reach was extended to higher energies and higher momenta than any previous experiment, and unprecedented precisions were reached. The transverse-momentum dependent production of deuterons and antideuterons in inelastic pp collisions from 900 GeV to 7

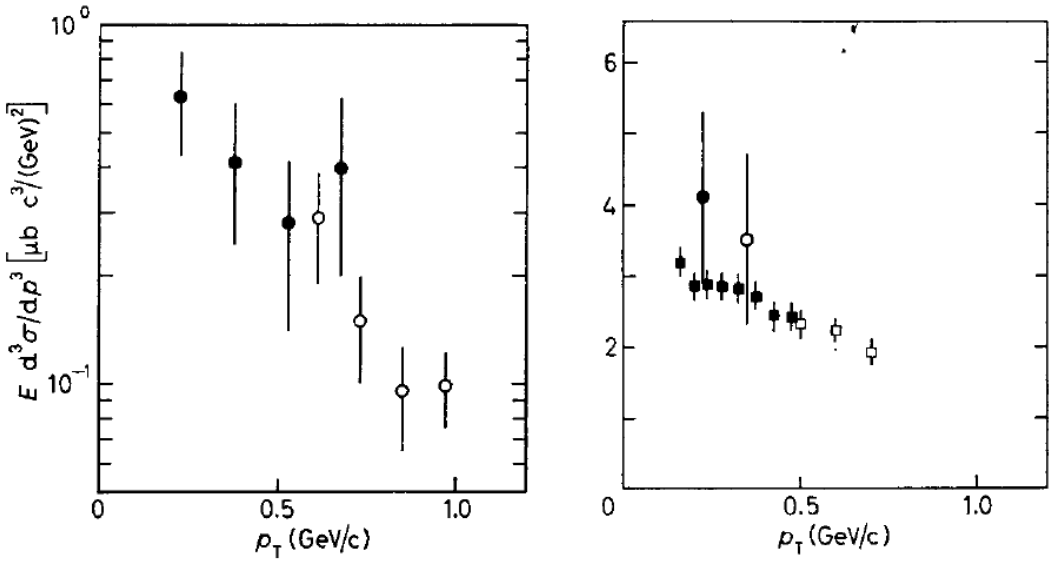

Figure 1.9: (Left) Invariant differential cross-sections for the production of antideuterons (statistical errors only) in pp collisions at $\sqrt{s} = 45$ GeV, full points are at $\sqrt{s} = 53$ GeV at ISR. (Right) Deuteron/antideuteron ratio (circles) compared with the proton/antiproton ratio (squares) squared at half of the transverse momentum at the two energies at ISR. From [18, 19].

TeV measured by ALICE at midrapidity ($|y| < 0.5$) are reported in Fig. 1.10 [20]. These measurements allowed ALICE to test the antimatter-to-matter balance [20] at LHC conditions. To this end, the ratio of antideuteron-to-deuteron is reported in Fig. 1.11 (left), and compared to the squared antiproton-to-proton ratio at different energies. The latter ratio is defined using the squared antiproton-to-proton ratio following the definition of the coalescence probability (Eq. 2.34, which will be clarified in Section 2.3). As expected, the $\overline{\mathrm{d}}/\mathrm{d}$ ratio approaches unity as the centre-of-mass energy increases as it is also observed for the antibaryon-to-baryon ratio [21].

The latest results on the antimatter-to-matter ratio in heavy-ion collisions [22] extended the measurements to (anti)tritons and (anti)helium in Pb–Pb collision at $\sqrt{s} = 5.02$ TeV. As expected from theory, ALICE confirmed that at the LHC conditions, the antinuclei-over-nuclei ratio is compatible with 1 and thus the baryochemical potential is compatible with zero.

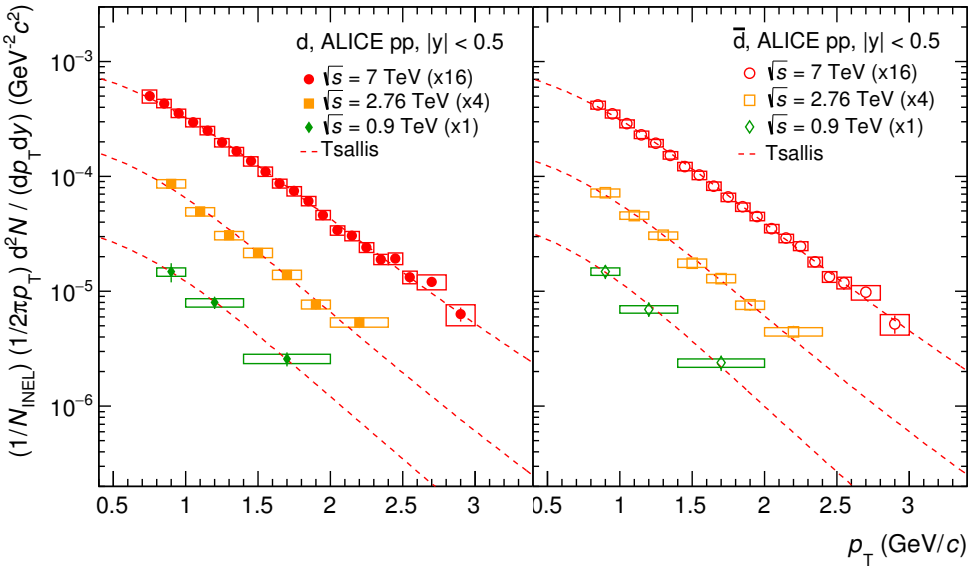

Figure 1.10: Invariant differential yield of deuterons (left panel) and antideuterons (right panel) in pp collisions at $\sqrt{s} = 0.9$, 2.76, and 7 TeV. Systematic uncertainties are represented by boxes and the data are multiplied by constant factors for clarity in the figure. The dashed line represents the results of a fit with a Tsallis function [20].

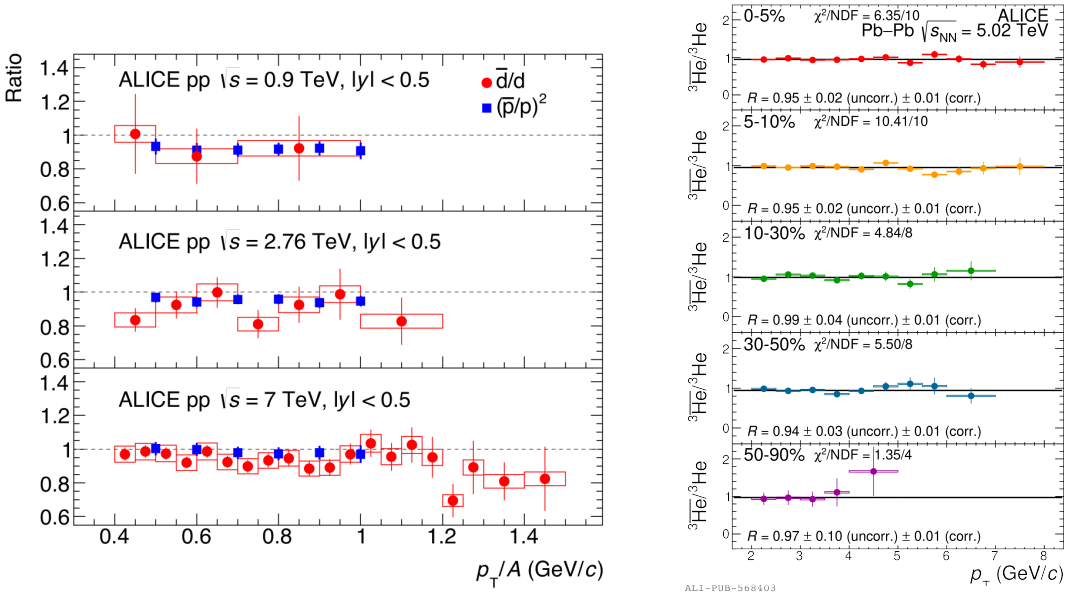

Figure 1.11: (Left) Antideuteron-to-deuteron ($\bar{\mathrm{d}}/\mathrm{d}$) ratio as a function of p_{T} per nucleon p_{T}/A compared to the squared antiproton-to-proton ratio $(\bar{\mathrm{p}}/\mathrm{p})^2$ (in blue squares) in pp collisions at different collision energies at midrapidity ($|y| < 0.5$) [20]. (Right) p_{T}-differential ratio of $^3\overline{\mathrm{He}}$ production relative to ^{3}He measured in Pb-Pb collisions at $\sqrt{s_{\mathrm{NN}}} = 5.02$ TeV in various centrality intervals (adapted from [22]). In both plots error bars are statistical uncertainties, while boxes represent centrality-uncorrelated systematic uncertainties.

In Fig. 1.12 the (anti)deuteron coalescence probability B_2 (more details in Section 2.3) measured in $\sqrt{s} = 7$ TeV pp collisions is shown in comparison with the measurements of B_2 performed by different collaborations and experiments [20]: Bevalac (LBNL), H1 & ZEUS (DESY), and ISR (CERN). Data from previous experiments cover a limited interval of p_{T}/A and are less precise than ALICE data. Nonetheless, these indicate that the probability of forming low momentum (anti)deuterons by coalescence in pp collisions at the TeV scale is compatible with the same probability in different collision systems at lower energies, including electron-proton (ep) collisions and photoproduction reactions. Thanks to the broader momentum coverage, the ALICE results reveal a p_{T} dependence in B_2 never seen in previous experiments.

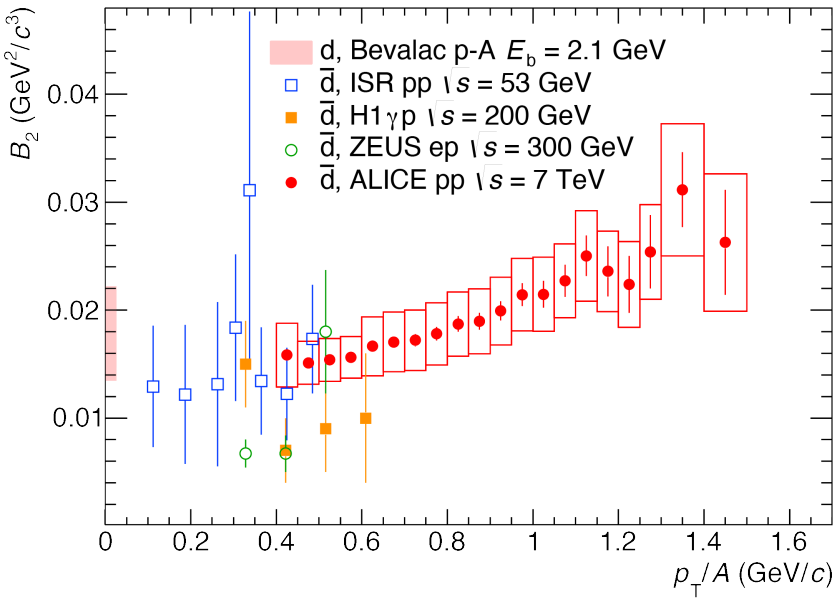

Figure 1.12: Coalescence parameter B_2 (see Section 2.3) in inelastic pp collisions at $\sqrt{s} = 7$ TeV (circles) compared with the values measured in pp, γp, ep (squares and hollow circles), in p–Cu and p–Pb collisions (band at $p_{\mathrm{T}}/\mathrm{A} = 0$ GeV/c). [20].

In addition, the ALICE experiment performed (anti)helium measurements in different colliding systems and at different energies, such as p–Pb collisions at $\sqrt{s} = 5.02$ TeV, Xe–Xe collisions at $\sqrt{s} = 5.44$ TeV and in pp collisions at $\sqrt{s} = 7$ and 13 TeV [20, 23, 24]. These campaigns allowed to measure the production yield as well as the coalescence parameter for three-nucleon systems (B_3), though with limited precision due to the rarer production than for deuteron (see Chapter 2). The spectra of (anti)helium-3 produced in pp = 13 TeV is shown in Fig. 1.13.

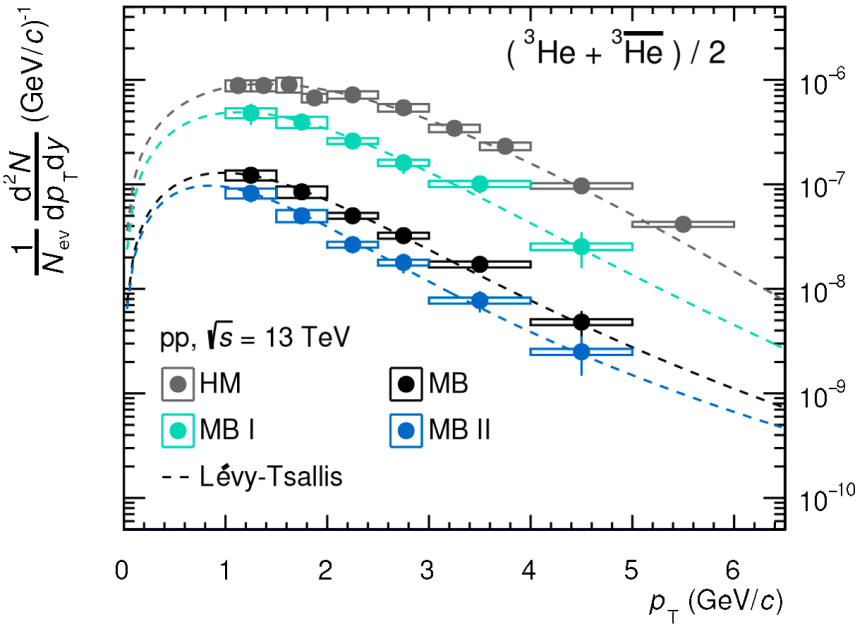

Figure 1.13: Transverse-momentum spectra of (anti)helium-3 measured in pp = 13 TeV at midrapidity (|y|< 0.5) [23]. The results are shown in different multiplicity classes.

1.3 Antinuclei in Cosmic Rays

Cosmic rays (CR) are particles that reach the Earth's atmosphere from the Sun or interstellar space [25]. They are mostly composed of high-energy protons and light nuclei. According to their production mechanism, CRs are classified as *primary* if they are produced and emitted directly by the astrophysical sources or as *secondary* if they are produced in the collision of primary CRs with the interstellar medium (ISM) or via decays. Primary CRs are mainly composed of electrons, protons (74% of the observed particles), neutrinos and nuclei, in particular helium (18%).

1.3.1 Antinuclei as a signature of Dark Matter

Dark matter (DM) is considered to be the dominant gravitationally attractive component in the Universe, but the details about its physical properties are still mostly unknown. The evidence about its existence and properties come from astrophysical - like the speed of rotation curves of spiral galaxies, velocity dispersion of elliptical galaxies and gravitational lensing - and cosmological - as anisotropies in the cosmic microwave background (CMB) - observations.

Most of the dark matter models characterise the nature of DM via quantum-field theory-based particle interactions. The baryonic DM hypothesis must be excluded [26] for different reasons. If DM had been composed of baryons, the cosmic microwave background (CMB) and cosmic web structure would be dramatically different from how they appear. Additionally, the abundance of light elements created during the primordial nucleosynthesis depends on the photon-to-baryon ratio density of the Universe; the observed deuteron and ^{4}He abundances provide constraints on the baryon density in the Universe, as those coming from CMB measurements. These measurements strongly reject the baryonic DM hypothesis. A deeper discussion is beyond the scope of the thesis, but the interested reader can find more in Refs. [27, 28, 29] on the topic. The candidates must satisfy a series of properties, most notably the electromagnetic neutrality, as the DM is expected to interact with ordinary matter with an order of magnitude smaller than typical weak-force interaction (the fine-structure α near the weak-scale coupling $\sim 10^{-2}$).

The most common non-baryonic candidates for DM are usually called *natural* candidates. *Axions* represent cold DM (particles characterised by an expected speed in space lower than the speed of light) as they are light ($m \approx 10^{-5} \div 10^{-3}$ eV). Axions have given origin as a strong-CP violation problem solution in particle physics. *Neutrinos* are ultra-relativistic and light ($m \approx 0.05$ eV) particles.

A third class of candidates for DM are weakly-interacting massive particles (*WIMPs*), introduced by Steigman and Turner [30]. These have a mass around the typical weak scale and are considered natural candidates in a significant number of theoretical models [31], such as the supersymmetric neutralino and a Kaluza-Klein photon [32]. The observed abundance of DM in the Universe can be explained through the WIMP thermal freeze-out mechanism. In the primordial Universe, ordinary matter and DM were in thermal equilibrium. Due to the Universe expansion, WIMPs froze out of equilibrium with the thermal plasma. The decoupling was due to the reduced WIMP annihilation rate, and it happened at the moment in which the rate reached the expansion rate of the Universe. In this sense, WIMPs would be considered as thermal relics of the Universe. It is important

to stress here that WIMP candidates, like the χ neutralino, have not been experimentally observed yet, and there are no theoretical reasons to prefer the WIMP model for DM to other natural candidates.

WIMP particles are predicted to annihilate or decay into ordinary matter, producing a large spectrum of different species, among which antiprotons and antineutrons. These antinucleons can interact and form bound states, the light antinuclei. These light antinuclei (as $\overline{\mathrm{d}}$ and $^3\overline{\mathrm{He}}$) from WIMPs are considered promising DM detection signals [33, 34] and they are expected to be produced with a kinetic energy per nucleon around 0.1 - 1 GeV. As detailed in the next section (Section 1.3.2), the predicted flux for $\overline{\mathrm{d}}$ and $^3\overline{\mathrm{He}}$ is much higher than the expected background from astrophysical secondary sources, as shown in Fig. 1.14: according to different models, the $^3\overline{\mathrm{He}}$ from DM signal in the low kinetic energy per nucleon is almost background-free, as the fluxes differ of almost three orders of magnitude. The $^3\overline{\mathrm{He}}$ is an interesting candidate also for its larger mass with respect to $\overline{\mathrm{d}}$, which implies a higher formation energy threshold.

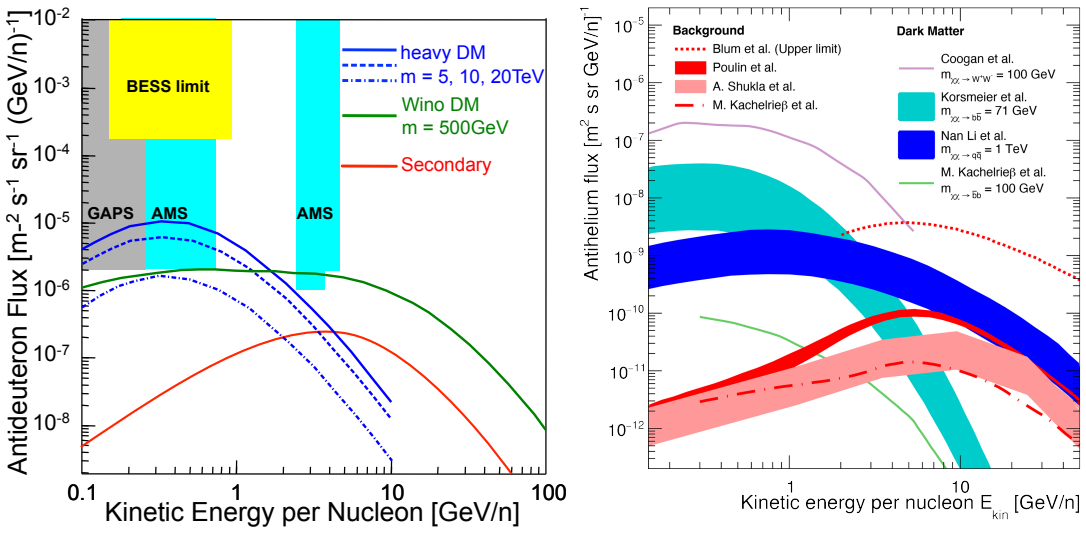

Figure 1.14: (Left) Predicted antideuteron flux from annihilation of DM with $m_{DM} = 5, 10, 20$ TeV [35] (blue lines, top to bottom) and from pure-Wino DM [36] (green line). The astrophysical background from secondary cosmic rays (red line) is shown. (Right) The expected flux for $^3\overline{\mathrm{He}}$ as a function of the kinetic energy per nucleon [37] according to different models from literature. Fluxes from DM annihilation are in blue and green colors, whereas fluxes from the astrophysical background are shown with red curves and bands. The error bands are due to both uncertainties in the coalescence momentum and propagation uncertainties.

1.3.2 Antinuclei from secondary Cosmic Rays

The antinuclei produced in secondary CR interactions are the main background in searches for antinuclei from dark matter particle interactions. As no primary sources are expected for antinuclei in the Galaxy, the observed antinuclei are produced by primary CR collisions

with the interstellar matter (ISM). The antinucleus abundance depends on the flux of cosmic rays, the distribution of ISM and the production cross section. To correctly predict the expected flux of antinuclei near Earth, where space-borne and air-borne cosmic ray experiments might operate, the CR sources and the propagation of the produced electrically-charged antinuclei through our Galaxy must be modelled in detail and, additionally, the corrections due to the interaction with the heliosphere also have to be accounted for.

The propagation of CRs in the Galaxy is driven by magnetic fields. The CR propagation for a particular particle species can be written in the general form [38] as

$$\frac{\partial\psi(\vec{r},p,t)}{\partial t} = q(\vec{r},p,t) + \vec{\nabla}\cdot\left(D_{xx}\vec{\nabla}\psi - \vec{V}\psi\right) + \frac{\partial}{\partial p}p^2 D_{pp}\frac{\partial}{\partial p}\frac{1}{p^2}\psi - \frac{\partial}{\partial p}\left[\dot{p}\psi - \frac{p}{3}(\vec{\nabla}\cdot\vec{V})\psi\right] - \frac{1}{\tau_f}\psi - \frac{1}{\tau_r}\psi\,, \quad (1.10)$$

where $\psi(\vec{r},p,t)$ is the CR density at position $\vec{r}$ per unit of momentum p, $q(\vec{r},p,t)$ is the source term, $\vec{V}$ is the convection velocity, D_{xx} is the spatial diffusion coefficient, D_{pp} is the coefficient that describe the diffusive reacceleration, $\dot{p}$ is the momentum derivate with respect to time, τ_r is the radioactive decay timescale and τ_f is the loss by fragmentation timescale.

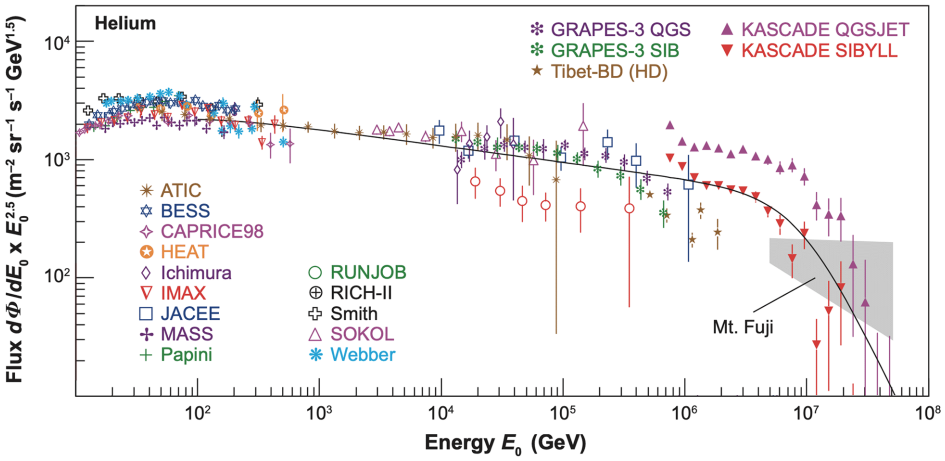

Figure 1.15: Compilation of spectral data $10^{10} - 10^{17}$ eV for helium combining balloon, satellite, and ground-based measurements. Adapted from [38].

The CR fluxes modelled with the previous equation must be corrected for the time-dependent shielding effect due to solar modulation [39]. To describe this effect, the most commonly used model is the force-field approximation, but this model does not describe accurately the CR flux at low energy [40, 41]. State-of-the-art approaches to this problem are based on numerical solutions of the heliospheric diffusion equation, such as the `HELMOD` model [42]. The heliospheric diffusion equation that describes the propagation of CRs in the heliosphere [33] is commonly written as

$$\frac{\partial f}{\partial t} = -(\vec{V}_{sw} + \vec{v}_d)\cdot\nabla f + \nabla\cdot(\mathbf{K}\cdot\nabla f) + \frac{P}{3}(\nabla\cdot\vec{V}_{sw})\frac{\partial f}{\partial P}\,, \quad (1.11)$$

where f is the CR phase space density, $\mathbf{K}$ is the symmetrised diffusion tensor, P is the CR momentum, $\vec{V}_{sw}$ is the speed of the solar wind and $\vec{v}_d$ is the (divergence-free) speed associated to drifts.

Numerical approaches are also used to solve the diffusion equation Eq. 1.10 for CR in the Galaxy to obtain the steady-state solution within the galactic volume. One of the state-of-the-art codes used for this estimation is `GALPROP` [43]. This framework uses a method based on discrete timesteps to evolve the momentum-dependent particle density in the ISM until the steady-state is reached [43, 44]. The method used by `GALPROP` is the Crank-Nicolson method, which is much more time-efficient than the conventional explicit method (which calculates the evolution of the particle-density distribution in the timescales of the diffusive motion through the Galaxy, typically 10^7 years, in steps of the order of the timescales of the energy losses by ionisation or radiative emission of nuclei, 10^3 years).

1.3.3 Searches for antimatter in Cosmic Rays

Low-energy CRs can be measured using high-atmosphere and space-based detectors. This kind of experiment has the advantage of having very low contamination due to limited CRs-atmosphere interactions. This can be achieved by different experiments that use different techniques (as shown in Fig. 1.15, in which the spectral data for helium is measured combining balloon, satellite and ground-based measurements). Three of the most recent experiments of this type will be presented here.

BESS and BESS-Polar The Balloon-borne Experiment with Superconducting Spectrometer (BESS) was a vast program of different measurements performed via high-resolution magnetic-rigidity spectrometer for low-energy protons and antinuclei at extreme latitudes. The BESS spectrometer was placed in a balloon designed for long-time flights. The BESS experiment performed 9 flights over northern Canada from 1993 to 2002, while the more recent BESS-Polar and BESS-Polar II (shown in Fig. 1.16) with upgraded equipment collected data in Antarctica above the South Pole from 2004 to 2007. The cutoff rigidity reached by the last version of the BESS spectrometer was below 0.5 GeV. Among the most important results from BESS is the upper limit on the $\bar{\mathrm{d}}$ flux [45], which was recently updated to the value of 6.7×10^{-5} $(\mathrm{m}^2\ \mathrm{s\ sr\ GeV/n})^{-1}$ at 95% confidence level [46] in a kinetic energy range per nucleon from 0.163 to 1.100 GeV/n. Additionally, the experiments set an upper limit for the antihelium-over-helium ratio to be 6.9×10^{-8} at 95% confidence level combining all BESS data [47].

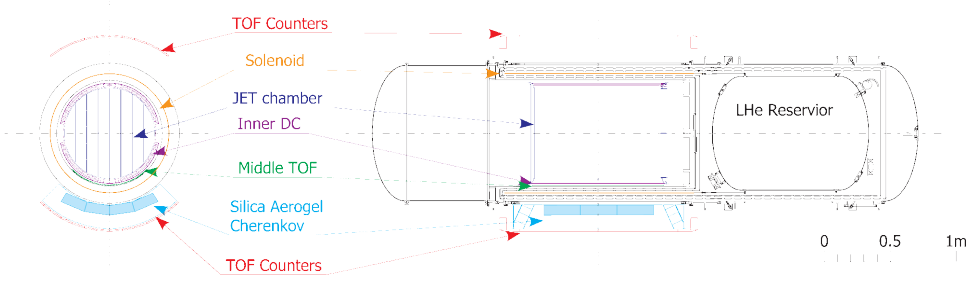

Figure 1.16: Cross-sectional and side views of the BESS-Polar II Spectrometer [47].

PAMELA The Payload for Antimatter Matter Exploration and Light-nuclei Astrophysics (PAMELA) was a satellite-installed experiment that studied the CR fluxes from 2006 to 2016 [48]. The PAMELA instrument was located on the Resurs-DK1 satellite. It was composed of a Time-Of-Flight (TOF) detector, a silicon magnetic spectrometer (with an average value $B = 0.43$ T), an electromagnetic imaging calorimeter, a shower tail catcher scintillator and a neutron detector. The apparatus was able to measure the speed of particles with the TOF detector, the charge Z via scintillators, and the rigidity of charged particles in the magnetic field as the inverse of the particle deflection in the field. The main goal of the PAMELA experiment was the study of cosmic antiprotons, positrons and light antinuclei. The apparatus was able to study antiprotons with an energy sensitivity ranging from 80 MeV up to 190 GeV, while for the positrons, the energy range was from 50 MeV up to 270 GeV. The prositron-over-electron is shown in Fig. 1.18 (a).

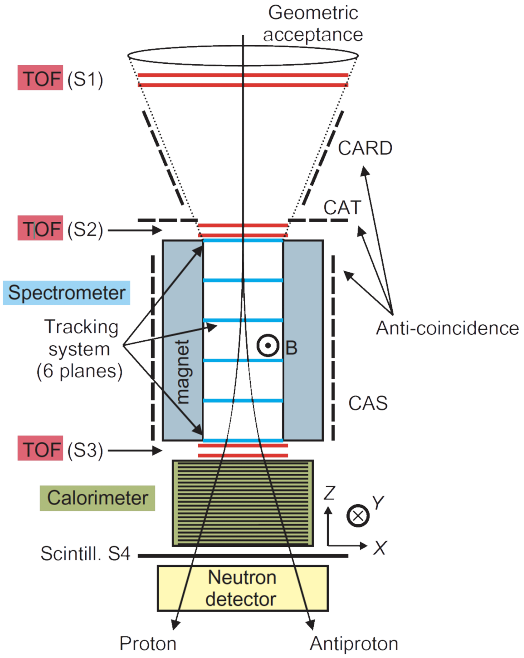

Figure 1.17: Schematic overview of the PAMELA apparatus. The detector was 1.3m high and had a mass of 470 kg. The average power consumption was 355 W. The average value of the magnetic field was 0.43T [48].

The latter feature allowed PAMELA to observe that the measured positron-over-electron ratio increases for energies higher than 10 GeV [49], an unexpected result that has been later confirmed by other experiments, such as FERMI [50] and AMS-02 [51]. This breaking result contradicted the expected secondary production in the models of CR propagation in the Galaxy, in which propagation was modelled as a diffusive process. The PAMELA experiment also estimated the ratio of measured antiprotons over protons. In Fig. 1.18 (b) this ratio is shown as a function of the kinetic energy and compared with different models which assume the production as exclusively secondary: the ratio shows a rising behaviour up to 10 GeV ($\overline{p}/p \sim 0.2 \times 10^{-3}$) and then it lowers (down to $\overline{p}/p \sim 0.1 \times 10^{-3}$).

This measurement allows the setting of boundaries to the diffusion coefficient or to study the effect of a local CR source [52], and with this vast energy range, it allows to set boundaries for the contributions of DM decay and annihilation. The PAMELA design allowed the apparatus to be extremely sensitive to the antihelium-to-helium ratio (up to 10^{-7}), but the experiment did not observe any antihelium signal.

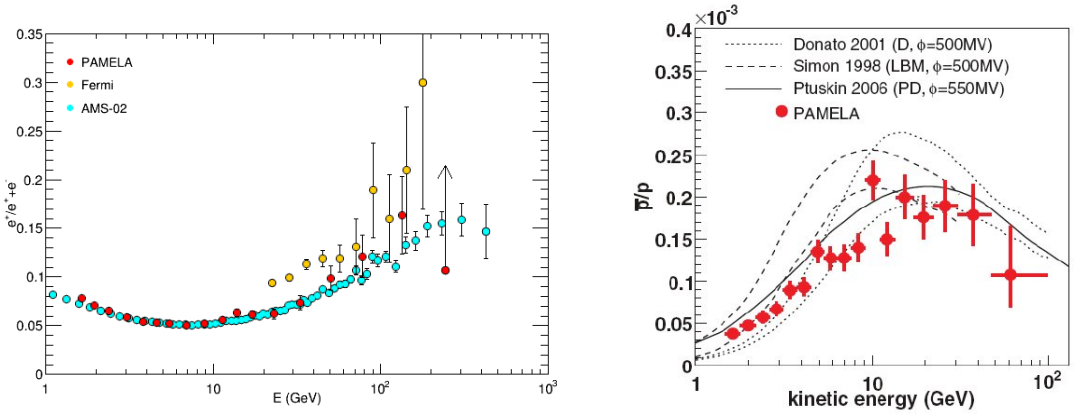

(a) (b)

Figure 1.18: (a) Galactic cosmic ray positron fraction measured by PAMELA, along with FERMI and AMS-02 measurements. Only statistical errors are shown [49]. (b) Galactic cosmic ray antiproton over proton fraction as a function of the kinetic energy, along with secondary production model predictions [48]. The dashed lines show the limits calculated for the Leaky Box model [53], while the dotted lines show the limits for a diffusion model with reacceleration [54]. The solid line shows the calculation for the case of a plain diffusion model [55].

AMS-02 The Alpha Magnetic Spectrometer (AMS-02) experiment is a cosmic ray detector located at the International Space Station (ISS), the purpose of which is to study the chemical and isotopic composition of CRs. Since the start of its operations in May 2011, it collected more than 240 billion events [56]: of these, more than 10 billions are protons and more than 100 millions are deuterons [57].

AMS-02 is a magnetic spectrometer, as PAMELA, and it is composed of different subdetectors, as shown in Fig. 1.19. The photons and electrons can be detected, and their energy and direction can be measured by an electromagnetic calorimeter (ECAL). The Transition Radiation Detector (TRD) is used to separate the signal due to light mass particles (electrons, pions, kaons). The Time-Of-Flight detector (TOF) is used as the main trigger and measures the particle speed up to $\beta = 0.8$. The particle path bends due to the magnetic field of the solenoid, and this allows us to measure the rigidity $p/|Z|$. The particle charge is measured with a Ring Cherenkov counter (RICH). From the particle charge, the momentum can be extracted knowing the rigidity. The mass of the particles can be estimated with the equation $m = ZR/\gamma\beta$. Thanks to the different charges and masses, it is possible to separate (anti)protons, (anti)deuterons, (anti)helium-3 and (anti)helium-4.

One of the first results obtained by AMS-02 has been the observation (and, accordingly, the confirmation) of the positronic anomaly measured by PAMELA [58]. In the years of operations, AMS-02 collected seven antideuteron candidates and eight antihelium candidates: six antihelium-3 and two antihelium-4 nuclei. Fig. 1.20 reports an example of event display with the signal from a potential ^{4}He candidate. To date, no confirmation has been given about these candidates' nature [59].

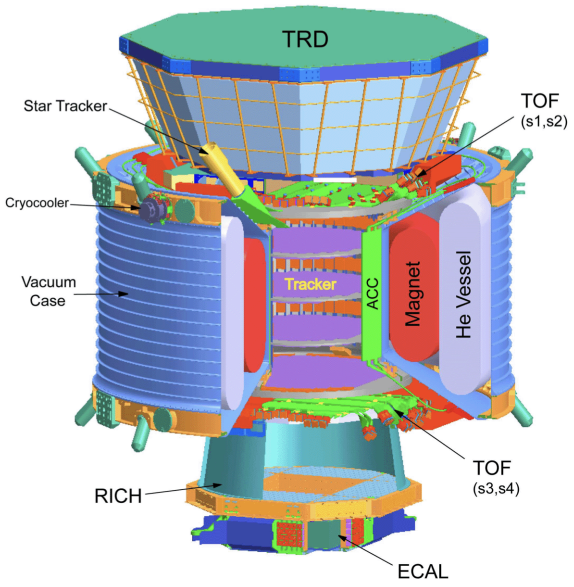

Figure 1.19: Layout of the AMS-02 experiment [57].

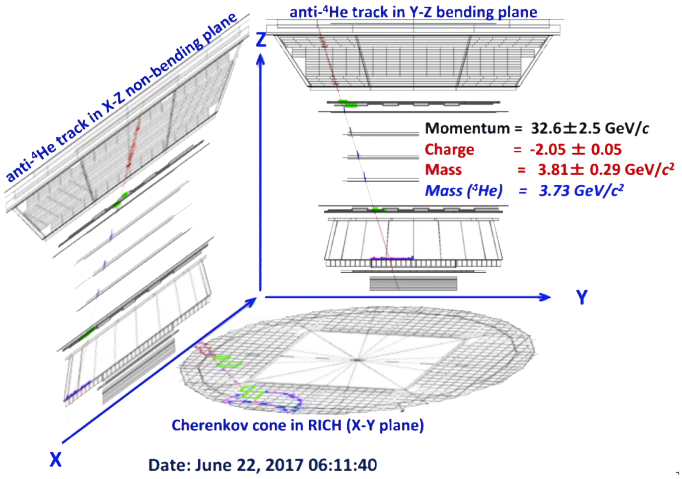

Figure 1.20: One of the two antihelium-4 candidates events observed by the AMS-02 collaboration [59].

GAPS The General AntiParticle Spectrometer (GAPS) is a balloon-based experiment [60, 61] whose start of the operation and first flight are planned for the end of 2024. Its main purpose is the measurement of the light (anti)nuclei flux above Antarctica. The data-taking campaign will be performed on several 35-day-long flights. The detector is designed to use ten plates of 1-2 mm thick Si(Li) detectors, according to a scheme reported in Fig. 1.21. The Si(Li) allows for the detection of (anti)nuclei with an innovative technique: when the (anti)nuclei travel through the Si(Li) plates, they can be absorbed and create an excited exotic atom. The excitation state will endure for a time of the order of the nanosecond, and then the exotic atoms will decay to the ground state, emitting an X-ray. As the X-ray energy is well known, measuring the X-ray energy, the particle energy loss in the material, the time-of-flight of the particles and the multiplicity of other particles will allow us to identify (anti)nuclei. For this purpose, GAPS will also have a large TOF detector that will be used to provide a high-speed trigger to serve as a shield/veto to the instrument and measure the particle velocity up to 0.5 β and also the energy deposit.

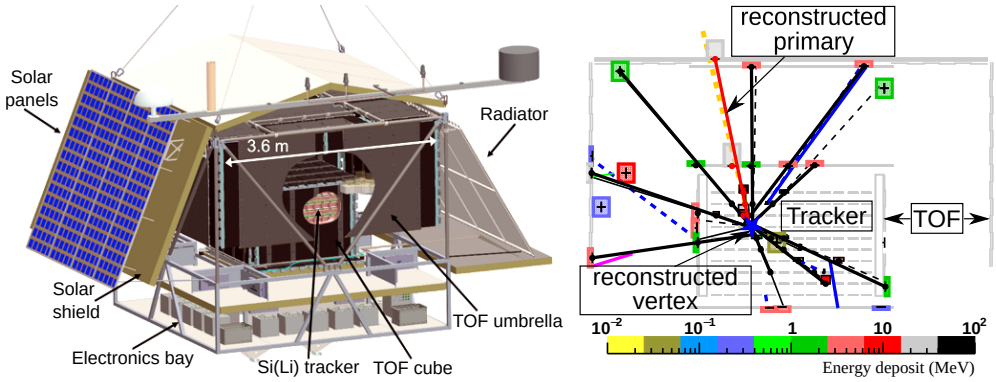

Figure 1.21: (Left) Schematic overview of the GAPS instrument [62]. (Right) The GAPS detection system. An antinucleus ($^3\overline{\text{He}}$) travels between two layers of the TOF detector and slows down until it stops in the Si(Li) target, forming an (excited) exotic atom. The orange dashed and red solid line indicate the simulated and the reconstructed primary $^3\overline{\text{He}}$ nuclei, respectively. After atomic de-excitation, X-rays are emitted, followed by pions and protons by nuclear annihilation (other coloured solid lines).

The launch of GAPS will enable precise antiproton measurements in a new unexplored low-energy range, below 0.25 GeV per nucleon, as reported in Fig. 1.22. GAPS expect to collect up to 500 antiprotons per single long-duration flight [63], allowing the collection of enough data to perform both DM model validation and other astrophysical studies about the primordial black hole evaporation [64].

In addition, based on full instrument simulation, event reconstruction, and realistic atmospheric influence simulations, a projected GAPS flux sensitivity to antihelium-3 nuclei, assuming the detection of one event in one 35-day flight is estimated to be $4.0^{+13.3}_{-3.8} \times 10^{-6}$ $(\text{m}^2\ \text{s sr GeV/n})^{-1}$ at the 95% confidence level [63].

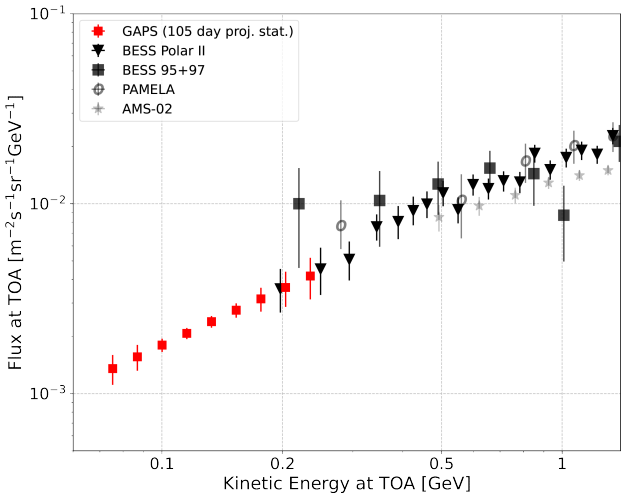

Figure 1.22: The projected GAPS precision cosmic antiproton spectrum (red) at the top of the atmosphere is shown with the statistics expected from three 35-day flights [63]. Additionally, data from original BESS, BESS Polar II, PAMELA and AMS-02 are plotted.

Chapter 2

(Anti)nuclei formation models

In Chapter 1, the discovery of antimatter was briefly discussed, from the discovery of the positron up to the production of light antinuclei at modern hadron and heavy-ion colliders. These significant observations open up a significant puzzle: how can light (anti)nuclei, which are loosely-bound states, be produced and survive at the high temperatures achieved in the final state of ultra-relativistic heavy-ion collisions? Do the cluster formation mechanisms, ultimately driven by the strong interaction, differ in various collision systems, and how? After a brief but essential introduction to the physics of heavy-ion collisions in Section 2.1, two of the main approaches used to describe nuclear production at colliders, the statistical hadronisation models (SHMs) [65, 66] and the coalescence model [67, 68], are introduced in Section 2.2 and in Section 2.3, respectively. Model predictions are discussed in comparison with recent results from the LHC, at the energies most relevant for this thesis work.

2.1 High-energy heavy-ion collisions: from QCD to hadrochemistry

The Standard Model of particle physics (SM) is the quantum field theory that describes three of the four known fundamental interactions in the Universe. Within the framework of the SM, Quantum Chromodynamics (QCD) is the state-of-the-art gauge theory that explains the strong interaction [69]. The name chromodynamics derives from the ancient Greek word χρῶμα, *colour*, which is the name of the QCD charge.

The Lagrangian of the QCD possesses an explicit SU(3) local gauge invariance, which results in eight massless mediator bosons called *gluons*.

It is written in the form

$$\mathcal{L}_{\mathrm{QCD}} = \mathcal{L}_{\mathrm{gluons}} + \mathcal{L}_{\mathrm{quarks}} = -\frac{1}{4} G^a_{\mu\nu} G^{\mu\nu}_a + \sum_f \overline{\Psi}_f \left(i\gamma^\mu \partial_\mu + g_s \frac{\lambda_a}{2} \gamma^\mu A^a_\mu - m_f \right) \Psi_f \quad (2.1)$$

where a is the *group index*, A^a_μ is the *gluon field* that is due to the SU(3) generator λ_a, f is the *quark flavour index* and g_s is the *coupling constant* of the strong interaction. The SU(3) symmetry of the Lagrangian is non-abelian. As a consequence, the gluon tensor has an additional contribution with respect to the photon tensor of the Quantum Electrodynamics

(QED) Lagrangian:

$$G_a^{\mu\nu} = \partial^\mu A_a^\nu - \partial^\nu A_a^\mu - g_s f_{abc} A_b^\mu A_c^\nu \tag{2.2}$$

where f_{abc} is the structure constant of SU(3). The existence of this not-null structure constant implies the existence of two self-interaction vertices for gluons that allow for loop corrections to the gluon propagator: the effect of these corrections is the so-called *anti-screening* of the colour interaction. The intensity of the strong interaction depends on the distance and the transferred momentum Q, as the coupling constant of the strong interaction $\alpha_s = g_s^2/4\pi$ is

$$\alpha_s(Q^2) = \frac{\alpha_s(\mu^2)}{1 + \frac{33-2n_f}{12\pi} \ln \frac{Q^2}{\mu^2}} \tag{2.3}$$

where n_f is the number of flavours and μ is the *renormalisation scale* of the QCD [3]. For low values of Q^2, the quarks are bonded inside their hadron phase (*confinement regime*), while for higher values of transferred momentum, the coupling becomes asymptotically null and the theory describes free states (*asymptotic freedom*). The measured values of α_s in different experiments and using different approximations are summarised in Fig. 2.1.

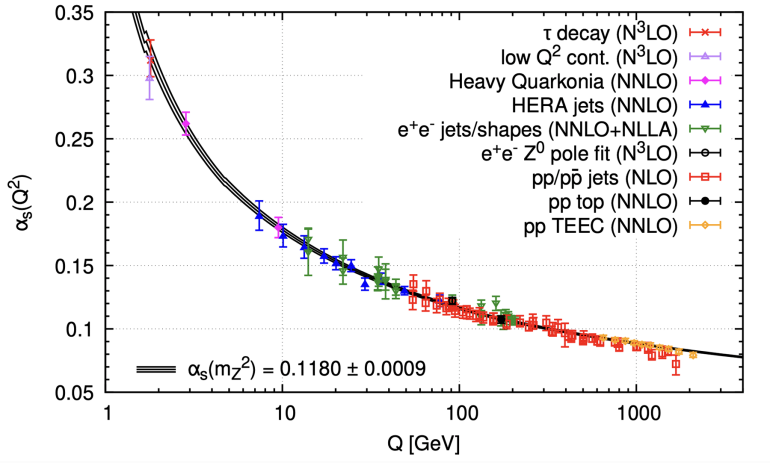

Figure 2.1: The measurements of the α_s coupling as a function of the transferred quadri-momentum Q [25].

2.1.1 QCD phase transition

A consequence of the α_s behaviour shown in Eq. 2.3 is the existence of different states of strongly interacting nuclear matter [69]. As shown in the phase diagram of QCD (see Fig. 2.2) as a function of the temperature (T) and the baryochemical potential (μ_B), different phases of matter can be characterised by the temperatures and the densities. The baryochemical potential is quantity introduced to account for the fact that in a relativistic quantum system the particle number is not always conserved, because of particle annihilation and creation processes.

The baryochemical potential $\mu_B = \frac{\partial E}{\partial N_B}$, therefore, is defined as the energy that has to be provided to the system to increase the total number of (anti)baryons of one unity.

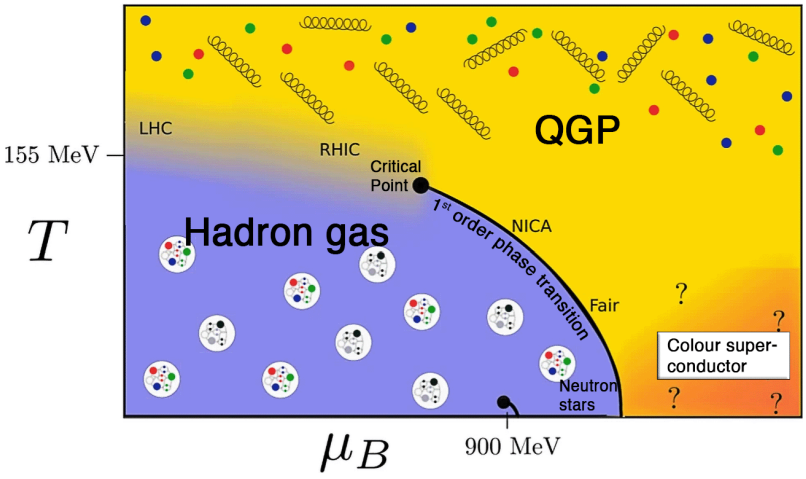

Figure 2.2: Phase diagram of QCD. Adapted from [70].

At low temperatures and low baryochemical potentials in Fig. 2.2 nuclear matter is in its ordinary state, with quarks and gluons confined into hadron (referred to as hadron gas). By increasing the values of T while keeping $\mu_B \approx 0$ GeV, the transition to a deconfined partonic matter is a smooth crossover. With the increase in temperature, the mean transferred momentum increases as well, and, as a consequence, the strong interaction becomes weaker. These conditions, similar to those of the primordial Universe, lead to a state of deconfined strongly-interacting matter, in which quarks and gluons can freely move in a strongly interacting plasma called Quark-Gluon Plasma (QGP). According to Cosmology [71], the QGP-to-hadron phase transition took place in the early Universe, when the baryochemical potential reached the value $\mu_B \approx 0.33$ eV, as a consequence of the cooling process due to the matter expansion. Moving instead along the μ_B axis while keeping low temperature $T \approx 0$ GeV, one encounters baryon-rich systems characterised by a high baryon density, such as neutron stars, and then a first order phase transition leads to a deconfined state, hypothesised to be present in the core of neutron stars.

At the LHC $\mu_B \approx 0$ the transition is expected at the temperature $T \approx 150$ MeV [72]. A simple estimation of the QCD critical energy density for the phase transition to occur can be given using the Stefan-Boltzmann law and considering the system quarks and gluons as a gas of massless particles moving inside a volume V [73]. The energy density ϵ can be expressed as

$$\epsilon = \frac{\pi^2}{30} n_{DOF} T^4 \tag{2.4}$$

where n_{DOF} is the number of degrees of freedom of the system. For the QGP, $n_{DOF} = (16 + \frac{21}{2} n_f)$, which allows to estimate the energy density $\epsilon \sim 1$ GeV/fm^3 using the pseudocritical temperature $T_C = 150$ MeV.

2.1.2 Heavy-ion collisions

The extreme conditions that allow for the formation of QGP can be achieved by colliding ultrarelativistic heavy ions at colliders and thus enable the study of the phase boundaries

between ordinary hadronic matter and the QGP. When accelerated to ultra-relativistic energies, heavy nuclei appear as Lorentz-contracted disks along the direction of the beam axis. As a consequence of the Lorentz contraction, the nuclei transverse dimension appears wider than their longitudinal dimension. The collision, therefore, can be considered as the superposition of binary nucleon-nucleon collisions: a fraction of the nucleons called *partecipants*, participates in the collision (their number is N_{part}), while the non-participant nucleons are called *spectators* (and their number is $N_{spect} = 2A - N_{part}$, where A is *atomic mass number*).

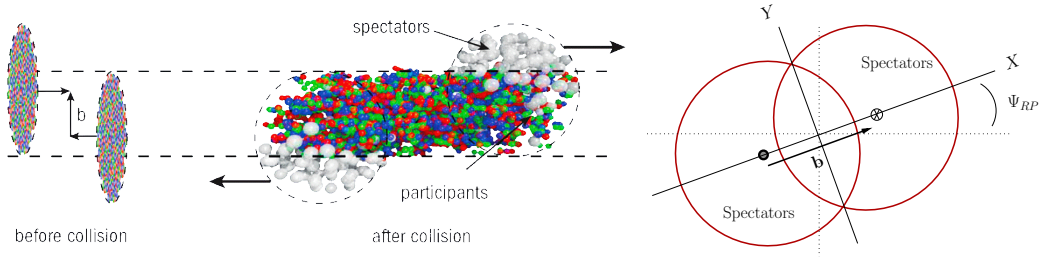

Figure 2.3: An ultra-relativistic heavy-ion collision is seen from the yz plane. b is the impact parameter. The impact parameter is used also for the determination of the plane of the collision (*event plane*), defined by the angle Ψ_R between the beam direction (z axis) and the impact parameter vector $\vec{b}$.

The geometry of a collision is characterised by the impact parameter b, which is defined as the module of the vector between the centres of the two nuclei in the transverse plane with respect to the collision axis, as shown in Fig. 2.3. The parameter quantifies the overlap region between the two colliding nuclei.

A collision is called *central* if it is characterised by a small impact parameter and a large number of participants are involved. Notably, an ideal central collision would be a head-on collision with all the nucleons participating and a null impact parameter. On the contrary, a collision is called *peripheral* if it has a large impact parameter and is characterised by few participant nucleons. As centrality strongly affects the charged multiplicity of a heavy ion collision, it is one of the main parameters used for classifying HI events. Classes of centrality are commonly defined in terms of a percentile of the nucleus-nucleus hadronic cross section. The measurement of the centrality of a collision is an indirect measurement of the number of participant nucleons. This is fundamental, as it allows the normalisation of the observables between different colliding systems (e.g. pp or p–Pb). The centrality of a collision is measured usually in two different ways. The first method is based on the relation between centrality and the number of the (charged) particles produced in the collision (the multiplicity), the latter of which can be measured by an experiment. This method is dependent on the choice of a geometrical model for the hadronic processes. The main method used for estimating this correlation is the Glauber model [74], which is based on the assumption that nucleons keep travelling in linear trajectories and that the binary nucleon-nucleon cross section is independent of the number of the antecedent collisions. A second method is based on the measurement of the energy carried by the spectators along the forward zero-degree directions, usually performed via calorimeters located near the beam pipe. The number of spectators is complementary to the number of participants.

This method has the advantage of being independent from any collision model.

2.1.3 Evolution of a heavy-ion collision

After an ultra-relativistic collision between heavy nuclei, a long-lived strongly-interacting system is created as a consequence of the deposit of a large amount of energy in a small volume. The investigation of the evolution of this state of matter and the characterisation of its properties is of fundamental importance and one of the main goals of heavy-ion experiments [75]. The evolution of this system is represented in a space-time diagram in Fig. 2.4, where t indicates the time after the collision and z represent the beam axis.

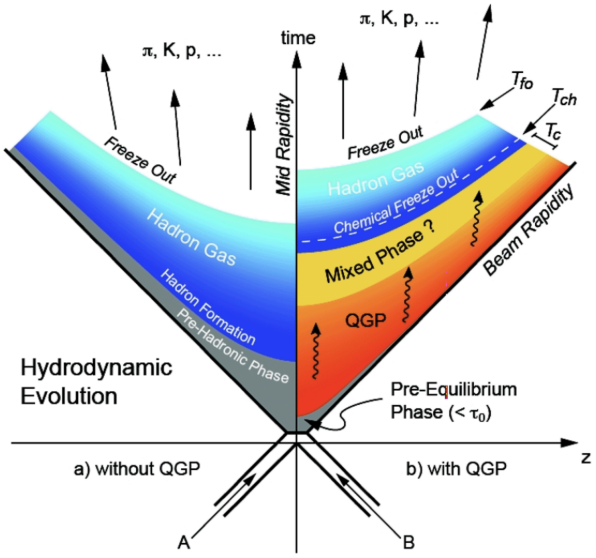

Figure 2.4: Evolution of a heavy-ion collision represented in a space-time diagram [76]. The z direction is parallel to the beam line. The two panels represent the evolution with (right) and without (left) QGP formation.

The phases of the collision [75, 77] are here summarised:

1. for $t < 0$ fm/c: two nuclei move along the beam line, and due to the ultra-relativistic energies, they are strongly Lorentz contracted in the laboratory reference frame. This is called the *pre-collision stage*.

2. at $t = 0$ fm/c: the collision happens as described in Section 2.1.2.

3. for $0 < t < 1$ fm/c: the initial binary collisions between nucleons involve hard scattering between partons with large momentum transfer. These processes are characterised by a high transferred momentum between colliding partons. In this *pre–equilibrium phase*, all the high-energy particles are produced. In these first instants of the collision, the nuclei deposit a large amount of energy in the midrapidity region, and then they proceed to the forward rapidities. As a result, the system at this stage at midrapidity is a hot interacting medium with null baryochemical potential ($\mu_B \approx 0$). In contrast, the baryochemical potential is carried at forward rapidity by the escaping valence

quarks and the spectator nucleons. At LHC conditions, there will be a QGP phase transition. The QGP (*droplet*) created in the process reaches a thermal equilibrium after strong parton scattering interactions at its proper time τ_0.

4. for $1 < t < 10$ fm/c: the produced QGP hot *fireball* expands due to pressure gradients at the system boundaries. This expansion phase is modelled using relativistic hydrodynamics. The expansion causes the hot matter to cool down progressively.

5. for $10 < t < 15$ fm/c: the matter finally reaches the critical temperature T_C and, at this point, the *hadronisation* process starts. This brings the deconfined matter through another *phase transition* back to confined strongly-interacting matter. The system gradually moves into an interacting *hadron resonance gas* (HRG). The elastic and inelastic interactions between hadrons continue to occur during all the fireball expansion. After the momentum exchange between hadrons is not sufficient to allow inelastic interactions, the relative abundances of different particle species are fixed. This happens when the fireball reaches the so-called *chemical freeze-out*. When the hadrons stop interacting, and the particle momenta are fixed, the HRG reaches the *kinetic freeze-out*.

6. for $t > 15$ fm/c: the hadrons created are finally free to exit the interaction region and the *free hadron stream* can finally reach the detector. Eventually, particle decays due to strong or weak interactions will occur.

As shown in the Fig. 2.4, the QGP droplet formation does not happen in every collision. If the energy density is not sufficiently high to create the QGP, hadronisation occurs directly after the collision. In pp and p–Pb collisions, the final state can be significantly different because of the lower production of partons in the very initial stages and the lower energy density deposit, which may be insufficient for the system to transition to a QGP.

2.2 Statistical Hadronisation Models

The statistical hadronisation models (SHM) (or *thermal models*) are models used to predict the abundances of different particle species produced in particle collisions. The story of these models began with the very first particle collisions model: one of the first models was proposed by E. Fermi [78] in the 1950s and improved and developed by R. Hagedorn [79] in the 1960s. In the 1990s the first successful application of statistical hadronisation was achieved to comprehensively describe data from the BNL AGS and Si + Au(Pb) collisions. In the same period, G. Brown [80] successfully described the influence of resonance decays on pion spectra using a thermal approach.

The main SHM assumption is that, in a collision, all the particles that are compatible with the conservation laws (due to the Standard Model) can be produced. The relative abundance of every species will strongly depend on to the particle partition function. The medium produced after a collision can be described as an expanding hot, non-interacting gas of known hadrons and resonances. According to slightly different boundary conditions depending on the size of the collision system, the model can precisely predict the hadron yields measured in different colliding systems and at different energies. For systems that are characterised by a large interaction volume produced after the collision (e.g. heavy-ion

collisions), a grand canonical ensemble (GC) statistical model is used, while for smaller systems (like pp and p–Pb collisions), it is necessary to use a canonical model.

2.2.1 Grand Canonical Statistical Hadronisation Model

The heavy-ion collisions at the LHC produce a large reaction volume, and the hadron-resonance gas resulting from them can be described using a Grand Canonical ensemble. This formalism can be used as the detectors can access a portion of the entire interaction system, for example, the mid-rapidity region. This volume is in contact with an energy and particle reservoir and in equilibrium with it. This equilibrium condition implies that the energy and quantum numbers (electric charge, baryon number, isospin, ...) are conserved on average. The average conservation of the charges is distinctive of the Grand Canonical (GC) hadronisation formalism [65] used to characterise heavy-ion collisions. The extension of this model to the study of smaller colliding systems, the canonical hadronisation model discussed in Section 2.2.2, requires the exact local conservation of the charges.

The Grand Canonical formalism is therefore used to characterise the statistical properties of a physical system at the thermodynamical equilibrium in a heavy-ion collision, using parameters like the baryochemical potential μ_B or the temperature T. In fact, the SHM describes an hadronic system after the hadronisation that follows the QCD phase transition discussed in the previous section. Hence, the GC partition function $Z(T, V, \mu)$ can be written as:

$$Z(T,V,\mu) = \mathrm{Tr}\left\{\exp\left[-\beta\left(H + \sum_i \mu_i Q_i\right)\right]\right\}, \text{ with } \mu = \sum_i \mu_i Q_i \quad \text{and } \beta = \frac{1}{T} \tag{2.5}$$

where T is the temperature of the medium, V is the volume, Q_i are the conserved charges and μ_i are the chemical potentials relative to every conserved charge. H is the Hamiltonian of a Hadron Resonance Gas (HRG) used to describe the interaction of the strongly interacting medium and it is able to reproduce the equation of state obtained with lattice QCD methods [81] before the phase transition to a deconfined state over a significant range of temperature values [72, 82]. In this approximation, the HRG is modelled as composed of non-interacting hadrons and resonances. The QCD equation of state predictions for the HRG and the lattice QCD models are shown in Fig. 2.5. It is important to stress that the latter condition requires the system density to be extremely low: in this approximation, repulsive and attractive interactions can be considered as negligible. Additionally, the repulsive corrections have been modelled as van der Waals eigenvalue corrections [83]. The latter correction is still under active research: in particular, it is difficult to neglect or model the interactions of light (anti)nuclei.

In the strongly interacting medium produced in relativistic heavy-ion collisions, the primary conserved quantum numbers are the electric charge Q, the strangeness S and the baryon number B. One of the critical elements to accurately predict the highest temperature values that the medium can reach is the choice of the mesonic, baryonic and resonance states to be used as input in the Hamiltonian. The total partition function Z of the system is given by the product of all partition functions Z_i of the particle states included in the

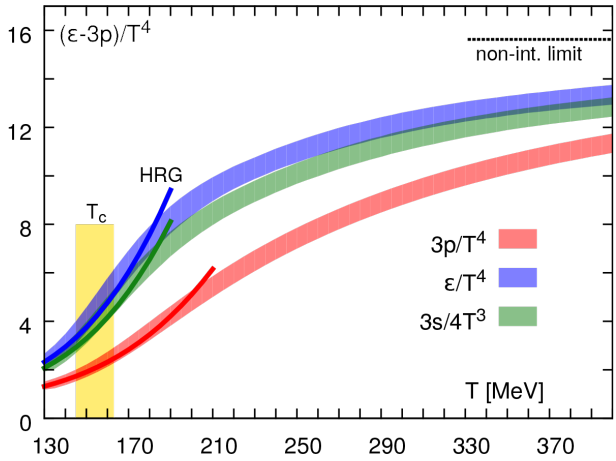

Figure 2.5: The QCD equation of state [84] as predicted by the HRG model (solid lines) and from lattice QCD (bands) [81]. The dashed horizontal line is the non-interacting gas limit for the energy density. The yellow vertical band is the crossover region.

HRG [65, 66]:

$$Z(T,V,\mu) = \prod_i Z_i(T,V,\mu_i) \longrightarrow \log Z(T,V,\mu) = \sum_i \log Z_i(T,V,\mu_i) \ . \tag{2.6}$$

The (logarithm of the) partitions functions Z_i are defined as

$$\log Z_i(T,V,\mu_i) = \frac{V g_i}{2\pi} \int_0^\infty \pm p^2 \ \mathrm{d}p \log\left(1 \pm \lambda_i(T,\mu_i)\, e^{-\beta\epsilon_i}\right) , \tag{2.7}$$

where g_i is the spin-isospin degeneracy factor, m_i is the mass of the i^{th} particle state, $\epsilon_i = \sqrt{m_i^2 + p^2}$ is the energy of a i^{th} particle state of momentum p. The sign $\pm$ in Eq. 2.7 takes account of the bosonic (-) or fermionic (+) nature of the particles. The chemical potential dependence is also encoded in the fugacity λ_i, which is defined as

$$\lambda_i(T,\mu_i) = \exp\left\{\beta\left(B_i\mu_B + S_i\mu_S + Q_i\mu_Q\right)\right\} = \exp\{\beta\mu\}, \text{ with } \beta = \frac{1}{T} \tag{2.8}$$

where B_i, S_i and Q_i are the baryonic number, the strangeness number and the electric charge of the i^{th} particle species, while μ_B, μ_S and μ_Q are the respective chemical potentials. In all the equations, the Boltzmann constant k_B is assumed to be equal to unity, and it is not shown. The logarithm can be Taylor-expanded and after the momentum integration, the previous partition function for the species i becomes

$$\log Z_i(T,V,\mu_i) = \frac{V g_i}{2\beta\pi^2} \sum_{k=1}^{\infty} \frac{(\pm 1)^{k+1}}{k^2} \lambda_i^k m_i^2 K_2(k\beta m_i) \text{, with } \beta = \frac{1}{T} \tag{2.9}$$

where K_2 is the modified Bessel function of the second kind. The sign depends on the Bose-Einstein or the Fermi-Dirac statistical distribution of the particles, while the first term corresponds to the Boltzmann approximation.

The average number $\langle N_i \rangle$ of particles i in volume V at the temperature T for a system described by the grand canonical ensemble is obtained from Eq. 2.9 as

$$\langle N_i \rangle^{th} (T, V, \mu) = \frac{1}{\beta} \frac{\partial}{\partial \mu_i} \log Z_i (T, V, \mu_i) = \frac{V g_i}{2\beta\pi^2} \sum_{k=1}^{\infty} \frac{(\pm 1)^{k+1}}{k} \lambda_i^k m_i^2 K_2 (k\beta m_i) \ . \quad (2.10)$$

The Eq. 2.10 does not describe completely the measured particle yield in heavy-ion collisions: to compare the measured yield with the theoretical prediction it is necessary to account for the additive terms due to feed-down contribution from resonant states (j) that decay in a particle of a species i. If $\Gamma_{j \to i}$ is the branching ratio of the $j \to i$ decay, then the total average number of particles is

$$\langle N_i \rangle (T, V, \mu) = \langle N_i \rangle^{th} (T, V, \mu) + \sum_j \Gamma_{j \to i} \langle N_j \rangle^{th} (T, V, \mu) \, . \quad (2.11)$$

The Eq. 2.11 explicitly points out that, with this approximation, the particle yields depend only on five parameters: the temperature T, the volume V and the three chemical potentials μ_i. In a heavy-ion collision, some parameters are constrained. The μ_Q is fixed by the isospin of the initial stage. Due to the null valence strangeness content of the colliding nuclei, μ_S is null (and fixed). The volume dependence is removed if the yield ratios between different species are compared instead of the production yields. As the number of baryons inside the interaction region is strongly dependent on the energy of the colliding system, the baryochemical potential μ_B is not constrained by the initial conditions.

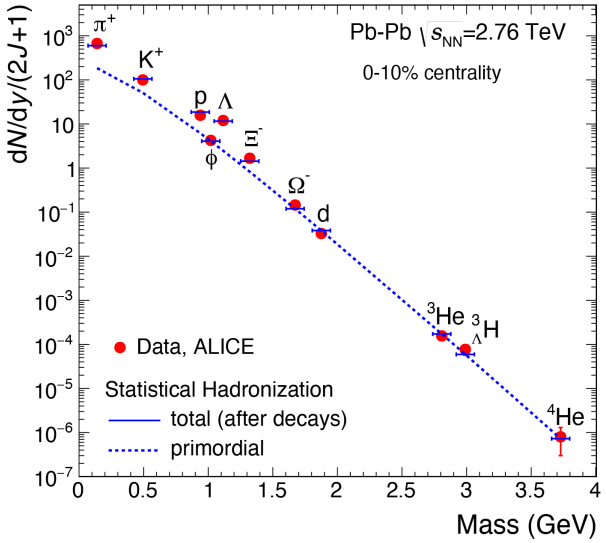

Figure 2.6: Hadron yields as a function of mass, normalised by the spin degeneracy factor $(2J + 1)$ [65]. Comparison with predictions of the SHM (particles only, no anti-particles). The (red points) are measurements in central Pb–Pb collisions at $\sqrt{s_{\rm NN}} = 2.76$ TeV by the ALICE Collaboration. The figure shows both the *total yields*, comprehensive of all contributions from strongly-decaying resonances, and the *primordial yields*, without strong and electroweak decays contributions.

The SHM allows us to predict hadron yields in a wide range of mass, from pions up to (anti)(hyper)nuclei. The mass dependence of hadron yields compared with predictions of the SHM is shown in Fig. 2.6. The yields measured in central Pb–Pb collisions at $\sqrt{s_{\rm NN}} = 2.76$ TeV are normalized by the spin degeneracy factor $(2J + 1)$ [65]. The yields show an exponential dependence on mass M and temperature T. Heavy particles, characterised by $M \gg T = 155$ MeV, are not significantly affected by feed-down and the yield scales as $\mathrm{d}N/\mathrm{d}y \sim M^{3/2} \exp(-M/T)$, while lighter particles as π, K, p deviate from this distribution due the resonance decay contributions. In particular, the small feed-down that contributes to the light nuclei yields is due only to rare hypernuclei decays. This deviation is shown in the figure by comparing the total yields of different species (in blue markers) with the primordial-only predicted yields (dashed line).

The SHM also describes the yields of light (anti)nuclei in spite of their binding energy being much lower than the freeze-out temperature of the medium [65, 85]. The predicted yields are determined by their distribution in the phase space and not by the hadron internal structure. Another successful feature of the SHM is the correct prediction of the antimatter-over-matter ratio as a function of the energy per nucleon pair at the centre of mass. As shown in Fig. 2.7 (left panel), at low collision energy, the baryochemical potential is significantly higher than zero, so antimatter production is suppressed. At high energy, the baryochemical potential is null and the amount of antimatter and matter is equal. In Fig. 2.7 (right panel) the normalised (hyper)(anti)nuclei yield is shown as a function of the $\sqrt{s_{\rm NN}}$ of the collisions. The production yield of ^{3}He at LHC energies is significantly lower then at lower $\sqrt{s_{\rm NN}}$ values (low to 0.1 TeV). As the energy increases, the production yield increases proportionally to the $\sqrt{s_{\rm NN}}$ values.

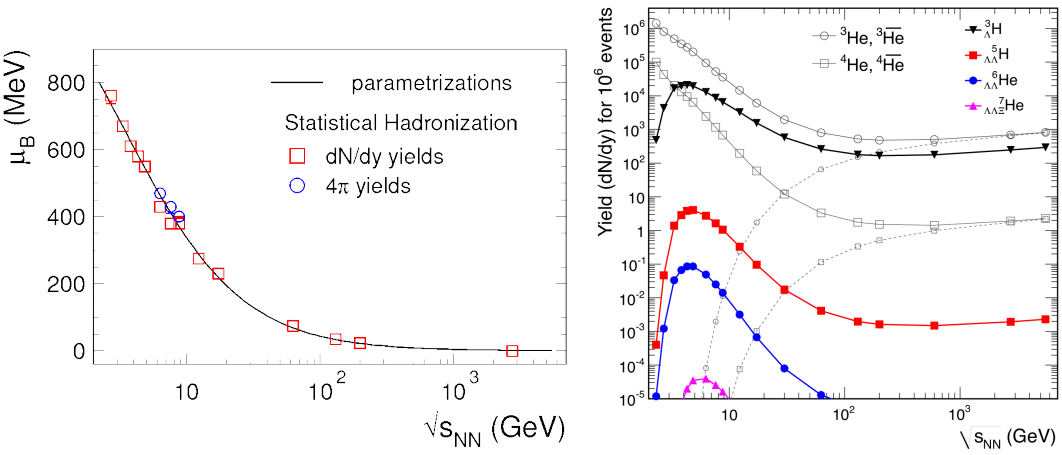

Figure 2.7: (Left) The energy dependence of the baryochemical potential μ_b obtained from the analysis of hadron yields for central AA collisions at different energies. The parametrisation is $\mu_B = a/(1 + 0.288\sqrt{s_{\rm NN}})$, with $a = 1.298$ MeV (plot adapted from [65]). (Right) SHM predictions for the production yields of (anti)(hyper)nuclei with mass number $A \geq 3$ as a function of the collision energy [65].

2.2.2 Canonical Statistical Hadronisation Model

The SHM is also used to model smaller systems, like e^+e^- or pp collisions. These systems do not satisfy the grand canonical formalism conditions as they are characterised by a small reaction volume. This requires imposing a stricter charge conservation. As the number of particles with a conserved charge is of the order of unity, the local charge conservation must be imposed, switching from a grand canonical ensemble formalism - in which the charges are conserved on average - to a canonical ensemble in which the charge number does not fluctuate from a state to another as it is exactly conserved. The immediate consequence of this change of paradigm is that the number of particles that carry the conserved charges is suppressed with respect to the grand canonical approach: hence, the name of *canonical suppression* for this approach. An implementation of the canonical statistical models (CSMs) will be briefly discussed in this Section.

The system is modelled as an ideal HRG in full thermodynamical equilibrium, like in the GC approach discussed in Section 2.2.1. In the canonical approach [66, 86], the conserved charges (Q, B and S) are set to fixed values, which are conserved inside the correlation volume V_c. Given the system temperature T and the correlation volume V_c, the partition function can be written as

$$\begin{aligned} Z(B,Q,S) = &\int_{-\pi}^{\pi} \frac{\mathrm{d}\phi_B}{2\pi} \int_{-\pi}^{\pi} \frac{\mathrm{d}\phi_Q}{2\pi} \int_{-\pi}^{\pi} \frac{\mathrm{d}\phi_S}{2\pi} e^{-i(B\phi_B+Q\phi_Q+S\phi_S)} \\ &\times \exp\left[\sum_k z_k^1 e^{i(B_k\phi_B+Q_k\phi_Q+S_k\phi_S)}\right] \end{aligned} \tag{2.12}$$

where Q_k, B_k and S_k are the charges carried by the k species and the sum is performed on all the k species contained in the HRG. The z_k^1 is the single-particle particle function for the k species:

$$z_k^1 = V_c \int \mathrm{d}m \rho_k(m) g_k \frac{m^2}{2\beta\pi^2} K_2\left(\frac{m}{T}\right) , \tag{2.13}$$

where ρ_k is the mass distribution of the k species, which is introduced to correct for the resonance finite width, K_2 is the modified Bessel function and g_k is the spin-isospin degeneracy factor.

With the use of the Boltzmann limit of Fermi and Bose statistics, it can be shown [87] that the mean particle multiplicity of the k species calculated using the canonical ensemble $\langle N_k^{th}\rangle^{ce}$ is

$$\left\langle N_k^{th}\right\rangle^{ce} = \frac{Z(Q-Q_k, B-B_k, S-S_k)}{Z(Q,B,S)} \left\langle N_k^{th}\right\rangle^{gce} \tag{2.14}$$

where $\langle N_k^{th}\rangle^{gce}$ is the mean particle multiplicity of the k species calculated using the grand canonical ensemble and setting the volume equal to V_c. The ratio that connects the mean particle multiplicity in the canonical formalism to the one in the grand canonical formalism is called the *chemical factor* and it evidences the exact local charge conservation. Following Eq. 2.11, the total particle yield is obtained with the addition of feed-down contributions from resonant states:

$$\langle N_k\rangle^{ce} = \left\langle N_k^{th}\right\rangle^{ce} + \sum_j \Gamma_{j\to k} \left\langle N_j^{th}\right\rangle^{ce} \quad . \tag{2.15}$$

where $\Gamma_{j\to k}$ is the is the branching ratio of the $j \to k$ decay.

One of the main effects of canonical suppression is the strong suppression of strange particle yields. The study in Ref. [66] and [88] considered for the first time the canonical suppression effects at LHC energies with the presence of light (anti)nuclei among the produced particle states. In the integration over the mass distribution ρ_k in Eq. 2.13, the energy-dependent Breit-Wigner model [89] is used. This choice has negligible effects on light (anti)nuclei yields - weakly affected by the feed-down states - but introduces a 15% correction on proton yields. The calculations of this study were performed within the Thermal-FIST [90] framework. The canonical ensemble HRG model is used here, imposing the exact null values of the conserved charges, $Q = B = S = 0$, as the net-baryon content of particles at midrapidity at the LHC is null (as shown in the previous Section in Fig. 2.7).

Depending on the chemical freeze-out temperature and correlation volume in rapidity choice, this model can have different implementations. The pivotal choice of the correlation volume V_c in units of rapidity $\mathrm{d}V/\mathrm{d}y$ ($V_c = k\ \mathrm{d}V/\mathrm{d}y$) shows the necessity to relate the mean multiplicities calculated in the CSM to the rapidity densities that are measured experimentally [66].

The *vanilla CSM* is modelled assuming a full chemical equilibrium at the chemical freeze-out temperature of $T = 155$ MeV, as estimated in central heavy-ion collisions. The dependence of the yields on the charged-particle multiplicity is due to the canonical suppression. The correlation volume range is $V_c = 1 - 6\ \mathrm{d}V/\mathrm{d}y$. The results obtained with this model [88] are shown in Fig. 2.8. The data are taken from ALICE at the LHC. Different curves represent different choices of V_C. The different colours represent different collision systems: pp at $\sqrt{s} = 7$ TeV (in green), p–Pb at $\sqrt{s_{\mathrm{NN}}} = 5.02$ TeV (in blue), Pb–Pb at $\sqrt{s_{\mathrm{NN}}} = 2.76$ TeV (in red). The ratios Λ/π, Ξ/π and Ω/π are well predicted, while the comparison of K/π with data is significantly worse at low multiplicity. The ϕ/π shows another problem of this model: the neutral ϕ is unaffected by the strangeness suppression (as the strangeness charge S is null due to the particle quark composition $\phi = s\bar{s}$), while the pions π are suppressed: this predicts a strong increase of the ratio at low multiplicity, while the data show an opposite trend. At the same time, the CSM predicts the suppression of the nuclei-over-proton ratios at the lower multiplicities and this is achieved for $V_c = 3\ \mathrm{d}V/\mathrm{d}y$.

The issues of the vanilla CSM can be addressed by developing a slightly more sophisticated model, the γ_S-*CSM* [91, 92]. It can be hypothesised that the chemical freeze-out temperature varies with the system size, with smaller systems having a higher temperature. As a consequence, the decoupling of the inelastic hadronic reactions would happen earlier. The shorter lifetime of the hadronic phase is also supported by the extracted T_{kin} values from blast-wave fits to the p_{T} spectra of measured pions, kaons and protons, as larger T_{kin} (~ 170 MeV) are observed in pp collisions with respect to central Pb–Pb collisions (~ 100 MeV).

The overestimation of the ϕ/π ratio and the K/π observed in pp collisions data can be due to incomplete chemical equilibrium. This can be approached with the inclusion of a strangeness saturation factor γ_S to account for a chemical freeze-out temperature T_{chem} with a strangeness freeze-out temperature lower with respect to T_{chem}. Two parametrisations have been extracted from the measured data, one for the chemical freeze-out and one

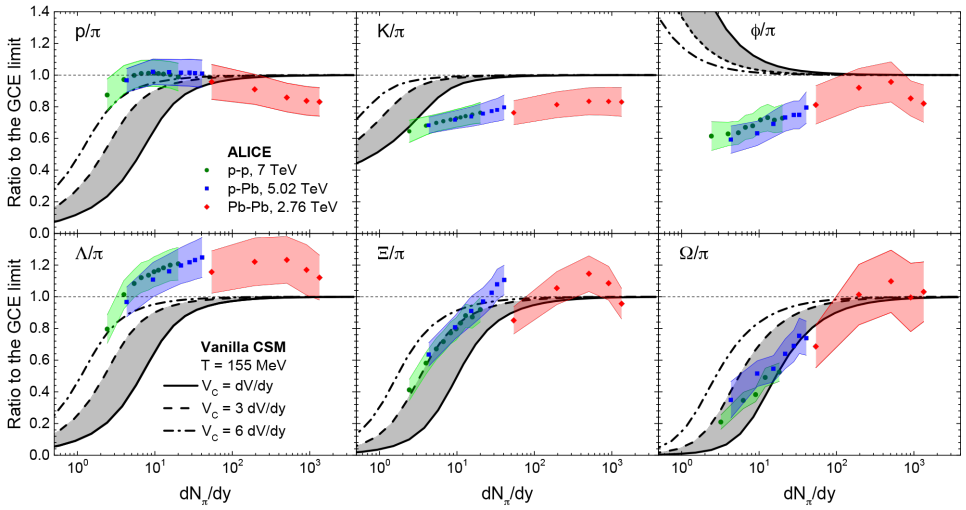

Figure 2.8: The ratios of hadron-to-π yields as a function of the pion multiplicity at midrapidity, using the vanilla CSM with exact conservation of Q, B and S in different colliding systems [88]. The results and data are scaled by the GCE limit values evaluated in the CSM, with $T = 155$ MeV and $\mu_B = 0$.

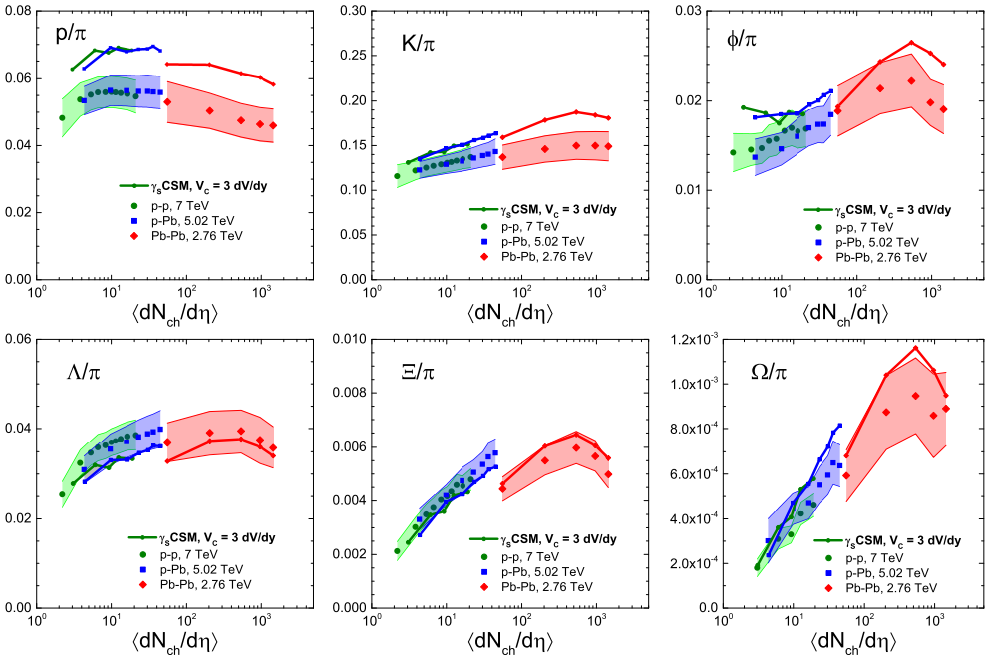

Figure 2.9: The ratios of hadron-to-π yields as a function of the charged particle multiplicity evaluated in the γ_S-CSM with $V_c = 3\,\mathrm{d}V/\mathrm{d}y$ for the thermal parameters extracted for each multiplicity in different colliding systems [88].

from the strangeness saturation parameter. The temperature can be estimated [88] as

$$T = T_0 - \Delta T \ln(\mathrm{d}N_{\mathrm{ch}}/\mathrm{d}\eta) \tag{2.16}$$

with $T_0 = (176 \pm 1)$ MeV, $\Delta = (2.6 \pm 0.2)$ MeV and $\mathrm{d}N_{\mathrm{ch}}/\mathrm{d}\eta$ is the charged multiplicity (per unit of pseudorapidity).

The strangeness saturation parameter γ_S [88] is

$$\gamma_S = 1 - \exp\left[-\frac{\mathrm{d}N_{\mathrm{ch}}/\mathrm{d}\eta}{B}\right] \tag{2.17}$$

where $B = 59 \pm 6$.

The volume parameter in this model [88] is linearly proportionally to the multiplicity per unit of pseudorapidity $\mathrm{d}N_{\mathrm{ch}}/\mathrm{d}\eta$:

$$\mathrm{d}V/\mathrm{d}\eta = v\ \mathrm{d}N_{\mathrm{ch}}/\mathrm{d}\eta,\ v = (2.4 \pm 0.2)\ \mathrm{fm}^3\,. \tag{2.18}$$

The results of the γ_S-CSM calculation are shown in Fig. 2.9, where the ratios of hadron-to-π yields are shown as a function of multiplicity and compared to ALICE data.

2.3 Coalescence model

In the coalescence model, the nucleons generated in the collision bind into a nucleus if they are spatially close and have similar velocities. In the last sixty years, coalescence models have been used to describe the formation of different composite objects. The model was developed by Butler and Pearson [67] for proton-nucleus collisions: they suggested that the capture and binding of nucleons produced in presence of the target nuclear optical potential could be the origin of the measured deuteron production. Coalescence has been further developed by Kapusta [68] and used to study the production of deuteron in relativistic nuclear collisions. The interaction diagrams for these models are shown in Fig. 2.10.

The probability of nucleons to merge via coalescence can be experimentally defined as the coalescence parameter B_A:

$$E_A \frac{d^3N_A}{dp_A^3} = B_A \left(E_p \frac{d^3N_p}{dp_p^3} \right)^Z \Bigg|_{\vec{p}_p = \frac{\vec{p}_A}{A}} \left(E_n \frac{d^3N_n}{dp_n^3} \right)^N \Bigg|_{\vec{p}_n = \frac{\vec{p}_A}{A}} \tag{2.19}$$

where $A = Z + N$ is the mass number, $p_{p,n}$ are the proton and neutron momenta and $E_{p,n}$ their energies. Hence, the coalescence parameter B_A is the key parameter of coalescence approach. The term on the left is the invariant production spectra of nuclei with mass number A, while the term on the right is the coalescence parameter times the invariant production spectra for primary protons, elevated to the mass number. Theoretically, the proton and neutron invariant spectra must be considered separately. As at the LHC energies the isospin chemical potential is null, than neutrons and protons belong to the same isospin multiplet and, therefore, yields of protons and neutrons are the same. This comes in assistance of the ALICE measurements, as the stable neutral particles cannot be detected (excluding a limited acceptance covered by hadronic calorimeters).

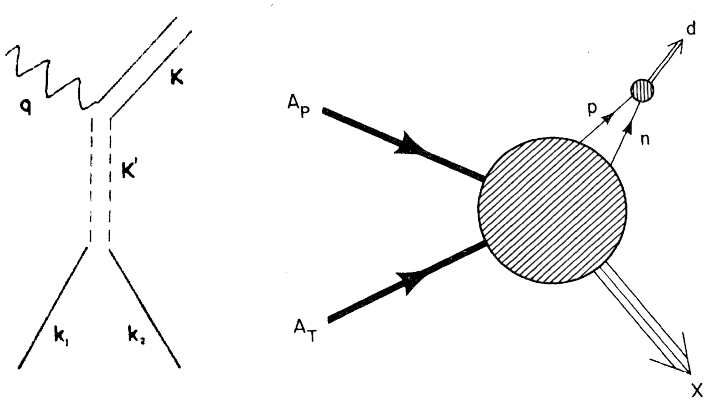

Figure 2.10: (Left) Butler and Pearson's diagrams of nucleons interacting with each other to form an intermediate deuteron state. $\mathbf{k_1}$, $\mathbf{k_2}$ are the momenta of the nucleons in the initial state, $\mathbf{q}$ is the recoil of the nucleus and $\mathbf{K}$ is the deuteron momentum in the final state (adapted from [67]). (Right) Kapusta's [68] schematic diagram for the production of a deuteron in the final state of a relativistic collision between two nuclei.

2.3.1 Simple coalescence

The simplest coalescence model to build is a model in which the coalescence probability is assumed independent of the momentum and of the object size relative to the size of the nucleons emitting source. This is called *simple* coalescence or *naive* coalescence. The model premises imply that it is sufficient for two nucleons to bind to be close in momentum space, regardless of their distance in space. Considering the deuteron, as an example, its formation in this model is assumed to happen if a proton and a neutron have a momentum difference $\Delta\vec{p} = |\vec{p}_p - \vec{p}_n| < p_0$, with p_0 being a constant value that sets a threshold for the coalescence process.

Experimentally, this approximation proved to be valid for pp and p–Pb [20, 93, 94], but it fails Pb–Pb collisions. This can be interpreted as the fact that in small systems the simple model assumptions are plausible because the colliding system size is comparable with the size of the nucleus (since nucleons are produced close to each other). In particular, the emitting source of colliding systems such as e^+e^- or pp, in the simple coalescence is considered point-like. This approximation holds as long as the source is smaller than the produced particle.

Larger systems show a strong dependence of the coalescence probability with the centrality, which suggest a dependence with the size of the source, as nucleons can be produced with a significant distance from each other and hence not being able to coalesce into a nucleus, even with similar momenta. Additionally, the naive coalescence cannot fully explain the elliptic flow of deuterons [95].

2.3.2 Coalescence based on Wigner function formalism

More advanced models [96, 97] do not neglect the finite size of the nucleon source: two nucleons close in momentum value may not interact due to the space distance from which are emitted. In a full quantum-mechanics description of the interaction processes, the classical phase space representation of the nucleus is replaced with its Wigner function, obtained by the Wigner transform of the wave functions. The probability of coalescence is due to the the overlap between the wave functions of the nucleons and the wigner functions of the nucleus.

In the simplest case, that of the deuteron (p,n), the internal deuteron wave-function $\varphi_d(\vec{r})$ is

$$\varphi_d(\vec{r}) = \left(\pi r_d^2\right)^{-3/4} \exp\left(-\frac{r^2}{2r_d^2}\right), \tag{2.20}$$

where the characteristic-size parameter for deuteron is defined as $r_d = \sqrt{8/3}\lambda_d$, where λ_d is the rms of the wave-function of the deuteron. As the harmonic-oscillator approximation is used, the resulting Wigner function is Gaussian and allows for analytical solutions. For point-like constituents, the generic characteristic size parameter for $A > 2$ nuclei [98] is

$$\lambda_A^2 = \frac{3}{2}\frac{A-1}{A}\frac{r_A^2}{2}. \tag{2.21}$$

The choice of the gaussian function is not the only option: further studies addressed the topic through more realistic wave-functions, like the Hulthen parametrisation [99, 100] for deuterons, or Λ-deuteron for the hypertriton [101, 102].

The quantum-mechanical nature of the nuclei is explicitly accounted for with an average correction factor $\langle C_A \rangle$. The correction factor is defined as

$$\langle C_A \rangle = \prod_{i=1,2,3} \left(1 + \frac{r^2}{4R_i^2}\right)^{-\frac{1}{2}(A-1)} . \tag{2.22}$$

The correction factor for a deuteron can be approximated as:

$$\langle C_d \rangle \approx \frac{1}{\left[1 + \left(\frac{r_d}{2R_\perp(m_T)}\right)^2\right] \sqrt{1 + \left(\frac{r_d}{2R_\parallel(m_T)}\right)^2}} \tag{2.23}$$

where r_d is the size parameter, $R_\perp$ and $R_\parallel$ are respectively the transverse and longitudinal *homogeneity radii* [96] of the coalescence volume (measured via Hanbury Brown-Twiss interferometry [103]) and represent the space-time variances of the source, while $m_T = \sqrt{m^2 + p_{\mathrm{T}}^2}$ is the *transverse mass* of the nucleons. The coalescence parameter B_2 for deuteron can be explicitly expressed as a function of the source dimension [96]:

$$B_2 = \frac{3\pi^{3/2}\langle C_d \rangle}{2m_T R_\perp^2(m_T) R_\parallel(m_T)} \tag{2.24}$$

Using the $R \approx R_\perp \approx R_\parallel$ approximation (isotropic source), Eq. 2.23 and Eq. 2.24 become

$$B_2 = \frac{3\pi^{3/2}\langle C_d \rangle}{2m_T R^3(m_T)}, \qquad \langle C_d \rangle \approx \left[1 + \left(\frac{r_d}{2R(m_T)}\right)^2\right]^{-3/2} . \tag{2.25}$$

The variation of B_2 and $\langle C_d \rangle$ as a function of the source volume is illustrated in Fig. 2.11, using different values for the characteristic size parameter r_d. For $r_d = 0$ (point-like approximation), the quantum-mechanical correction factor is equal to one. For not null values of r_d, $\langle C_d \rangle$ increases with R and, for large source size, it reaches unity asymptotically. The choice of r_d affects the slope as larger r_d will cause a slower rise. For low R values the coalescence parameter is dominated by the correction factor, reaching a finite value if the source size tends to zero. For $R \gg r_d$, the coalescence parameter is instead dominated by the classical phase-space separation and this causes the coalescence probability to decrease at large distances in configuration space. The experimental data used for a comparison ($r_d = 3.2$ fm) corresponds to a rms radius of the deuteron wave-function $\lambda_d = (2.1413 \pm 0.0025)$ fm. The value $r_d = 10$ fm has been chosen as a reference as it is completely unrealistic. The dotted vertical line in the plot corresponds to the inflection point of $\langle C_d \rangle$, in $R = r_d/\sqrt{6}$, if $r_d = 3.2$ fm.

According to Ref. [96, 102, 104], Eq. 2.23 can be extended to nuclei with $A > 2$.

Eq. 2.22 can be used together with the subsequent equations from Ref. [96] for this purpose. Once the homogeneity volume V_{hom}(Eq. 2.23) (extracted from HBT measurements with pairs of identical hadrons) is known, then the effective volume V_{eff} in the cluster spectrum can be extracted as

$$V_{eff}(A, M_T) = \left(\frac{2\pi}{A}\right)^{3/2} V_{hom}(m_T) \tag{2.26}$$

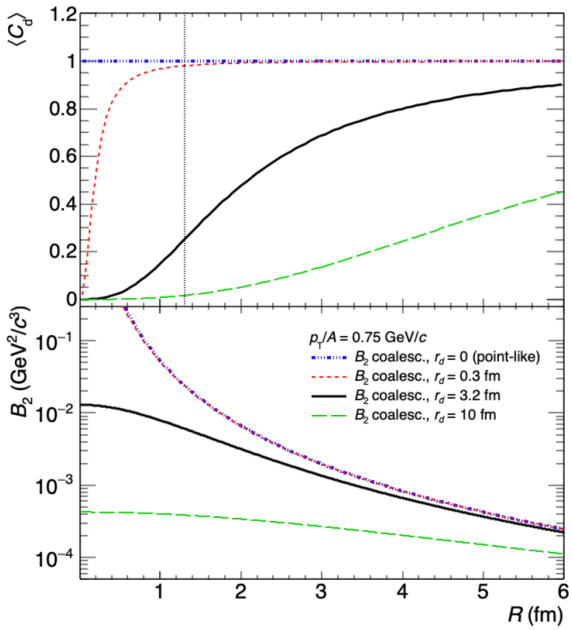

Figure 2.11: Quantum-mechanical correction factor $\langle C_d \rangle$ and coalescence parameter B_2 for the deuteron as a function of the radius of the source R, calculated with different size parameters: $r_d = 0$; 0.3; 3.2 and 10 fm [97].

where $M_T = A\ m_T$ is the transverse mass of the cluster. The coalescence parameter B_A hence can be written as

$$B_A = \frac{2J_A + 1}{2^A} A \langle C_A \rangle \frac{V_{eff}(A, M_T)}{V_{eff}(1, m_T)} \left(\frac{(2\pi)^3}{m_T V_{eff}(1, m_T)} \right)^{A-1} \tag{2.27}$$

and combining the latter with Eq. 2.22 and the $R \approx R_i$ approximation, it is obtained

$$B_A = \frac{2J_A + 1}{2^A} \frac{1}{\sqrt{A}} \frac{1}{\sqrt{m_T^{A-1}}} \left(\frac{2\pi}{R^2 + (r_A/2)^2} \right)^{\frac{3}{2}(A-1)} \tag{2.28}$$

which is a general formula that is used to compare the predicted B_A with the experimental data (Eq. 2.19).

An alternative formulation to the source-size dependent coalescence [100] is based on the description of femtoscopic correlations between nucleons [105]. The model assumes that the high excitation state produced at the high energy collision when reached the kinetic freeze out can be described by a multi- particle quantum-mechanical density matrix. The projection of the density matrix onto particle states at the detector gives the observed particle spectra. The bound-state multi-nucleon final state solutions of the final state interactions constitute the observed nuclei. This framework is here applied to the study of the deuteron coalescence. Once the normalised two-particle source $\mathcal{S}_2$, a function in the

pair-rest frame coordinate $\mathbf{r}$ is defined as an integral in $t = r^0$,

$$\mathcal{S}_2(\mathbf{r}) = \frac{\int dr^0 \tilde{S}_{p_1,p_2}(0,r)}{\int d^4r\, \tilde{S}_{p_1,p_2}(0,r)}. \tag{2.29}$$

and being p the momentum of the nucleus and $w_s = (2s+1)/(2s_N+1)^2$ the spin weights, then the coalescence parameter B_2 for the deuteron can be analytically estimated in this framework by

$$B_2 \approx \frac{2((2s_d+1))}{m(2s_N+1)}(2\pi)^3 \int d^3\mathbf{r}|\phi_d(\mathbf{r})|^2 \mathcal{S}_2(\mathbf{r}) \tag{2.30}$$

$$\approx \frac{2((2s_d+1))}{m(2s_N+1)} \int d^3\mathbf{k}\mathcal{F}_d(\mathbf{k}) C_2(p,\mathbf{k}) \tag{2.31}$$

where $C_2(p,\mathbf{k})$ is the momentum space correlation function, which is the Fourier transform of $\mathcal{S}_2(\mathbf{r})$,

$$C_2(p,\mathbf{k}) = \int d^3\mathbf{r} \exp(i\mathbf{k}\mathbf{r})\mathcal{S}_2(\mathbf{r})\,, \tag{2.32}$$

and $\mathcal{F}_d$ is the momentum space deuteron form factor, which is connected to the deuteron wave-function ϕ_d as

$$|\phi_d(\mathbf{r})|^2 = \int d^3\mathbf{k} \frac{1}{(2\pi)^3} \exp(i\mathbf{k}\mathbf{r})\mathcal{F}_d(\mathbf{k}). \tag{2.33}$$

2.3.3 B_A and ^{3}He/p as a function of p_{T}

The ALICE experiment performed different campaigns of measurement of the (anti)nuclei spectra and the relative coalescence parameters, which are experimentally accessible using the invariant yields of protons and that of nuclei, according to the equation

$$E_A \frac{d^3N_A}{dp_A^3} = B_A \left(E_{p,n} \frac{d^3N_{p,n}}{dp_{p,n}^3} \right)^A \Bigg|_{\vec{p}_p = \vec{p}_n = \frac{\vec{p}_A}{A}}, \tag{2.34}$$

which is a simplified version of Eq. 2.19 that is valid at LHC due to the expected isospin symmetry. As state-of-the-art coalescence models (Section 2.3.2) predict a dependence on the spatial separation of the nucleons emitted in a collision, in order to investigate the dependence of the coalescence probability on the size of the source, the measurements have been performed at different energies and in different colliding systems.

The coalescence parameter B_2 and B_3 are shown in Fig. 2.12 as a function of the charged-particle multiplicity for a fixed value of p_{T}/A. The left panel shows the evolution of B_2 as a function of multiplicity, while the right panel shows the evolution of B_3. Data are compared with the theoretical predictions from [97]. The first parametrisation (A) is a data-based parametrisation that uses a fit of the ALICE measurements of the system radii R from femtoscopic measurements [106] as a function of multiplicity, while parametrisation B has the system radius and the multiplicity constrained to fit the measured data from Pb–Pb collisions at $\sqrt{s_{\mathrm{NN}}} = 2.76$ TeV in the high centrality class (0-10%). The theoretical

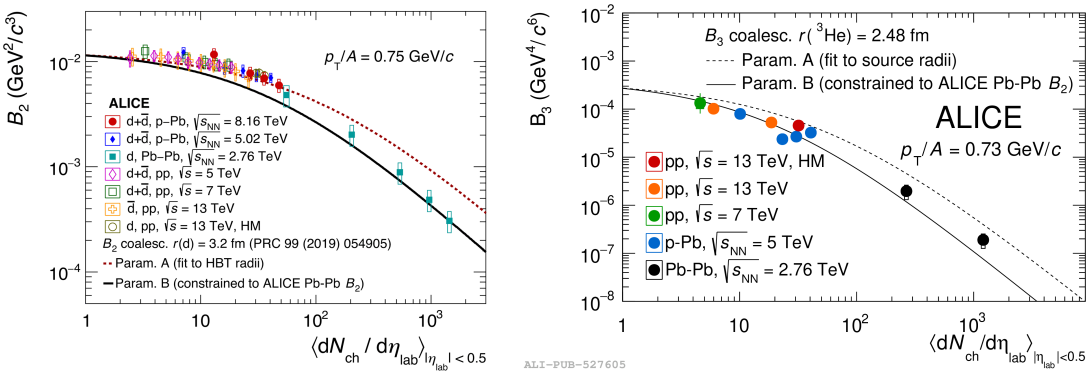

Figure 2.12: (Left panel) The coalescence parameter B_2 at $p_T/A = 0.75$ GeV/c as a function of multiplicity in different collision systems. (Right panel) The coalescence parameter B_3 at $p_T/A = 0.73$ GeV/c as a function of multiplicity in different collision systems.

predictions are estimated setting the radius of the deuteron $r_d = 1.96$ fm and the radius of the helium $r_{^3\mathrm{He}} = 1.76$ fm.

The measurements show the dependence of the coalescence probability on the charged particle multiplicity: at low multiplicity (e.g. pp and p–Pb) a weak dependence on multiplicity is observed; at higher multiplicity (Pb–Pb) the data show a significant drop in the coalescence probability. The theoretical models used to fit the data are not able to describe the B_A for the whole range of multiplicity, with both of the proposed parametrisation.

Another measurement performed is the ratio between (anti)nuclei and hadrons produced in the same class of events as a function of the multiplicity [24]. In Fig. 2.13 the ratios of (left) deuterons-over-protons (d/p) and (right) helions-over-protons (^{3}He/p) are shown in all available collision systems at the LHC, as a function of the average charged-particle pseudorapidity density $\langle \mathrm{d}N_{\mathrm{ch}}/\mathrm{d}\eta \rangle$. The data are compared with predictions performed with both the Thermal-FIST CSM and the coalescence model. The ratio increases as the multiplicity increases and eventually saturates at high multiplicities.

The coalescence predictions for ^{3}He are modelled in two different cases: a two-step process in which the helium is formed via coalescence from a deuteron and a proton (two-body) and a (three-body) process in which the three nucleons bind together to form the helium nucleus. The difference between these models is evident at low multiplicity, while at higher multiplicity the models converge. The coalescence model is in strong agreement with deuteron data, while for ^{3}He the agreement is weaker: the two-body model overshoots the data in the whole multiplicity range, while the three-body model overshoots the data at low multiplicity range. Both the coalescence models cannot predict the high multiplicity decreasing trend.

The CSM predictions are performed using two different implementations, both using a correlation volume $V_c = 1.6$ d$V/$dη: the first (i) assuming the system to be in chemical equilibrium and the chemical freeze-out temperature fixed at $T_{\mathrm{chem}} = 155$ MeV, the other (ii) using a more advanced model [24, 107, 108] that considers the annihilation freeze-out temperature to be dependent on $\langle \mathrm{d}N_{\mathrm{ch}}/\mathrm{d}\eta \rangle$. In the d/p ratios, the predictions of (i) show good agreement in the full multiplicity range, but it does not predict the decreasing at

high multiplicity. This behaviour is predicted by (ii), but the values are further from data as compared to the other model. In the ^{3}He/p ratios, both CSM calculations have a worse agreement with respect to the coalescence models.

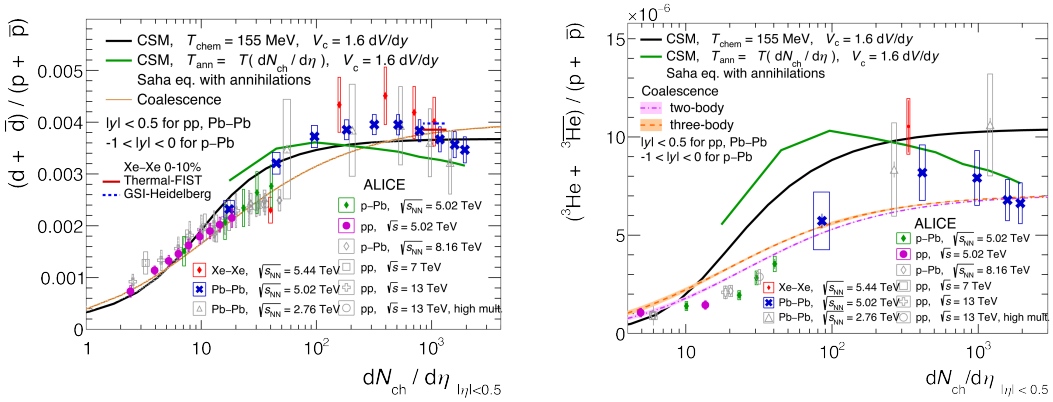

Figure 2.13: (Left panel) Deuteron-to-proton and (right panel) helion-to-proton ratios as a function of the average multiplicity density [24]. All yields are measured at midrapidity. Statistical uncertainties are shown as vertical lines, systematic uncertainties are shown as boxes. The coalescence model predictions are shown as bands, while the black and green lines correspond to different CSM predictions.

Chapter 3

The ALICE experiment

A Large Ion Collider Experiment (ALICE) is one of the main four experiments installed at the LHC at CERN. LHC is the most powerful collider in the world to date. ALICE has been collecting data since 2009 during three different data taking periods called *Runs*: LHC Run 1 (2009–2013), Run 2 (2015–2018) and the Run 3 (2022–ongoing). The runs were punctuated by periods of stop of the data taking used for major maintenance and upgrade of the detector, the *Long Shutdowns* (LS): LS1 (2013–2015) and LS2 (2018–2022). In this section, the Large Hadron Collider (LHC) accelerator complex and the technical details of the ALICE experimental apparatus are described, with a strong focus on the results of the vast upgrade campaign performed during the LS2. The detector was upgraded to keep pace with the high luminosity of the Run 3 data taking campaign. Hence, a full description of the updated performance of the ALICE subdetectors used to measure (anti)nuclei and of the readout system is presented.

3.1 The Large Hadron Collider (LHC)

The Large Hadron Collider (LHC) is part of the complex acceleration system at CERN [109]. The chain of accelerators is able to accelerate particles at energies at every step higher: the accelerated particles travel through all the pre-accelerators up to the LHC collider. The acceleration complex is able to accelerate both protons and heavy nuclei, including lead (Pb), xenon (Xe) and oxygen (O), expected for the 2025 data taking. The high-energy collisions performed at CERN are listed in Tab. 3.1.

Protons are extracted from a negatively ionised hydrogen (H^-) tank and injected into the Linac4, a linear accelerator that boosts the protons up to 160 MeV using a multi-stage radiofrequency-based accelerator chain. The protons are then boosted into the Proton Synchrotron Booster (PSB), where the protons lose two electrons (from H^- to H^+) and are accelerated up to 2 GeV, before being injected in the Proton Synchrotron (PS). In the PS, a 638 m long synchrotron, the protons are accelerated up to 26 GeV and grouped in bunches before getting boosted into the Super Proton Synchrotron (SPS). The SPS is the second-largest machine in CERN's accelerator complex, with a total length of around 7 km. It began its operations in 1976 and is now able to accelerate protons up to 450 GeV before the injection into the LHC.

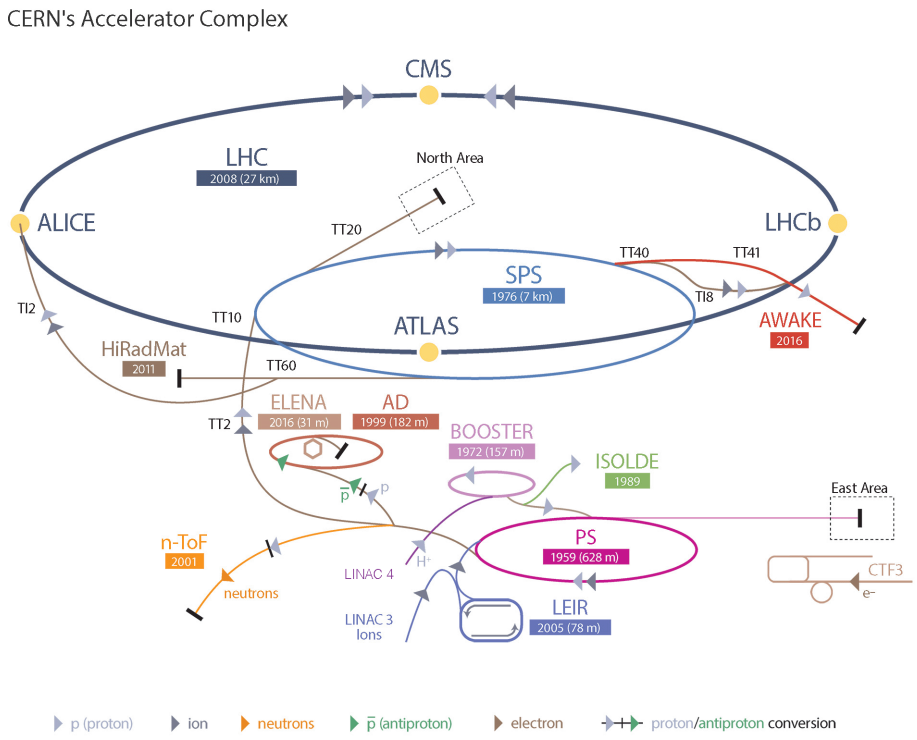

Figure 3.1: Layout of the accelerator complex at CERN. Adapted from [109].

The first phase in the case of lead nucleus acceleration is different. The ^{208}Pb ions are extracted from an isotopically pure source, heated via microwaves up to ~ 500°C, and then partially ionised using an electron flux. The ^{208}Pb ions travel through the Linac3, where they are accelerated up to 4.5 MeV per nucleon before getting injected in the Low Energy Ion Ring (LEIR). There, the beam is grouped into four bunches and accelerated up to 72 MeV per nucleon. The bunches are eventually injected into the PS; then they follow the same acceleration chain as the protons. Two beams travel inside the LHC in opposite directions and collide in four interaction points, one for each of the main LHC experiments: ALICE, ATLAS, CMS and LHCb.

Collision system	Collision energy ($\sqrt{s}$, $\sqrt{s_{\mathrm{NN}}}$) (TeV)
pp	**0.9**, 2.76, 5.02, 7, 8.16, 13, **13.6**
p–Pb	5.02 , 8.16
Pb–Pb	2.76, 5.02, **5.36**
Xe–Xe	5.44
O–O	**6.8**

Table 3.1: Collision systems and energies at the LHC for Run 1, Run 2 and Run 3 (in bold). The O–O data-taking campaign is planned for 2025. Adapted from [75].

The LHC Run 1 physics campaign began in 2009, reaching energies in the centre-of-mass up to $\sqrt{s} = 7$ TeV in pp collisions, energies per nucleon pair $\sqrt{s_{\rm NN}} = 5.02$ TeV in p–Pb collisions and $\sqrt{s_{\rm NN}} = 2.76$ TeV in Pb–Pb collisions. At the end of Run 1 (2013), the Long Shutdown 1 (LS1) began, allowing for a first limited detector update. The LHC Run 2 campaign started in 2015 and it reached energies up to $\sqrt{s} = 13$ TeV in pp collisions, $\sqrt{s_{\rm NN}} = 8.16$ TeV in p–Pb collisions and $\sqrt{s_{\rm NN}} = 5.02$ TeV in Pb–Pb collisions. The LS2 began in 2018 and lasted up to 2021. During the LS2, ALICE underwent a series of updates for the LHC Run 3 data taking campaign [110], which began in 2021. The details about the ALICE apparatus and the LS2 upgrades will be briefly introduced.

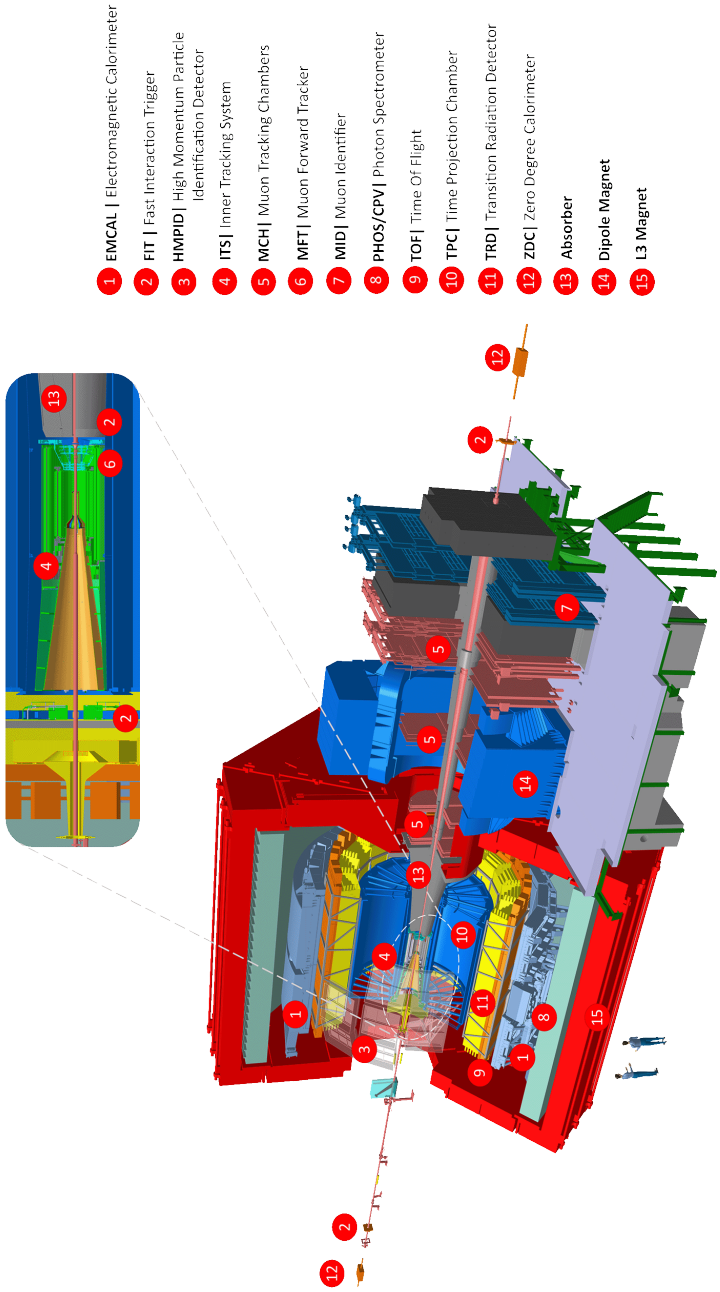

Figure 3.2: The layout of the ALICE apparatus in the LHC Run 3 [110]. The central barrel detectors (ITS, TPC, TRD, TOF, EMCal) are embedded in a magnetic field provided by the L3 solenoidal magnet ($B = 0.5$ T). The forward detectors (MCH, MID, MFT, FIT and ZDC) are used for triggering, event characterisation and multiplicity studies.

3.2 The ALICE detector

The ALICE detector was designed to study the conditions that are thought to have existed immediately after the Big Bang, studying the properties of the strong interaction and characterising the QGP produced in high-energy heavy-ion collisions.

The ALICE experiment is suited to study the physics of different colliding systems (pp, p–Pb, Pb–Pb, ...). Thanks to its apparatus capabilities, the ALICE experiment is able to perform measurement at low momenta (~ 100 MeV/c), and it can work in high-multiplicity environments. In particular, the detector was designed in the late nineties to take account of a predicted multiplicity in the heavy-ion collision of 2000–8000 charged particles per unity of rapidity. After the multiplicity measurement performed in 2001 at RHIC in Au–Au collisions, this value has been corrected down to 1500–4000 charged particles per unity of rapidity $\langle dN_{ch}/d\eta \rangle$ and for this reason, the ALICE experiment is able to work up to $\langle dN_{ch}/d\eta \rangle \sim 4000$.

The ALICE detector is located at the interaction point IP2 of the LHC, and its cavern is 56 m under the ground. The ALICE detector is 16 m high and 16 m wide; it has a length of 26 m along the beam direction and a weight of over 10 000 t.

The subdetectors in the central barrel of ALICE are embedded in a magnetic field of $B = 0.5$ T, generated by a powerful solenoid. The solenoid was previously used in the L3 experiment of the Large Electron-Positron collider (LEP) at the same place in the 1990s, and this is why the magnet is still called L3. The solenoid is a conventional magnet (unlike the LHC superconductive magnets) and requires a current of 30 kA to generate the magnetic field. The moderate magnetic field was chosen to allow the reconstruction of low momentum particles in the main tracker, i.e. down to $p_{\mathrm{T}} \sim 100$ MeV/c for pions.

The central barrel detectors are the Inner Tracking System (ITS2), the Time Projection Chamber (TPC), the Transition Radiation Detector (TRD), the Time of Flight detector (TOF), the High Momentum Particle IDentification detector (HMPID), the Photon Spectrometer (PHOS), the ElectroMagnetic Calorimeter (EMCal), the Di-jet Calorimeter (DCal) and the Charged Particle Veto detector (CPV). These are used for the identification of particles emitted at medium pseudorapidity, η. The ITS2 and TPC are used also for the tracking.

The Muon Tracking Chambers (MCH) and the Muon Identifier (MID) are located in the regions of pseudorapidity $-4 \leq \eta \leq -2.5$, and are used to study the forward particle production from their decay into muons.

The Zero Degree Calorimeter (ZDC), the Muon Forward Tracker (MFT) and the Fast Interaction Tracker (FIT) are placed on each side of the interaction point (IP) on the longitudinal axis (z-axis). The ZDC is used during Pb–Pb collisions to measure the centrality of the collisions. The MFT is a muon spectrometer based on the same silicon pixel technology used for the ITS2, the ALPIDE sensor (more details in Section 3.2.1). The FIT is a multi-array sub-detector that serves as an interaction trigger, online luminometer, and forward multiplicity counter. It is also used to measure the position of the primary vertex of the collision. The FIT is composed of two fast Cherenkov radiators located on both sides of the ALICE IP. The FV0 estimates the centrality of the collisions, whereas the FT0 measures the event time of the collisions (which is necessary also to computer the particle time-of-flight in combination with the TOF detector information, see Section 3.2.3) and

the FDD subsystem estimates the cross sections of diffractive processes. In the subsequent section, the three detectors were exploited for the analyses presented in this thesis.

3.2.1 Inner Tracking System (ITS2)

The ITS is the closest detector to the IP, and it is mounted in close contact with the LHC beryllium beam pipe. It is located in the ALICE central barrel, covering a pseudorapidity range of $|\eta| < 1.3$. The ITS main goals are the reconstruction of the collision primary vertex and the particle tracking. Due to its position, it is also used to reconstruct secondary vertices of the weak decays. During the LS2, the ITS detector used in Run 1 and Run 2 was completely substituted with an upgraded Inner Tracking System, called ITS2. The new ITS2 improves the precision of the reconstruction of the primary vertex, the low-momentum particle tracking performance, and the reconstruction of secondary vertices. In this thesis, both ITS and ITS2 will refer to the upgraded ITS2 used in Run 3.

Thanks to the new ITS2 design, using a lightweight pixel technology, the resolution on the impact parameter and the resolution on the collision vertex position improved due to the reduced distance of the first layer from the LHC beam line.

The first ITS2 layer sits at a radial distance of only 22.4 mm (from the 39 mm of the previous tracker), reducing the distance by a factor of 1.7. The improved spatial resolution on the impact parameter of the track to the primary vertex (PV) in transverse $r\phi$ and longitudinal z (right panel) planes is shown in Fig. 3.3. The parameter resolutions for new ITS2 are shown in Fig. 3.4: the resolution on the transverse $r\phi$ plane (on the left) and on the longitudinal direction z (on the right) as a function of p_{T} are compared with a detailed Monte Carlo simulation produced during the detector commissioning phase. The measured values are compatible within a 20% of the expected resolution performance. The comparison between the $r\phi$ parameter resolution for the old ITS and the new ITS2 is shown in Fig. 3.4. The figure shows a consistent improvement, as for p_{T} below 1 GeV/c, the ITS2 resolution is a factor three better, and at higher momenta, the gain is higher (up to a factor four for $p_{\mathrm{T}} \geq 10$ GeV/c), as shown in Fig. 3.4.

The ITS2 is based on a pixel-silicon sensor called ALPIDE [111] and it is the largest-scale application of Monolithic Active Pixel Sensors (MAPS) [112] in a high-energy physics experiment. The ALPIDE chip is a MAPS implemented in a 180 nm CMOS technology for imaging sensors provided by TowerJazz [113]. The chip dimensions are 15 mm by 30 mm. Every chip includes a matrix of 512×1024 sensing pixels, each one measuring 29.24 µm × 26.88µm ($z \times r\phi$). The interface, the analogue biasing, the control and the readout are implemented in a peripheral region of the chip. The chips are built using a high-resistivity epitaxial layer on the p-type substrate, with a thickness between $18 - 30$µm. The schematic cross-section of a silicon pixel cell is shown in Fig. 3.5 (left): if a charged particle crosses the sensor, charge carriers are diffused in the medium. The electrons released in the epitaxial layer diffuse laterally, while they are vertically confined by potential barriers at the interfaces with the overlying p-wells and the underlying (p-type) substrate. The signal is extracted by the n-well diodes: the electrons that reach the depletion volume of the diode can induce a current at the pixel front-end. The epitaxial layer is isolated from the n-well of the PMOS transistors using a construction process that provides a deep p-well layer: the epitaxial layer would otherwise act as an electron collector, competing with the sensing

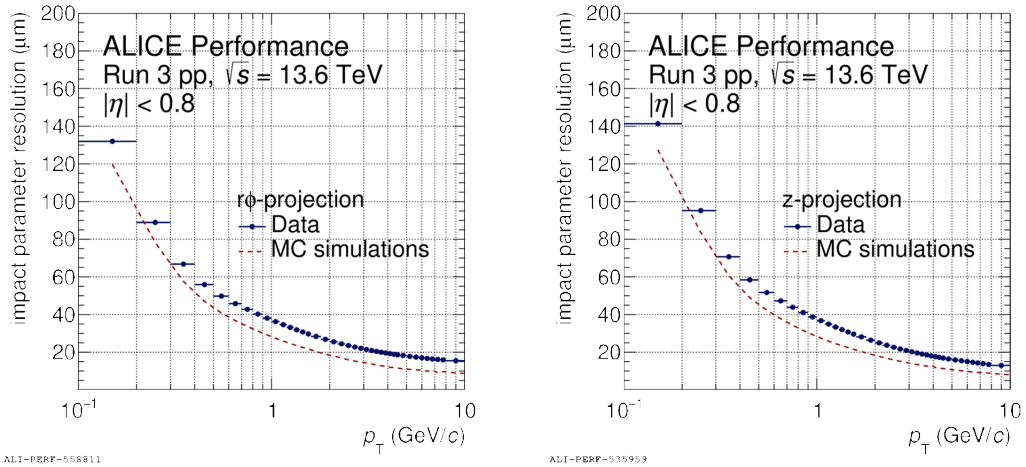

Figure 3.3: Resolution on the impact parameter as a function of the transverse momentum, in the transverse $r\phi$ (left) and the longitudinal z (right) planes, comparing data measured in pp collisions at $\sqrt{s} = 13.6$ TeV (blue) with Monte Carlo simulations (red). Figure credits: ALICE Collaboration.

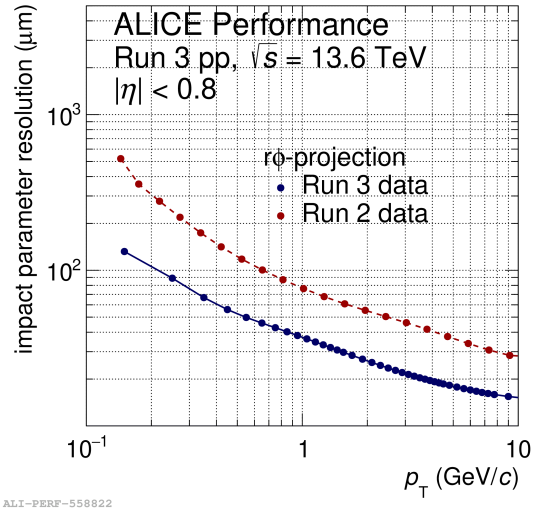

Figure 3.4: Impact parameter resolution in $r\phi$ as a function of p_{T} in pp collisions at $\sqrt{s}$ = 13.6 TeV in Run 3 data (in blue) and at $\sqrt{s}$ = 13 TeV in Run 2 data (in red). Figure credits: ALICE Collaboration

diodes, strongly reducing the charge collection. The depletion volume around the n-well diodes is increased by applying a reverse bias voltage to the substrate. This technique allows an increase in the signal-to-noise ratio (S/N).

The layout of the ITS2 is shown in Fig. 3.6. The total surface area of the detector is $\sim$10 m^2 and it is covered by about 12.5 billion silicon pixels. The detector is grouped in

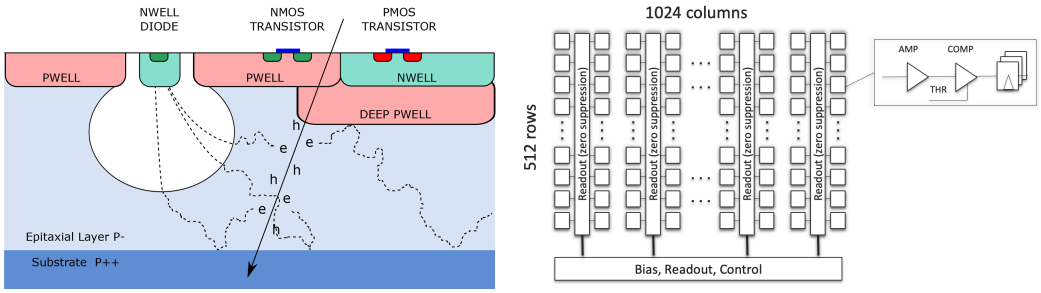

Figure 3.5: (Left) Schematic cross-section of a pixel cell. (Right) Architecture of the ALPIDE chip. Taken from Ref. [110].

two different sub-structures: the first one from the beam pipe is called the inner barrel (IB) and consists of the three innermost layers, while the outer barrel (OB) is arranged in two double layers, the middle and outer layer. The radial position of each layer was optimised to achieve the best performance in terms of pointing resolution, p_{T} resolution, and the best tracking efficiency in high multiplicity Pb–Pb collisions.

The ITS2 is divided into basic detector units, which are called staves. Staves consist of a polymide structure containing a printed circuit and the pixel chips, the *Hybrid Integrated Circuit* (HIC); a thermally conductive carbon fibre sheet with embedded cooling pipes, the *coldplate*; a support structure that provides the mechanical support and assembles HIC and Coldplate together, the *space frame*.

The ITS2 parameters are shown in the Tab. 3.2, while in Tab. 3.3 are shown the average radii of the layers, the stave lengths and the total number of chips.

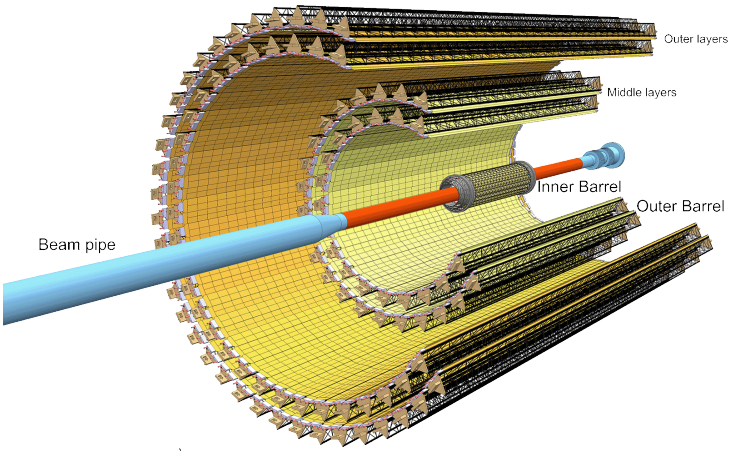

Figure 3.6: Layout of the ITS2 detector and the LHC beam pipe [114].

The mechanical structure of the ITS2 is shown in Fig. 3.7. The structural components of the barrels are designed to ensure accurate positioning within a few µm and to allow the separate assembly of all the layers inside the TPC. This is achieved with a complex support structure consisting of a conical structural service for IB, a conical and a cylindrical structure for OB and light composite end-rings. The structures are all contained inside a

Parameters	ITS2
No. of layers	7
Radial coverage	22–395 mm
Rapidity coverage	$\|\eta\| \leq 1.3$
Material budget	IB: 0.36% X_0, OB: 1.10% X_0
Pixel size	27 µm × 29 µm
Spatial resolution ($r\phi \times z$)	5 µm × 5 µm
Max rate (Pb–Pb)	50 kHz

Table 3.2: The main parameters of the ITS2 detector [114].

Layer	Average radius (mm)	Stave length (mm)	No. of staves	No. of chips
0	23	271	12	108
1	31	271	16	144
2	39	271	20	180
3	196	844	24	2688
4	245	844	30	3360
5	344	1478	42	8232
6	393	1478	48	9408

Table 3.3: Main layout parameters of the ITS2 layers [114].

support structure made of carbon fiber (the cage), installed within the inner radius of the TPC. The cage, which holds the beam pipe, is provided with a rail system designed to allow the installation of the ITS and MFT detectors within the inner radius of the TPC and to perform ordinary maintenance of the detectors during the yearly technical stops.

3.2.2 Time Projection Chamber

The TPC is the main tracker of the ALICE detector. It is a gas detector optimised to provide momentum measurements with excellent separation between tracks, to perform particle identification with the measurement of the energy loss per unity of length in the medium ($\mathrm{d}E/\mathrm{d}x$) and, together with the ITS subdetector, to determine the vertex of the collision. Similar to the ITS, the TPC underwent a major upgrade campaign during the LS2. The TPC covers a pseudorapidity range of $|\eta| \leq 0.9$ for the tracks that have been reconstructed in the full radial length (e.g. reconstructed using points in the ITS, TRD and TOF), and a full azimuth coverage. The TPC is able to reconstruct tracks in the range of transverse momentum range between $p_{\mathrm{T}} = 100$ MeV/c up to $p_{\mathrm{T}} = 100$ GeV/c.

The detector consists of a sliced segmented cylindrical barrel filled with a total volume of 88 m^3 of a $\mathrm{Ne}-\mathrm{CO_2}-\mathrm{N_2}$ gas mixture. The TPC is a cylindrical chamber, with the inner bore consisting of a central field cage drum with a 114 cm radius, which provides the necessary space for the installation of the ITS2. The layout of the upgraded TPC is shown in Fig. 3.8. The TPC volume is divided into two separate halves by the cathode; the two endplates are under positive voltage, and each endplate is subdivided into 18 azimuthal sectors. Each sector has one Inner Readout Chamber (IROC) and one Outer Readout Chamber (OROC). This configuration eventually brings the total amount of readout chamber to 159 pads in

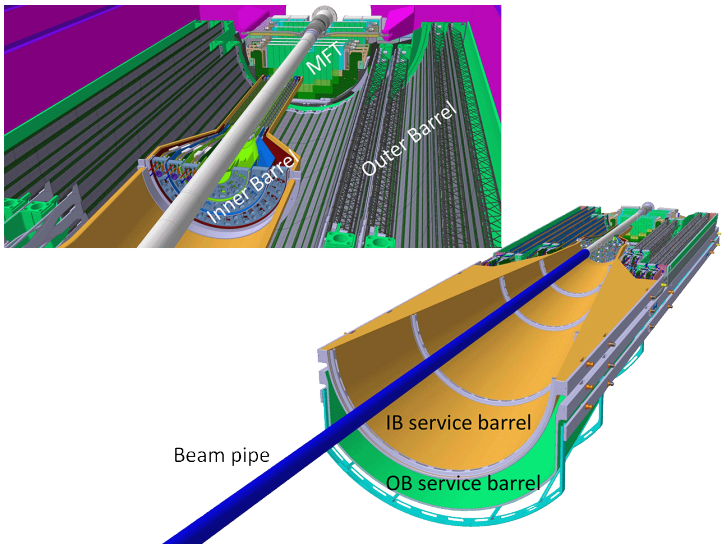

Figure 3.7: Overview of the mechanical structure of the ITS2 [110]. The upper panel shows the details of the Inner Barrel, the Outer Barrel staves, and the MFT in the back. The lower panel shows the conical structural shells.

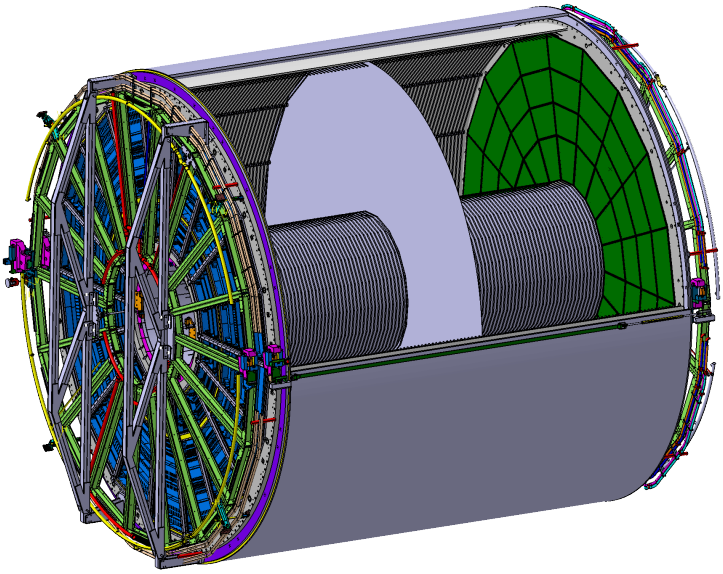

Figure 3.8: Layout of the TPC detector used in the LHC Run 3 [110].

the radial direction.

The TPC particle identification is based on the ionisation in the gas mixture caused by the charged particle crossing the barrel. When a charged particle crosses the gas volume, the particle can ionise the gas, separating electrons from positive ions. Applying a strong electrical potential (between the TPC cathodes and anodes) of -100 kV, the TPC generates a drift field of 400 V/cm. Due to the field, the positive and negative charges are separated

and drift in opposite directions inside the gas of the detector volume. The flow of charges inside the medium produces secondary ionisation, amplifying the signal extraction and creating an electron shower. The electrons are eventually collected by the positive electrode and measured by the endplates.

During Run 1 and Run 2, the readout system consisted of Multi-Wire Proportional Chambers (MWPCs) endplates. Due to the necessity of avoiding ion back-flow and reducing space charge effects in the drift region, the old TPC needed an active ion grid to collect the ions. A disadvantage of this design was that the previous TPC technology could sustain a limited readout rate (< 1 kHz). In Run 3, ALICE operates in continuous readout mode with no trigger. For this reason, a new readout system has been developed. The new IROCs and OROCs are based on the new Gaseous Electron Multipliers (GEMs) technology that allows up to 100 times higher rate with respect to Run 1 and 2, additionally reducing both the intrinsic dead time and ion back-flow. The layout of the ALICE TPC GEM panels [115] is shown in Fig. 3.9. The GEM chamber consists of a trapezoidal insulating polymide foil (with a thickness of 50 µm) coated with a copper surface (average Cu thickness $\sim$ 2–5 µm). The foils are perforated with a photo-lithographic processing performed by the CERN Micro-Pattern Technologies laboratory [116], forming a regular, dense pattern of double-conical holes (a few µm wide). The small dimensions of these amplification cones create powerful electric field strengths (around 50 kV/cm), sufficient for avalanche creation inside the holes of the GEM foil when a moderate voltage difference of typically 200 – 400 V is applied between the metal layers. This avalanche effect is shown in Fig. 3.9. Foils have two different hole pitch widths: standard (S, 140 µm) and large (LP, 280 µm). Foils are stacked to an S-LP-LP-S configuration, as shown in Fig. 3.10. Most of the ions are produced in the last amplification step. Every gap between the GEM foils is kept at a specific potential, and it produces transfer electric fields of 3500 V/cm in both GEM1-GEM2 (ET1) and GEM2-GEM3 (ET2) conjunction gaps; in GEM3-GEM4, the transfer electric field is around 100 V/cm (ET3), while the induced electric field between GEM4 and the pad plane is again 3500 V/cm.

The TPC readout chamber consists of a trapezoidal aluminium frame (the *Al-body*), a fiberglass plate (the *strongback*) and a pad plane made of a multilayer printed circuit board (the *PCB*). The IROCs are composed of one Al-body, one strongback, one pad plane and one GEM stack. The layout of an IROC is shown in Fig. 3.11. The OROCs, instead, are composed of one Al-body, one strongback, three pad planes and three GEM stacks.

The new readout system is expected to reduce the back-flow to 1%. After these upgrades, the new TPC energy loss resolution is around 5–10%, and the momentum resolution (obtained from the track length and bending in the solenoidal magnetic field) is around 1%. The TPC momentum resolution with the upgraded GEM readout is compatible with the one obtained with the previous MWPC setup. The comparison in Fig. 3.12 shows a compatible resolution in momentum for tracks with ITS-TPC information.

3.2.3 Time-Of-Flight

The ALICE Time-Of-Flight (TOF) detector is specifically designed to precisely measure the travel time of the particles from the vertex of the collision to the surface of the detector. The detector inner radius is approximately 3.7 m away from the beam pipe, and it is located all around the TRD, which envelopes the TPC.

Figure 3.9: Simulation of charge dynamics for two electrons entering into a GEM hole. The electron drift paths (the light lines) and the ion drift paths (the dark lines) are shown. The dots mark the places where ionisation processes have occurred. Shown in Ref. [110].

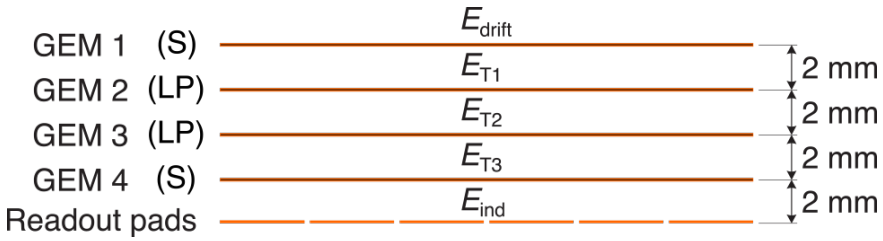

Figure 3.10: Schematic view of a stack with four GEM foils [110].

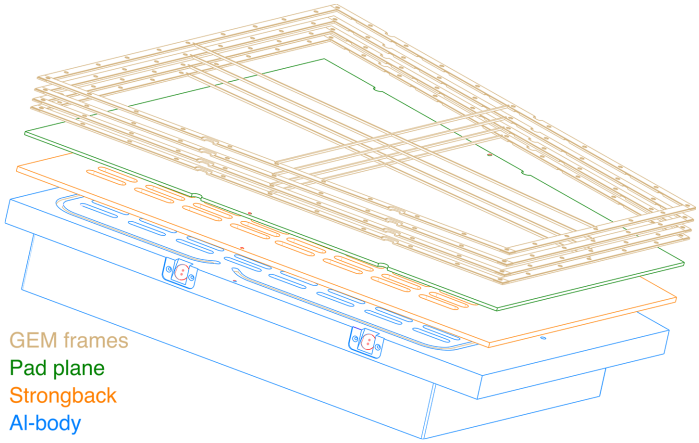

Figure 3.11: Layout of a TPC IROC, showing the chamber body components and GEM frames [110].

The TOF is a cylindrical detector covering the pseudorapidity range $|\eta| < 0.9$ and the full azimuth. The detector sensitive surface is a complex array of ~ 141 m^2 active

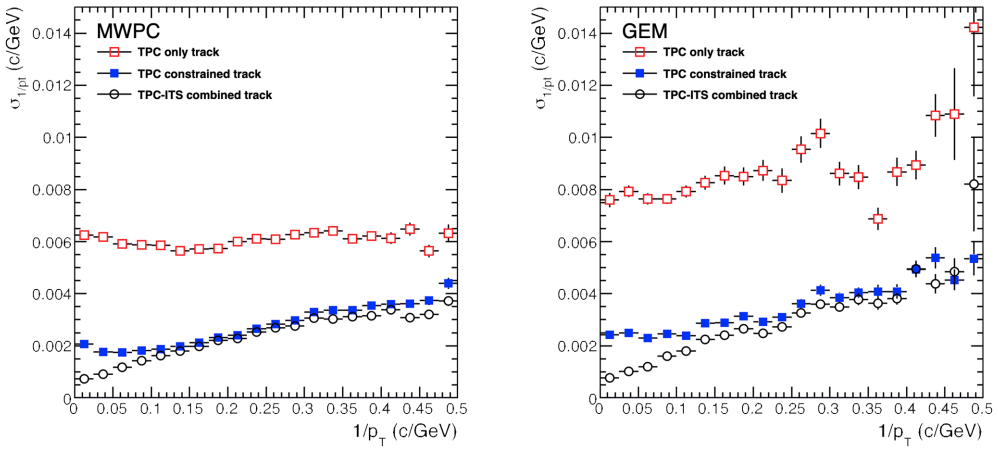

Figure 3.12: The ALICE TPC momentum resolution as a function of $1/p_{\mathrm{T}}$. The resolution is compared for the Run 2 MWPC (left panel) and the Run 3 GEM (right panel) readout systems [115].

area of Multi-gap Resistive Plate Chambers (MRPC). Each MRPC is subdivided into 96 readout pads with an active area of 2.5×3.5 cm^2. The TOF detector consists of a total of 1593 double-stack MPRCs. MRPCs are gaseous detectors consisting of two resistive plates kept at 13.5 kV voltage difference and filled with a $C_2H_2F_2$–SF_6 93–7 gas mixture. The larger gap is subdivided into smaller gaps by floating voltage resistive plates. If a charged particle crosses the gaps, it ionises the gas. Due to the strong electric drift field, the ionisation quickly produces an electron avalanche that can be measured by the readout. The schematic layout of a double-stack MRPC is shown in Fig. 3.13. The MRPC stack consists of 2 stacks grouping five 250 µm wide gaps each. Each stack is contained between a cathode and an anode printed circuit board (the PCB) containing the readout pads.

The stacks are delimited by two different types of glass. The outside glasses are covered with a special conductive paint, containing metal oxides that allow a high voltage to be applied at the extremities to induce a current. The outside glasses are 500 µm thick and connected to the PCB through high voltage connection holes and kept in position with a conductive glue. The inner glasses are 400 µm thick. The gap between the layers is maintained by using a fishing line. The anode PCB is a 1.6 mm thick and is three-layered, while the cathode PCB has a 0.8 thickness and is double-layered. The PCBs contain also the metallic pins used to pick up the signals from the pads and, together with a honeycomb panel frame, to provide the mechanical rigidity of the MRPC unit.

The MRPC modules are grouped into 18 azimuthal sectors, each sector containing a TOF supermodule containing 5 modules, as shown in Fig. 3.14. Each MRPC strip is placed to ensure that there are no dead zones.

The readout is performed through 152928 channels. The TOF readout system is composed of different units. Each of the 18 sectors is read by four VME crates. Every crate hosts one Data Readout Module board (DRM) and 9 or 10 TDC Readout Module (TRM)

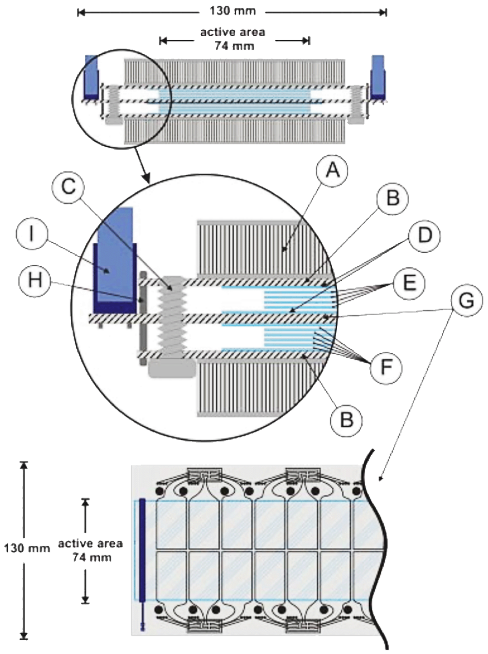

Figure 3.13: (Upper panel) Layout of a double-stack MRPC: (A) the honeycomb panel, (B) cathode PCBs, (C) nylon pin to stretch and regulate the fishing line, (D) 550 µm outer glasses, (E) 400 µm inner glasses, (F) 250 µm gaps, (G) anode PCBs, (H) the metal pin soldered to cathode and anode PCB, (I) the pin connector. (Lower panel) Layout of the readout pads [117].

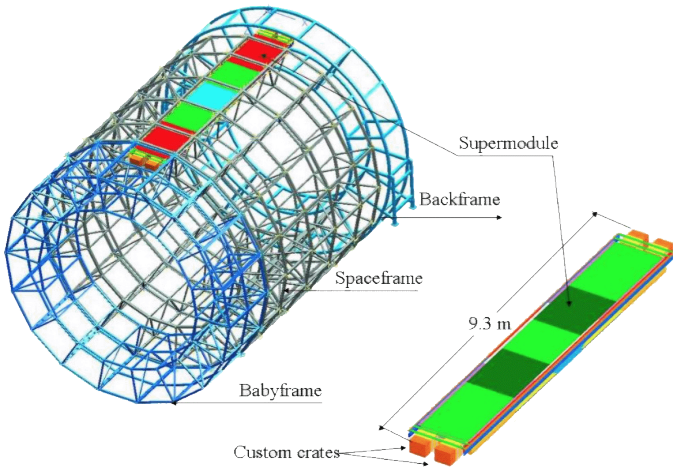

Figure 3.14: The layout of one of the TOF supermodules inside the ALICE spaceframe [110].

boards. In order to cope with the LHC Run 3 increased luminosity and interaction rate (see Section 3.2.5), the DRM has been upgraded during the LS2, switching the previous

boards with newly redesigned DRM (DRM2) [118], shown in Fig. 3.15. The DRM2 has been updated with a modern Field Programmable Gate Array (FPGA), the Microsemi IGLOO2, a fast programmable integrated circuit that replaces both the previous DRM Detector Data Link (DDL) and Timing, Trigger and Control systems (TTC) circuits. Both DRM2s and TRMs are hosted on 16 cm × 33 cm 9U VME cards. The DRM2 bandwidth to the Data Acquisition system (DAQ) is of 3.2 Gb/s, and it is designed to work in an ionising environment (with an expected total ionising dose for the boards of 0.013 krads per year). As introduced in Section 3.2.2, the ALICE apparatus operates in continuous readout mode during the Run 3 data taking, while during Run 1 and 2, the apparatus (and TOF) operated in triggered mode. To allow continuous mode, a synchronous trigger mode at fixed bunch crossing values at 33 kHz has been implemented in the readout: this feature sets a matching window of 30 µs in the GBTx ASIC TDC module of the TRM (the High-Performance Time-To-Digital Converter, HPTDC) to achieve a *effective* continuous readout. The DRM2 reads each TRM HPTDC channel as 64-bit words through a VME with a 160 MBytes/s peak throughput and eventually sends the data to the ALICE DAQ Common Readout Unit (CRU).

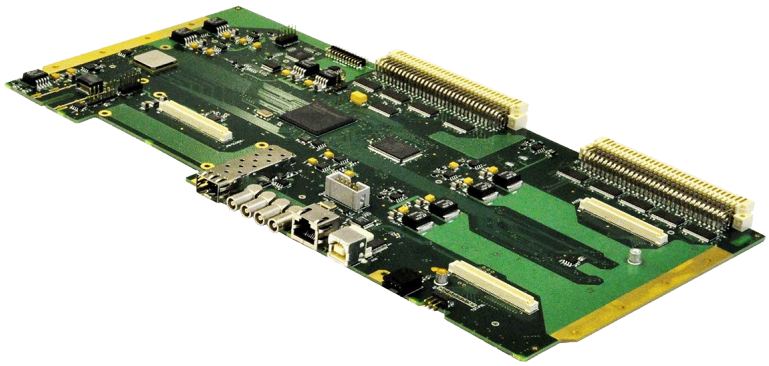

Figure 3.15: The TOF DRM2 board [118].

The TOF system is able to measure the time-of-flight of the particles with extreme precision. The global resolution of the TOF (σ_{TOF}) is due to different factors: the MRPC intrinsic time resolution ($\sigma_{\mathrm{MRPC}} = 50$ ps), the resolution on the collision time measured by the FT0 (σ_{t_0}), the resolution due to the readout electronics (σ_{electr}) and the resolution on the track momentum measured by the TPC (σ_p). The latter contribution can be parameterised as a function of the momentum. The global resolution is estimated summing in quadrature as

$$\sigma_{\mathrm{TOF}} = \sqrt{\sigma^2_{\mathrm{MRPC}} + \sigma^2_{t_0} + \sigma^2_p + \sigma^2_{\mathrm{electr}}}\,, \tag{3.1}$$

The global resolution measured during the calibration in pp collision at $\sqrt{s} = 13.6$ TeV is $\sigma_{\mathrm{TOF}} = 76$ ps, as shown in Fig. 3.16.

3.2.4 Fast Interaction Trigger

The Fast Interaction Trigger (FIT) [119] was designed to surpass the performance of the forward detectors used up to the Run 2 data taking campaign. The FIT is capable of

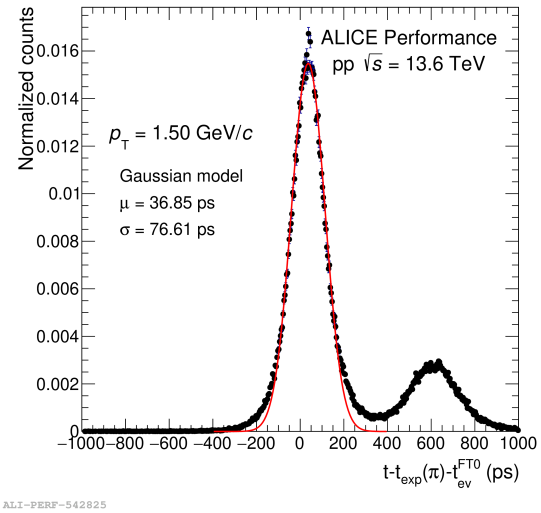

Figure 3.16: TOF resolution extracted under the mass hypothesis of π with the event time computed with FT0. Data collected in pp collisions at $\sqrt{s}$ = 13.6 TeV. Figure credits: ALICE Collaboration.

providing minimum bias (MB) trigger with an efficiency higher than 90% for pp collisions, measuring the luminosity for pp and Pb–Pb collisions with interaction rates up to 1 MHz and 50 kHz, respectively. The FIT allows the measurement of the collision time (that is needed for particle identification based on the time-of-flight) with a resolution better than 50 ps, and it is used to estimate the event multiplicity, centrality, and measure the event plane [120]. To satisfy the requirement of large acceptance and precise timing capability, FIT have a hybrid technology design, consisting of three subdetectors positioned in high-rapidity regions: the *FT0*, the *FDD* (both based on two arms of arrays of Cherenkov radiators) and the *FV0* (that uses a large segmented scintillator ring). The layout of the FIT detector inside the ALICE apparatus is shown in Fig. 3.17 (with respect to the longitudinal direction) and in Fig. 3.18 (on the transverse plane). In the latter, the distances of the FIT subdetectors from the nominal IP and the rapidity coverage are indicated.

The FT0 is formed by two Cherenkov arrays on both sides of the IP, named T0A and T0C, which have 24 and 28 modules, respectively. Each module is formed by a 2 cm thick quartz radiator coupled to a 53 x 53 mm^2 wide Planacon XP85012 micro-channel plate photo-multiplier (MCP-PMT) The FT0 Cherenkov modules were designed to be fast, and the subdetector design makes them insensitive to the background noise induced by particles coming from directions different from the IP. For this reason, the FT0 is fundamental in the minimum-bias and centrality trigger generation, along with collision time and vertex position estimation. In the left panel of Fig. 3.19, the correlation between collision vertex reconstructed by the tracking detectors and FT0 pp collision at $\sqrt{s}$ = 13.6 TeV is shown, while on the right panel of the same figure, the FT0 time resolution is shown for the same dataset.

The FV0 is a scintillator ring divided into five rings and eight 45-degree sectors, forming 40 detection elements assembled in a disc with an outer diameter of 148 cm and an inner

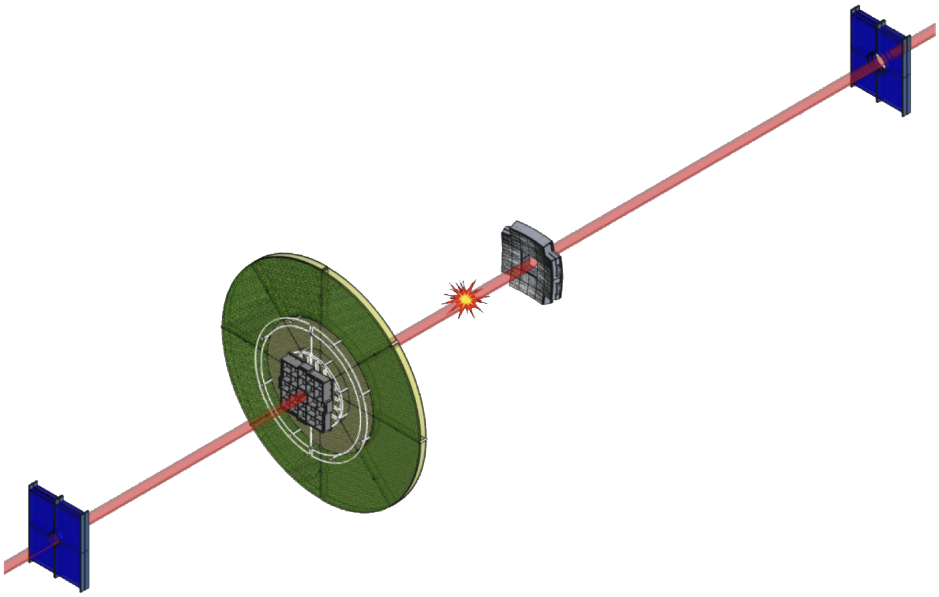

Figure 3.17: Layout of the FIT subdetectors (FT0, FV0 and FDD) aligned along the beamline. From bottom-left: FDD-A, FT0-A connected with FV0, IP, FT0-C, FDD-C. Not in scale [119].

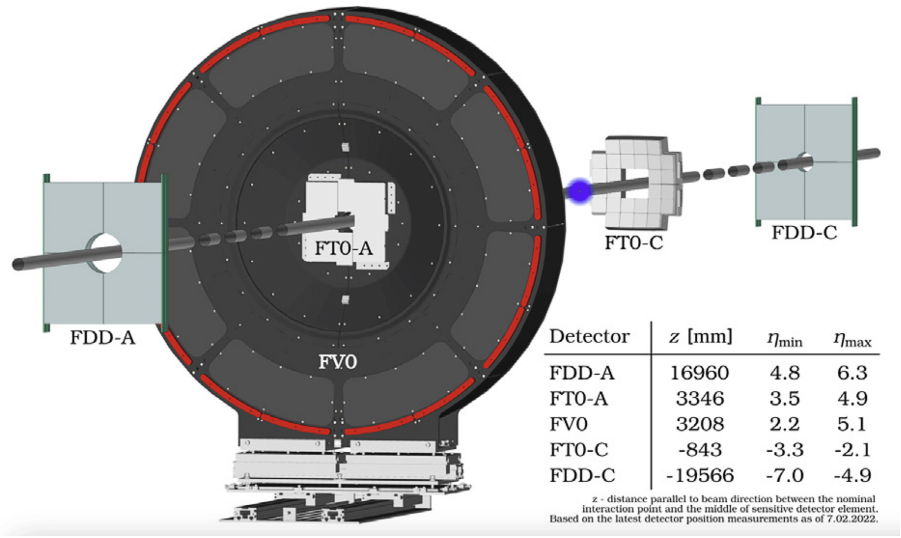

Figure 3.18: Layout of the complete set of FIT subdetectors arranged side-by-side (seen in the transverse plane). For each subdetector, the distance from the nominal IP (z) and the rapidity (η) coverage is indicated in the inset table. Taken from [121].

diameter of 8 cm. It is located on the beam longitudinal direction, on the opposite side of the hadron absorber of the Muon Spectrometer. The subdetector active surface is made of

4 cm thick EJ-204 plastic scintillators, each paired to a grid of optical fibers transmitting the signal to Hamamatsu R5924-70 fine-mesh PMTs, designed to work in high magnetic field condition [122]. Each sector of the outermost ring is read out by two photosensors for a total of 48 readout channels. The FV0 is suitable for monitoring the background, improving minimum-bias trigger efficiency and allowing the extension of the resolution available for the centrality-based trigger. The FT0-FV0 pair is essential for the centrality and event plane determination.

The FDD is formed by two-sided scintillator arrays (compared to a single layer used by the FV0) that use a fast state-of-the-art wavelength shifter. With respect to the FT0, the FDD arrays are located further from the IP (17 and 19.5 m), and because of cable-induced latency, they are mostly used as offline detectors. Nevertheless, it is essential for tagging photon-induced or diffractive events (as it substitutes the previous AD detector used during the Run 2 [123, 124]) - monitoring the absence of activity in the forward direction -, expanding the pseudorapidity coverage of the ALICE apparatus. This is crucial to better understand both the diffraction and the initial state of protons and ions in collisions as a function of energy with the new Run 3 collision energies.

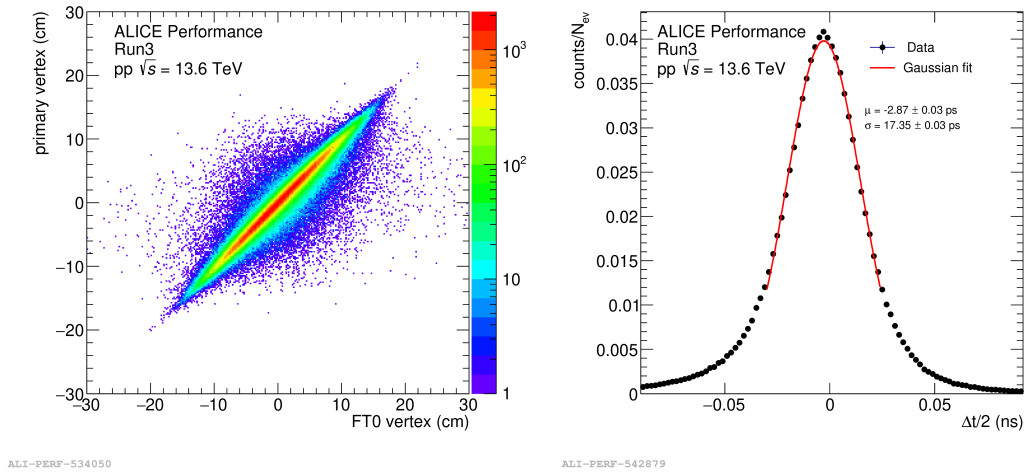

Figure 3.19: Performance of the FT0 subdetector on pp collision at $\sqrt{s} = 13.6$ TeV. (Left panel) Correlation between collision vertex reconstructed by the tracking detectors and FT0. (Right panel) The FT0 time resolution reached $\sim$ 17 ps, while with the first pp at $\sqrt{s} = 900$ GeV collisions this value was $\sim$ 26 ps [121].

The FIT uses dedicated front-end electronics common for all FIT subdetectors and is designed to collect data in a continuous readout mode. The front-end electronics are made with two types of VME boards. The Processing Module (PM) acquires the time signals and integrates the charge in a 16-21 ns window, using two fast 12-bit Analogue-to-digital converter circuits (ADCs). The TCMs use the pre-trigger information of PMs to create final triggers to be sent to the Central Trigger Processor of the ALICE Data Acquisition (see next Section).

3.2.5 ALICE integrated luminosity in the LHC Run 3

The upgrades on the ALICE detector discussed in the previous sections could, in principle, allow the experiment to be operated at an interaction rate of up to 4 MHz [125]. To limit the pile-up of collisions within the ITS readout time, it was chosen a suitable working interaction rate of 0.5 – 1 MHz for pp collisions and 50 kHz in Pb–Pb collisions. This choice allows limiting the pile-up to a small number (2-5 collisions) that can still be separated using the track association to reconstruct primary vertices. As during the LHC Run 3 the target integrated luminosity of ALICE (200 pb^{-1} in pp collisions) requires the apparatus to take data with interaction rates that are larger by a factor 5–20 with respect to the Run 2, an enormous amount of data is expected to be collected by the detector in continuous readout mode. In Fig. 3.20 the integrated luminosity collected by the ALICE experiment since the beginning of the Run 3 is shown until September 2024.

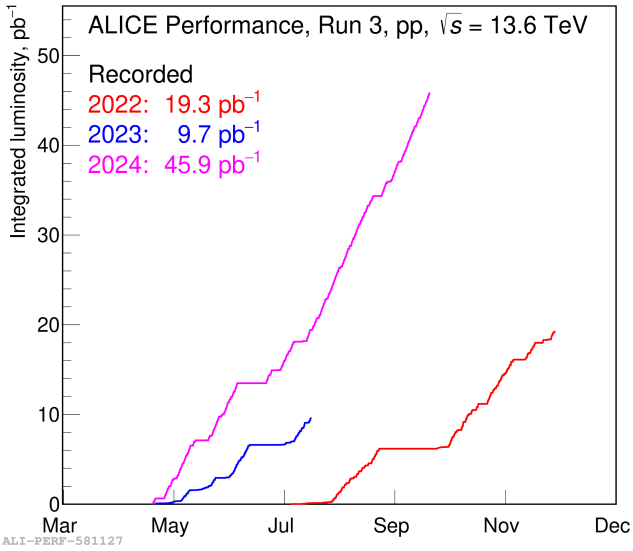

Figure 3.20: Total integrated luminosity for pp data taken in 2024 (as of September 2024) compared with 2022 and 2023 data taking periods. Figure credits: ALICE Collaboration.

3.2.6 O^2: the ALICE Online-Offline framework

The enormous amount of data expected to be collected by the detector (up to 1 TB/s in Pb–Pb collisions) requires a major update on the computational power of the data acquisition system. Additionally, measurements proposed for Run 3 have a low signal-to-background ratio, making the previous triggering techniques ineffective because of the high background levels. Therefore, a triggerless acquisition method and large samples would be necessary. To achieve this purpose, the need to minimise costs and maximise the efficiency of the data reduction and compression made it necessary to upgrade the Online-Offline (O^2) computing facility [126]. The O^2 farm is located at the experimental area at Point 2. The system is designed to work both online (synchronously, to store the data during the

data taking) and offline (asynchronously, to reconstruct the data according to later offline calibrations).

The online processing of the signals collected during the collisions is firstly performed by First Level Processors (FLPs), a farm of powerful computers connected to the ALICE detectors CRUs through 250 computing nodes, each one equipped with 32-core CPUs and 8 GPUs. Additionally, FLPs can run in replay mode by *replaying* the previously acquired data and run Monte Carlo simulations in real-time for testing the facility performance when the LHC collisions are interrupted for any reason. The data flow from CRUs is divided into specific Time Frames (TFs), which are sent and multiplexed to the FLPs I/O system via optical readout links. The raw data contained in each TF is immediately compressed by a factor of 2.5, then reprocessed and repacked, splitting the data into sub-Time Frames. The content of these TF undergoes a preliminary clustering, calibration and masking process, before being buffered in the memory and sent to the Event Processing Nodes (EPNs). EPNs consist of 1500 computing nodes, each one equipped with 32-core CPUs and 8 GPUs. EPN handles Time Frame aggregation and performs event and track reconstruction for each detector using a preliminary set of calibrations. The data volume is fully compressed by an additional factor of 8, resulting in a 90 GB/s throughput to data storage (60 MB/s per EPN). After the synchronous stage, the reconstructed data are saved in the Compressed Time Frame (CTF). CTF holds processed data from all the detectors and temporarily stores them in preparation for the asynchronous reconstruction.

Calibration and track matching are eventually completed asynchronously, reaching the desired data quality. This is achieved after an intense Asynchronous Quality Control campaign (Asynch-QC). The data are then permanently stored locally using the highest-quality global calibration performed in the Asynch-QC (the asynchronous pass, or apass). To perform the analysis, a second type of reconstructed data is produced, the Analysis Object Data (AOD). This contains all the key information about the reconstructed event, such as the primary and secondary vertex reconstruction, the track characteristics, the kinematic parameters, as well as the clusters and signal amplitudes from the ALICE detectors.

The produced AODs are permanently stored on hard drives in the O^2 facility or Tier 0/1 data centres and are accessible on the ALICE Grid. Tiers 0 and 1 participate in the asynchronous reconstruction process, where data undergo systematic re-calibration, reprocessing, and re-filtering. Additionally, tiers can produce Monte Carlo data, simulating the detector responses. The final AODs are eventually sent to the analysis facility to execute the data analysis. The asynchronous processing of data from a data taking period (including calibration and reconstruction) must be finalised before a new data-taking period begins. The storage facility acts as an *interface* between the O^2 facility and the ALICE Grid. All CTF data are cleared from the O^2 farm and Tier 1 disk buffers to free up space for new data. Any unprocessed data is stored on tape until the next LS phase when it can be reprocessed. In Fig. 3.21, the complete data flow and processing pipeline of the ALICE O^2 system is schematically represented.

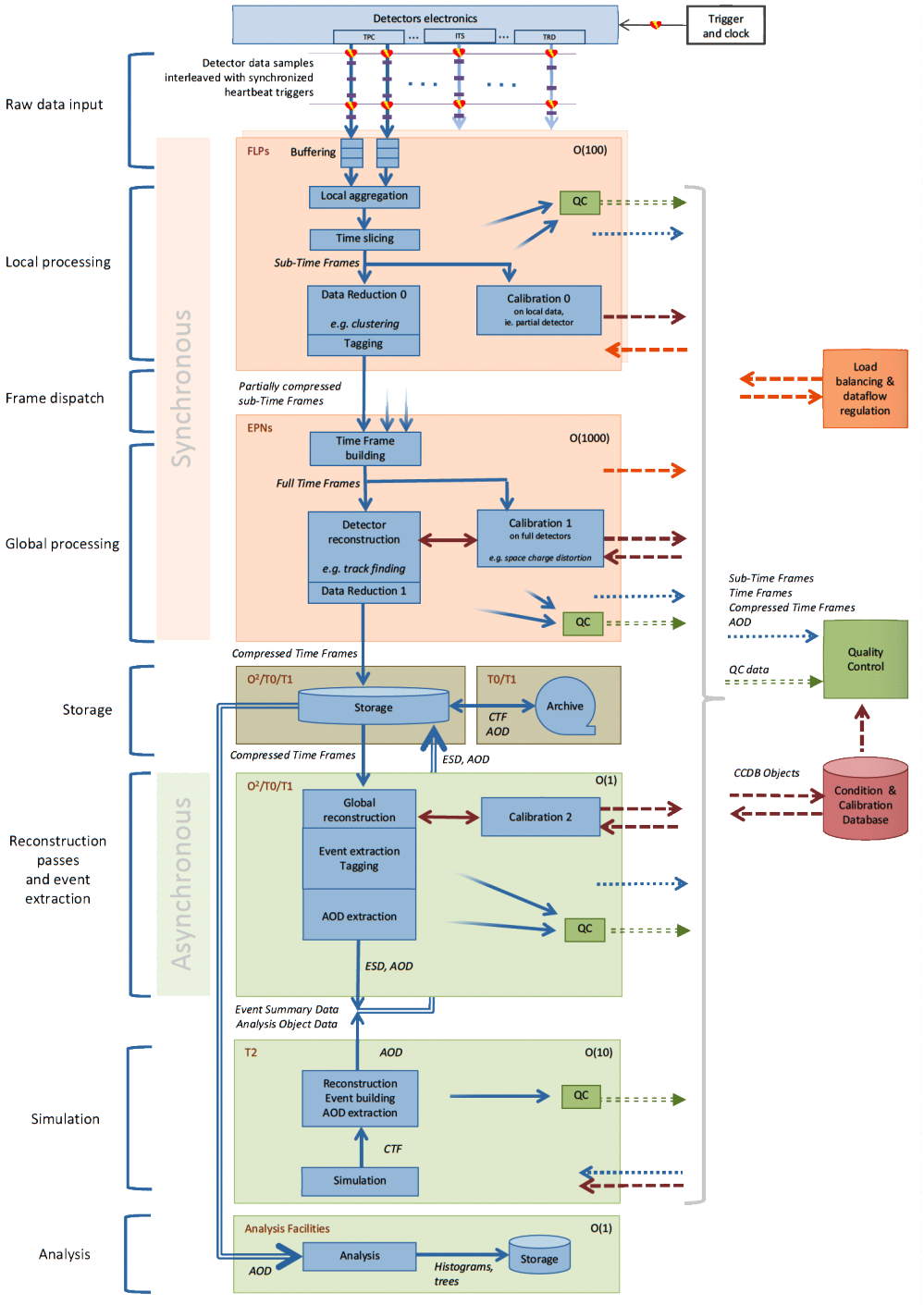

Figure 5.1: Data flow and processing pipeline of the O^2 system.

Figure 3.21: Data flow and processing pipeline of the O^2 system [126].

Chapter 4

Identification of light nuclei in ALICE

The ALICE apparatus can perform precise measurements of light nuclei such as deuteron, helium and their antimatter counterparts by taking advantage of the technologies described in Chapter 3. This chapter focuses on the hadron identification techniques that have been employed for the analysis presented in this work, which exploit the information of the TPC and the TOF detectors. ALICE is able to identify hadrons as well as light (anti)nuclei in different collision systems and in a broad range of transverse momentum (from $p_{\mathrm{T}} = 0.7$ MeV/c to 5-6 GeV/c for deuteron) with four different sub-detectors: TPC, TRD, TOF and HMPID. The TPC identifies particles through measurements of their specific loss of energy in the detector gas, the TRD exploits the measurement of the transition radiation, the TOF provides the measurement of the particle time-of-flight that, combined with the momentum and track length information can be used to compute the particle's mass, and the HMPID provides the measurement of the relativistic β obtained from the Cherenkov radiation emission angle. The HMPID was used in Run 1 to extend the momentum range for the measurement of deuteron production in Pb–Pb collisions [95], despite a limited acceptance compared to the TPC and the TOF, whereas the TRD was used during the LHC Run 2 to trigger on collisions in which a light nucleus was produced [127]. The p_{T} range for the optimal ALICE hadron PID performance is shown in Fig. 4.1. For this work, the identification of light (anti)nuclei is performed using the TPC and the TOF detectors. Therefore, the next sections will focus on these systems.

Most ALICE analyses that require hadron identification start first by applying track-quality selection criteria to remove from the sample the tracks that have been reconstructed with poor quality, for instance, tracks that have been obtained from a small number of TPC space points (*clusters*). At this stage, also kinematics selections (minimum p_{T}, rapidity range) are applied. Details on these criteria relevant to the analysis presented in this thesis will be given in Section 5.1.

Particle identification is performed on the resulting sample of good quality tracks to select particles with target properties while minimising the wrong species association.

It is worth mentioning here that while a fraction of the selected charged particles are produced by the hadronisation processes following the collisions and are emitted from

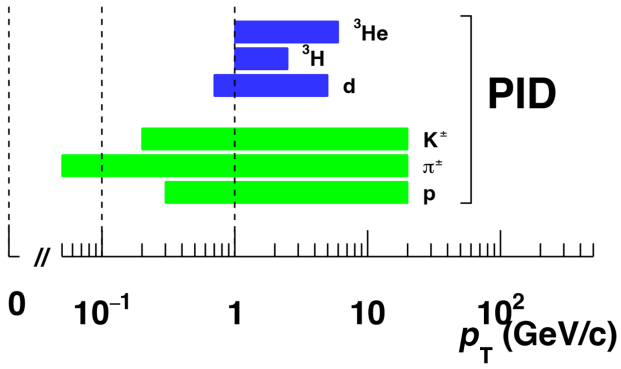

Figure 4.1: ALICE particle identification and reconstruction capabilities, with the p_{T} coverage corresponding to the published measurements based on pp or Pb–Pb data samples. Adapted from [75].

the interaction point (i.e. from the primary vertex of the collision, hence the name of *primary* particles), some of them are produced afterwards through secondary processes (*secondary* particles). Weakly-decaying primary particles travel through the detector for a few tens of centimetres distance and then decay (*secondary from weak decay*), while other particles can be produced by knock-out when primary particles hit the nuclei of the material of the ALICE detectors or structure frame (*secondaries from material*). To separate primaries from secondaries, the Distance of Closest Approach (DCA) information is used. The DCA is the distance between the particle track and the primary vertex. The distance can be projected in two components: the DCA_{xy} is the projection of the DCA on the plane transverse with respect to the beam direction and the DCA_z is the longitudinal component. Primary particle tracks are characterised by small values of DCA, peaked around zero, as they are emitted from the vertex of the collision, while secondary particles are expected to show a broader DCA distribution. This feature can be used to estimate the fraction of primary particles in the data and to correct the measured yields accordingly (see Section 5.3.3).

4.1 TPC PID

The signal output of the TPC readout chambers is used to perform particle identification based on the measured loss of energy in the TPC gas (see Section 3.2.2), given by the Bethe-Bloch formula:

$$-\left\langle \frac{\mathrm{d}E}{\mathrm{d}x} \right\rangle = Kz^2 \frac{Z}{A} \frac{1}{\beta^2} \left[\frac{1}{2} \ln \frac{2m_e c^2 \beta^2 \gamma^2 T_{\max}}{I^2} - \beta^2 - \frac{\delta(\beta\gamma)}{2} \right] . \tag{4.1}$$

The formula parameterises the rate of energy loss per unit path length ($\mathrm{d}E/\mathrm{d}x$) based on the charge of the incident particle (z), the atomic number (Z) and atomic mass (A) of the material, the velocity of the incident particle ($\beta = \frac{v}{c}$), the Lorentz factor of the incident particle ($\gamma = (1-\beta^2)^{-\frac{1}{2}}$), the mean excitation energy of the material (I), the maximum kinetic energy that can be transferred to the electrons of the material (T_{max})

and the density effect correction which takes account of induced material polarisation by the incident particle ($\delta(\beta\gamma)$). The rest mass of the electron is m_e, whereas c is the speed of light in vacuum. The energy loss of different particles depends on their charge and mass. Two ionising particles with different charges and with the same velocity can be separated as the higher the charge of the particle, the higher the energy loss. This characteristic is used to separate the lighter particles with $z = 1$ (electrons, muons, pions, kaons and hydrogen ions like protons, deuterons and tritons) from helium nuclei with $z = 2$ (helium-3 and alpha particles). It is worth stressing that this is fundamental to separate nuclei with the same number of nucleons (and nearly identical mass), like tritons (one proton and two neutrons) and helium-3 (two protons and one neutron). At the same time, two particles with the same momentum and different mass will have different velocities due to the inertia: slower particles will also lose more energy per length of material crossed, and this effect will allow the separation of different species. The performance of the TPC detector in pp collisions at $\sqrt{s} = 13.6$ TeV in terms of measured specific energy loss as a function of the particle rigidity is shown in Fig. 4.2. The bands that stand out correspond to different particle and antiparticle species, to which a parametrised Bethe-Bloch curve is superimposed. It can be noted that the bands for deuterons, tritons and helium nuclei are more populated than the corresponding antimatter nuclei (negative charge): a significant fraction of matter nuclei are secondary particles produced from knock out of the detector material, whereas no antinuclei can be produced in such processes.

The particle identification via energy loss can be used up to a rigidity of $p_{\mathrm{T}}/|z| \sim$ 2-3 GeV/c. When a high-momentum particle has a kinetic energy of around two times its rest mass, the particle undergoes the minimum ionisation losses in the medium, which is called a Minimum Ionizing Particle (MIP). MIPs have a constant loss of energy in the medium (Fermi's plateau) and their energy loss at high rigidity is independent of their mass and charges. For this reason, high-momentum particle identification in ALICE is usually performed by other subdetectors such as TOF or HMPID or using different subdetectors together with the TPC. For example, the TPC detector can be used to perform a loose preselection of candidates at intermediate rigidity (the 2-6 GeV/c range) combined with the PID by the Time-Of-Flight detector, as described in Section 4.2. The TPC can be used at high momenta ($p_{\mathrm{T}} > 7$ GeV/c) using a statistical based approach which uses estimations of the expected fractions of the species.

The loss of energy described by the Bethe-Bloch equation (Eq. 4.1) can be opportunely parameterised [128] to fit the TPC response:

$$f(\beta\gamma) = \frac{P_1}{\beta^{P_4}}\left[P_2 - \beta^{P_4} - \ln\left(P_3 + \frac{1}{(\beta\gamma)^{P_5}}\right)\right], \tag{4.2}$$

where β e γ are the relativistic factors and $P_1, \ldots, P_5$ are free parameters. This parameterisation has been developed by the ALEPH collaboration for the LEP collider, and hence the name ALEPH Bethe-Bloch. Another common parameterisation is based on the low-momentum particles ($p \leq 1$ GeV/c) having a specific energy loss that depends on $1/\beta^2$. In that case, the PID is performed by applying a fiducial selection on the expected value of the signal (splines parameterisation). The width of this selected fiducial interval is expressed in multiples of the $\mathrm{d}E/\mathrm{d}x$ resolution σ. The expected TPC response for the different species can be manually calibrated according to the data. The details about this procedure are addressed in Section 4.1.1.

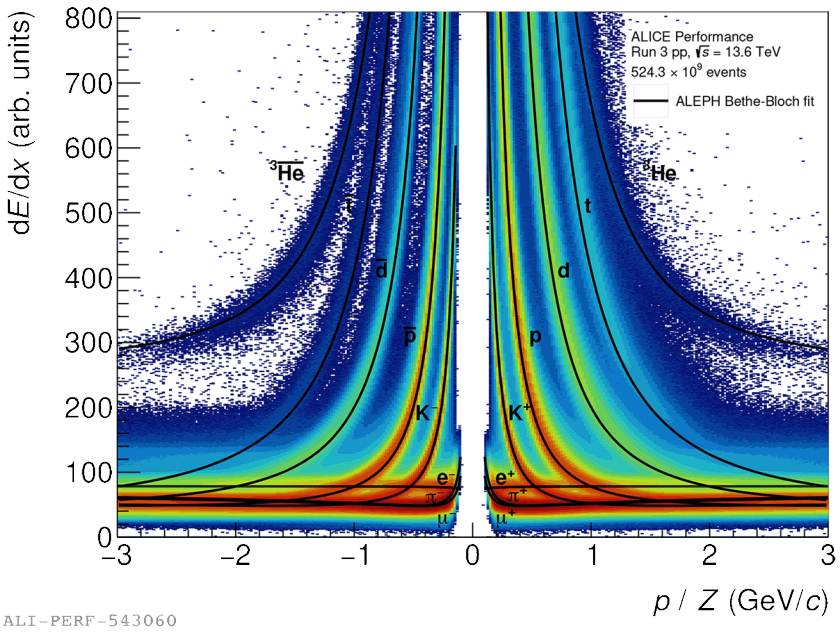

Figure 4.2: Particle energy loss as a function of the rigidity p/z measured by the ALICE TPC in the 2022 data taking campaign of pp collisions at $\sqrt{s} = 13.6$ TeV. The solid black curves represent the ALEPH parameterisation (see text for details) of the specific energy loss for different particle and antiparticle species. Figure credits: ALICE Collaboration.

The signal extraction in the TPC is based on the difference between the measured specific energy loss $(dE/dx)_{meas}$ of the particles in the gas and the expected specific energy loss $\langle dE/dx \rangle_{exp,i}$ for a selected particle species. The latter is estimated using the Bethe-Bloch equation, Eq. 4.1. The so called PID $n\sigma$ *estimator* for a species i is expressed as the ratio $\mathrm{N}_{\sigma,i}^{\mathrm{TPC}}$ of this difference to the energy loss resolution for the selected species, σ_i^{TPC},

$$\mathrm{N}_{\sigma,i}^{\mathrm{TPC}} = \frac{(dE/dx)_{meas} - \langle dE/dx \rangle_{exp,i}}{\sigma_i^{\mathrm{TPC}}} \,. \tag{4.3}$$

The typical TPC PID response in terms of $\mathrm{N}_{\sigma}^{\mathrm{TPC}}$ is reported in Fig. 4.3 and Fig. 4.4 for the π and p hypotheses, respectively. The distribution of $\mathrm{N}_{\sigma}^{\mathrm{TPC}}$ versus $p_{\mathrm{T}}/|z|$ is monitored to assess the success of the PID response calibration in the process of asynchronous quality control (Asynch-QC) of ALICE. In the operational momentum range of the TPC, the distribution of the $\mathrm{N}_{\sigma}^{\mathrm{TPC}}$ of a selected species is expected to be centered around 0 and have a width of one, by the definition of $\mathrm{N}_{\sigma}^{\mathrm{TPC}}$. The data in Fig. 4.3 and Fig. 4.4 show a well-calibrated response, which presents the mentioned features. As a counter example, in Fig. 4.5, instead, a problematic TPC response for protons is shown, obtained from the Asynch-QC algorithm that checks whether the response is well calibrated (near to ideal) or not. Different curves correspond to different data samples (or *runs*) and the figure shows how the responses can be misaligned, suggesting the need for improvement before data can be used for physics analysis. In day-by-day operations, these checks are fundamental to

the ALICE experts to establish whether another calibration step and new reconstruction using a better detector response is necessary.

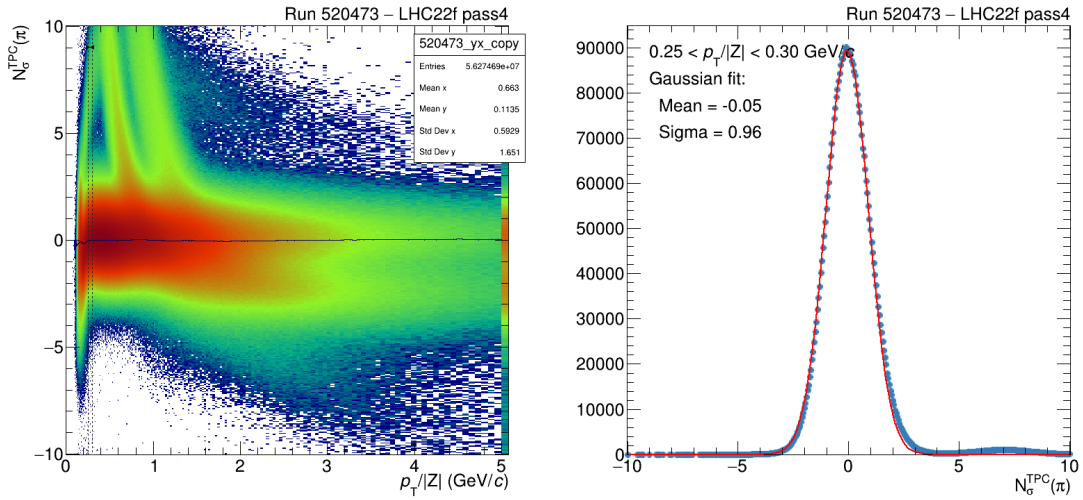

Figure 4.3: TPC response for the π hypothesis. On the left, the N_σ^{TPC} distribution is plotted as a function of $p_T/|z|$, while on the right the response is integrated in the $p_T/|z|$ = (0.35 – 0.45) GeV/c range.

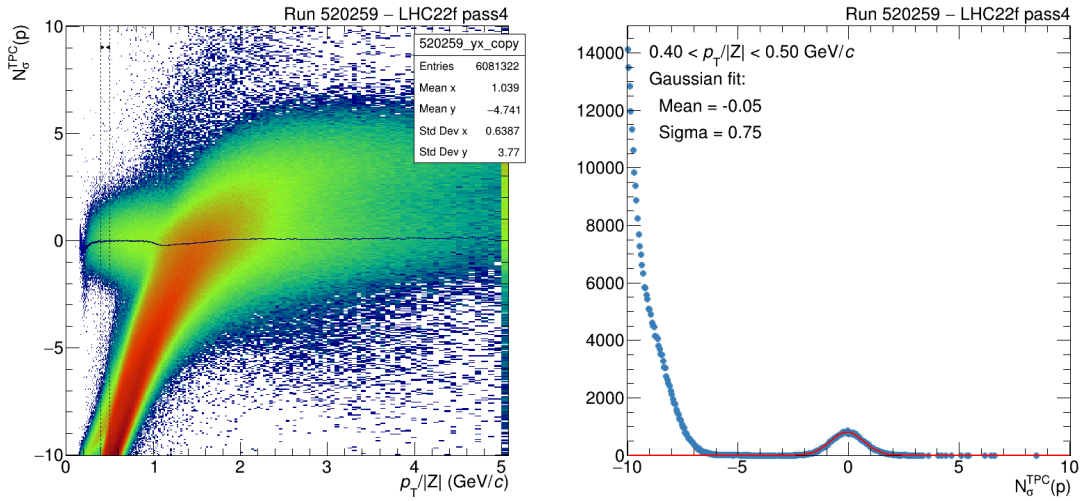

Figure 4.4: TPC response for the p hypothesis. On the left, the N_σ^{TPC} distribution is plotted as a function of $p_T/|z|$, while (on the right) the response is integrated in the $p_T/|z|$ = (0.40 - 0.50) GeV/c range. In this case, the σ value is smaller then expected.

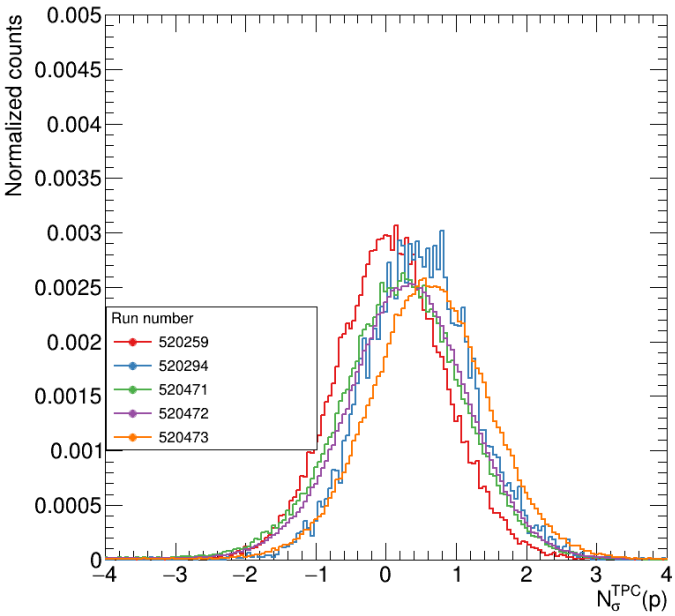

Figure 4.5: TPC response for the p hypothesis for different runs as obtained from data quality control algorithms. Not all the data samples have a N_σ^{TPC} mean value equal to zero, which suggests a recalibration of the detector response is needed before data can be used for physics analysis.

4.1.1 TPC response calibration procedure

When analysing the 2022 ALICE pp collision data at $\sqrt{s} = 13.6$ TeV targeting the measurement of ^{3}He and $^3\overline{\text{He}}$, a custom TPC response calibration procedure was deemed necessary as the central TPC response provided in the ALICE O^2 framework does not accurately predict the specific energy loss of particles whose charge is $Z > 1$.

The calibration procedure consists of fitting the measured energy loss distribution measured by the TPC with an ALEPH parameterisation (Eq. 4.2). After the fit is performed, the resolution of the TPC for the selected species is estimated directly from the data. The resolution is defined as the difference between the measured $\mathrm{d}E/\mathrm{d}x$ value and expected value. An histogram is filled with all the resolution values measured in a set $\mathrm{d}E/\mathrm{d}x$ range in the $p_\mathrm{T} = (0.5 - 3.5)$ GeV/c range. The distribution of resolutions is then fitted with a gaussian function and the width σ_{res} is used as an input in Eq. 4.3 to recalibrate the N_σ^{TPC} vs p response for the tracks. These values are used as the nominal energy loss for a chosen species, according to the method described in Section 4.1.

Once the custom parameters are extracted from the fit, these are used by an algorithm based on Eq. 4.2 to recalculate the $N_{\sigma,i}^{TPC}$ values of the tracks when the analysis is performed, allowing to perform the TPC PID correctly. This is performed by a separate piece of software (a *task*) that accounts for the $N_{\sigma,i}^{TPC}$ recalculation in parallel to the analysis

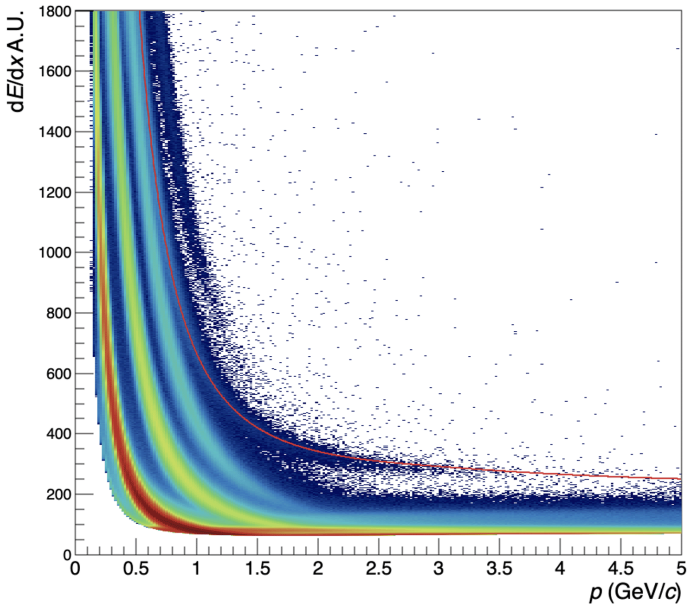

Figure 4.6: TPC response for negative particles in 13.6 TeV pp data. On the distribution, the custom Bethe-Bloch parameterisation for $^3\overline{\mathrm{He}}$ is superimposed to the data as a red curve.

software. The calibration parameters were first determined on a sample of 3.3×10^{11} collision events, representing the 71% of the whole 2022 dataset employed for the analysis. In Fig. 4.6, the result of the custom Bethe-Bloch calibration for anti-helium on the TPC signal distribution is shown in red.

The same procedure has been performed on the simulation datasets, with different calibrations, as the TPC response is different between data and MC. As the MC are used to estimate the $A \times \epsilon$ corrections of the raw spectra, the TPC must be consistent also in the simulated data. Hence, a custom calibration has been performed and, by extension, procedure has been applied to all the datasets used in this analysis.

In Fig. 4.7, the effects of the custom calibration on a dataset with a non-ideal central calibration are shown. The central TPC response (on the left panel) for deuterons in pp collisions at $\sqrt{s} = 900$ GeV causes the $\mathrm{N}_{\sigma}^{\mathrm{TPC}}$ (d) distribution to differ significantly from zero ($\mu = -1.889$). After the calibration procedure (on the right panel), the $\mathrm{N}_{\sigma}^{\mathrm{TPC}}$ for same dataset has a mean value close to zero ($\mu = 0.1128$) and a width close to unity.

4.1.2 Light (anti)nuclei identification with the TPC

Once that the TPC response is calibrated, the TPC information is used in analysis as described in the following for the case of antideuteron, chosen as an example. The candidate particles of interest, here $\overline{\mathrm{d}}$, are selected performing the selection in $\mathrm{N}_{\sigma}^{\mathrm{TPC}}$ vs p_{T} distributions. For every bin of p_{T}, the signal is extracted fitting the $\mathrm{N}_{\sigma}^{\mathrm{TPC}}$ distribution with a function. In Fig. 4.8 (on the left) is shown the distribution of $\mathrm{N}_{\sigma,i}^{\mathrm{TPC}}$ (d) as a function of rigidity. For $p_{\mathrm{T}} = (0.3 - 1.5)$ GeV/c, the TPC response signal due to the deuteron (the

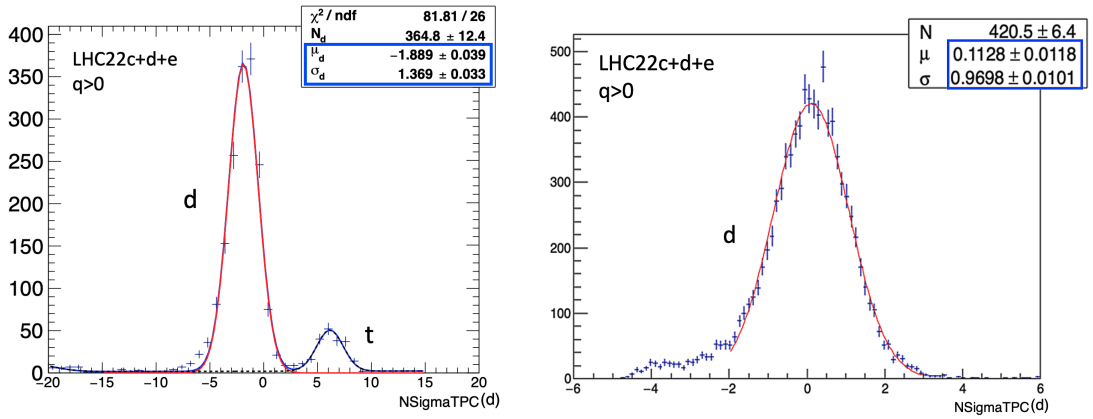

Figure 4.7: The N_σ^{TPC} distribution for deuterons before the calibration (left panel) and after the custom calibration (right panel) are compared. The N_σ^{TPC} distributions for the deuteron are fit with a Gaussian function. μ and σ are respectively the mean value and the width of the function. The triton signal is not visible on the right panel because of the different N_σ^{TPC} range of the plot.

band centred around 0) is visible. The proton signal (the red band on the bottom left) at low p_T shows a not flat ideal response. This will be addressed in the p_T-shift discussion (see Section 5.3.1). At higher p_T values, the proton signal overlaps the deuteron signal and the separation between species is less clear.

The function used to extract the signal is generally defined as the sum of two components, one that would fit the N_σ^{TPC} distribution in an ideal case with no contamination due to track mismatching or wrong species identification (the *signal*), and one that accounts for other particle contamination or detector effects (the *background*). The integral of the signal function in a $n\sigma$ range, with n being an appropriate value, returns the uncorrected (or *raw*) yield of the particle. Details on the TPC fit function used for the analyses of ^{3}He and $^3\overline{\text{He}}$ are given in Chapter 5.

4.2 TOF PID

The TOF detector can perform PID via time-of-flight measurements. A first PID method is based on the TOF reconstructed mass of a particle. The particle velocity $\beta = v/c$ and the Lorentz factor γ can be estimated from the measured time-of-flight t_{TOF}, once the track lenght L is known, as

$$\beta = \frac{L}{ct_{\text{TOF}}}, \qquad \gamma = \frac{1}{\sqrt{1-\beta^2}}\,. \tag{4.4}$$

Particles with different masses and with the same momentum have different velocities β. In Fig. 4.9, the velocity β of the species as a function of p in pp collisions at $\sqrt{s} = 13.6$ TeV is shown, where bands for π, K, p and d can be distinguished. The mass of a particle

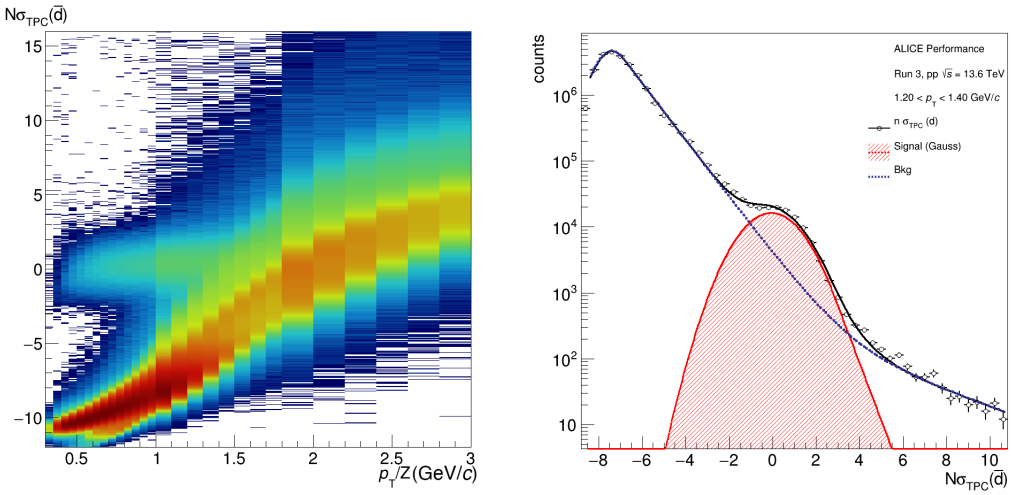

Figure 4.8: On the left, the $\mathrm{N}_{\sigma}^{\mathrm{TPC}}$ distribution for $\overline{\mathrm{d}}$ as a function of $p_{\mathrm{T}}/|z|$ in pp collisions at $\sqrt{s} = 13.6$ TeV is reported. The $\overline{\mathrm{d}}$ signal is centered around 0 and can be separated from the $\overline{\mathrm{p}}$ signal (red band) up to 1.5 GeV/c. On the right, the $\mathrm{N}_{\sigma}^{\mathrm{TPC}}$ ($\overline{\mathrm{d}}$) distribution is integrated in the $p_{\mathrm{T}}/|z| = (1.2 - 1.4)$ GeV/c interval. The distribution is fitted with a two-component fit function (black) obtained as the sum of a gaussian function to shape the signal (in red) and the sum of a gaussian function (to fit the proton signal) and of an exponential function for the background (in blue).

can be eventually inferred as

$$m = p\sqrt{\left(\frac{t_{\mathrm{TOF}} - t_0}{L}\right)^2 - 1}\,, \tag{4.5}$$

where t_0 is the *start time* (or *event time*). In the LHC, the bunches have a small but finite size. Henceforth, it is not known which one of the particles in the bunch have collided. This causes the event (collision) time to have an uncertainty with respect to the nominal beam crossing. For this reason, the event time is measured on an event-by-event basis and it is measured by the FT0 detector (see Section 3.2.4).

Another approach to PID with TOF makes use of the $n\sigma$ estimator, defined as

$$\mathrm{N}_{\sigma,i}^{\mathrm{TOF}} = \frac{t_{\mathrm{TOF}} - t_0 - t_{\mathrm{exp},i}(m_i, p, L)}{\sigma_{\mathrm{TOF}}(m_i, p, t_0)} \tag{4.6}$$

where L is the length of the track, p is the momentum of the track measured by the TPC and t_{TOF} is the measured hit time by the TOF, $t_{\mathrm{exp},i}$ is the expected time for a particle of mass m_i, and σ_{TOF} is the resolution on the particle time-of-flight. The expected time is computed during the track reconstruction procedure in the TPC and takes into account the variation of the momentum as the particle looses energy in the gas [129].

The resolution of the measured time-of-flight depends on various contributions, as introduced in Eq. 3.1. Some of the contributes are due to the detector itself (the intrinsic

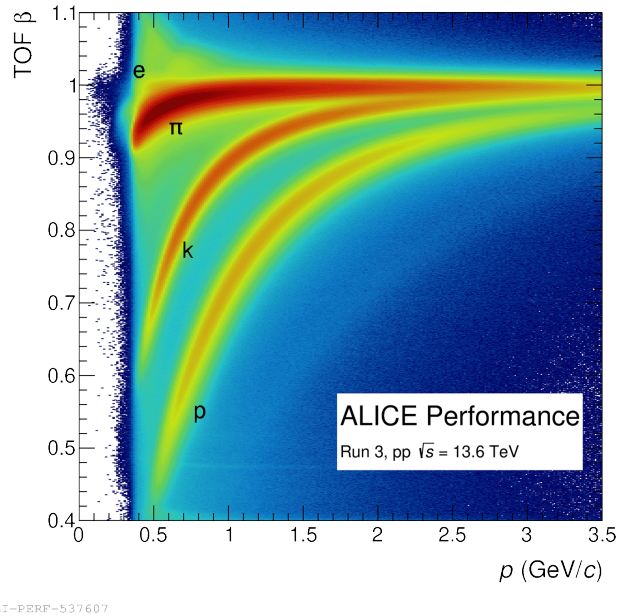

Figure 4.9: Particle velocity $\beta = v/c$ obtained with the TOF information vs p. The name of the particles identified are put on the plot. Data are from pp collisions at $\sqrt{s} = 13.6$ TeV.

MRPC resolution σ_{MRPC} and the resolution of the readout electronics σ_{Electr}), while other contributes are due to the reconstructed momentum resolution σ_p and the resolution on the start time σ_{t_0} calculated by the FIT detector.

In Fig. 4.10 and Fig. 4.11 the TOF PID response in terms of $\mathrm{N}_{\sigma}^{\mathrm{TOF}}$ is reported (for π and p, respectively). The $\mathrm{N}_{\sigma}^{\mathrm{TOF}}$ versus p_{T}/z distributions are used to check the PID response calibration quality in Asynch-QC, in the same way described for TPC response in Section 4.2. The distributions of the $\mathrm{N}_{\sigma}^{\mathrm{TOF}}$ are expected to be centred around 0 and with a width of 1. The data in Fig. 4.10 and Fig. 4.11 show the expected TOF response.

The TOF PID optimal momentum range is $p = (1 - 3)$ GeV/c. Particles with very low momenta ($p_{\mathrm{T}} \leq 0.5$ GeV/c) do not reach the detector or are absorbed by the innermost sub-detectors, while very high momenta particles are ultra-relativistic and cannot be separated, as $\beta = 1$.

4.2.1 Light (anti)nuclei identification with TOF

The TOF PID for light (anti)nuclei analyses is performed using the TOF-reconstructed mass values m (Eq. 4.5) by computing the difference between m and the nominal mass of the searched particle (e.g. m_{PDG}, if the value is taken from the Particle Data Group [25] tables). This variable ($\Delta m = m - m_{\mathrm{PDG}}$) distribution is expected to be a bell curve centred around the null value. The width of the distribution is due to the detector response and the statistical uncertainties on every measurement. At the sides of the target particle (e.g. ^{3}He) bell curve, more additional curves are expected: some are due the particles that are lighter

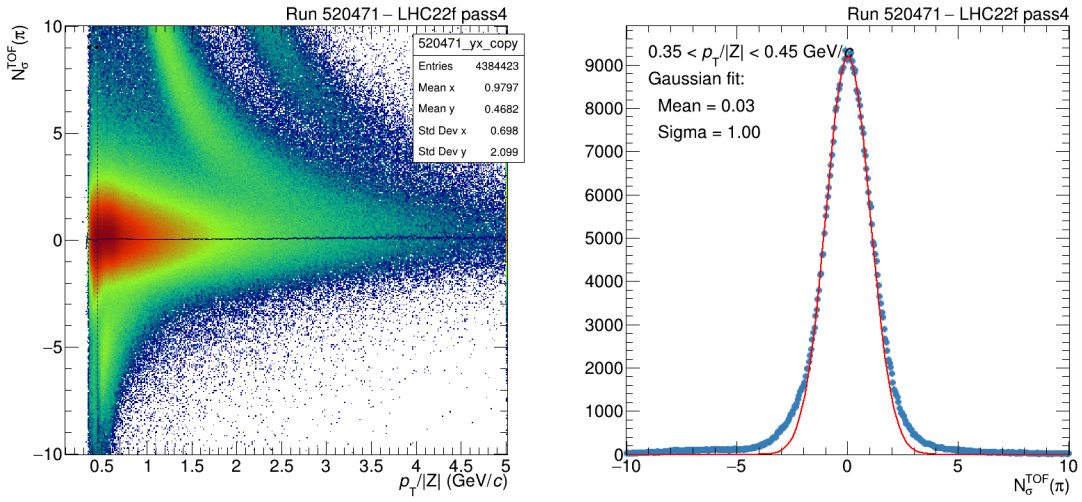

Figure 4.10: TOF response for the π hypothesis. On the left, the N_σ^{TOF} distribution is plotted as a function of $p_T/|z|$, while on the right the response is integrated in the $p_T/|z| = (0.35 - 0.45)$ GeV/c range.

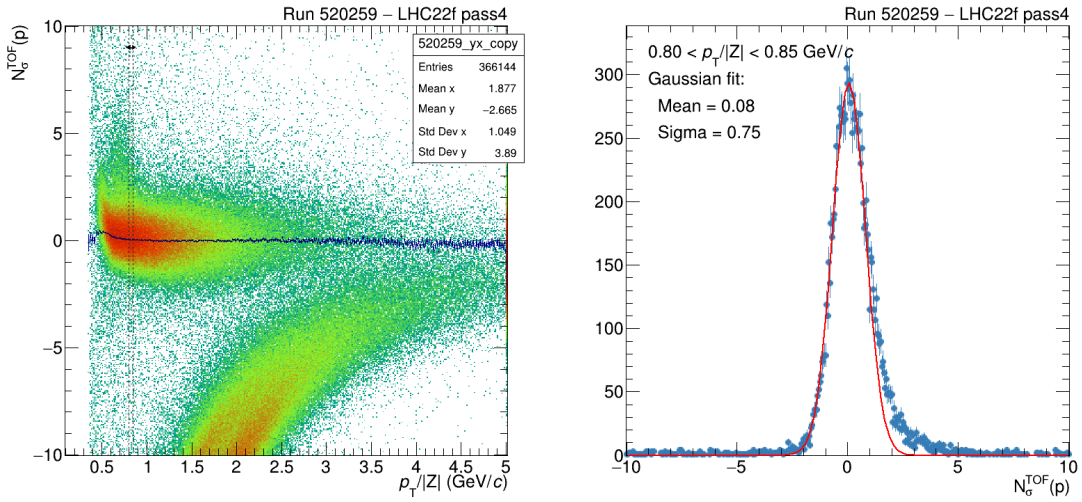

Figure 4.11: TOF response for the p hypothesis. On the left, the N_σ^{TOF} distribution is plotted as a function of $p_T/|z|$, while on the right the response is integrated in the $p_T/|z| = (0.80 - 0.85)$ GeV/c range.

than the target particles (e.g.) and some for the particles that are heavier (e.g. ^{4}He). An alternative, used in this analysis, is to extract the signal of interest from the difference of the squared power of the masses instead ($\Delta M^2_{TOF} = m^2_{TOF} - m^2_{\rm PDG}$). The use of a PID procedure based on the mass instead of the N_σ^{TOF} provides a better control on the PID dependence on the detector resolution (due to the denominator of Eq. 4.6). As an example,

the ΔM^2_{TOF} distribution as a function of rigidity is reported for the case of deuteron in Fig. 4.12 (left panel), together with a projection for a given rigidity interval (right panel).

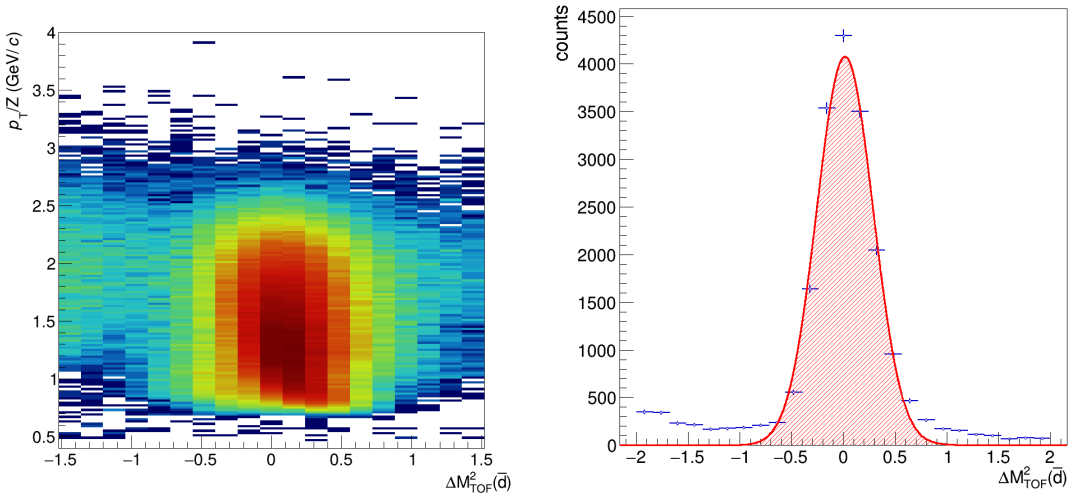

Figure 4.12: On the left, the $\Delta M^2_{\mathrm{TOF}}(\bar{\mathrm{d}})$ distribution as a function of p_{T}/z in pp collisions at $\sqrt{s} = 13.6$ TeV is reported. On the right, the $\Delta M^2_{\mathrm{TOF}}(\bar{\mathrm{d}})$ distribution is projected in the $p_{\mathrm{T}}/z = (1.8 - 2.0)$ GeV interval.

The reconstructed mass is strongly dependent on the ALICE tracking procedure, as, in particular, it relies on the measurements of the TPC momentum and track length. The TOF PID performance without any preselection of the candidates is not ideal, due to the possible track mismatch, that is the wrong association of TOF hits with tracks reconstructed by the TPC. Additionally, this technique should not distinguish tritons and helions, as they have the same mass. In the practical, a separation between these species is implemented as the ALICE detector measure the rigidity and the charge dependence is taken into account in the mass reconstruction process. For these reasons, the TOF PID used in this analysis is a combination of TPC and TOF PID (labelled as TPC+TOF): the tracks are preselected with the TPC inside a defined interval of $n\sigma_{\mathrm{TPC}}$ and then the TOF PID is then performed only on these preselected candidates. As the TPC identifies hadrons disambiguously at low p_{T}, this method allows one to extend the PID p_{T} range using the TOF mass-based method in a range in which the particles in the TPC are MIPs.

With reference to the right panel of Fig. 4.12 it can be observed that the measured signal is not perfectly Gaussian. This is due to the fact that the measured time-of-flight signal shape is not Gaussian [129], and ultimately, this shape affects also the reconstructed masses distribution. Following the same technique used for the TPC PID, in order to extract particle yields based on the TOF signal distributions, these are fitted with a function that is the sum of a signal, a gaussian function with an exponential tail, and a background component appropriately chosen. Further details on the TOF fit function used for the analysis of ^{3}He and $^3\overline{\mathrm{He}}$ are given in Chap. 5.

Chapter 5

(Anti)helium production in pp collisions at $\sqrt{s}$ = 13.6 TeV

The analysis for the measurement of the (anti)helium production in pp collisions at $\sqrt{s} = 13.6$ TeV follows the steps summarised below:

- First, a custom calibration of the TPC response is performed to allow for a selection of the (anti)helium candidates. This is necessary to compensate for the imperfect calibration of the tracking for particles with charge $|z| > 1$. Details on this procedure were presented in Section 4.1.1.
- The identification of ^{3}He and $^3\overline{\text{He}}$ candidates is performed using the TPC and the TOF information. Two analyses, one based on TPC-only PID and one based on the combined information of TPC and TOF (TPC+TOF), are carried out in parallel.
- For the TPC analysis, the signal is extracted based on the $\text{N}_\sigma^{\text{TPC}}$ (^{3}He) distributions, which are fitted with an appropriate function that accounts for both the ^{3}He ($^3\overline{\text{He}}$) signal and background. The raw yield is obtained by integration of the signal function.
- For the TPC+TOF analysis, candidates are pre-selected using a loose $5\sigma_{TPC}$ selection, then the TOF information is used to compute the mass squared of the particle, m^2_{TOF}. The ^{3}He signal is obtained from the distribution of $\Delta M^2_{\text{TOF}} = m^2_{TOF} - m^2_{^3\text{He}}$ and bin counting is used to extract the raw signal counts in each p_{T} bin. Both strategies are applied in the range $p_{\text{T}} \in (1.50, 5.0)$ GeV/c. Whereas the event and track selection criteria are summarised in Section 5.1, the signal extraction is described in Section 5.2.
- Sources of systematic uncertainties are discussed in Section 5.4.
- The p_{T}-dependent raw yields, or spectra, are then normalized for the number of collisions and corrected for acceptance, efficiency and primary fraction (helium only), as described in Section 5.3.
- The obtained corrected spectra are integrated to extract p_{T}-integrated yields $\text{d}N/\text{d}y$ with the help of a function to extrapolate in the unmeasured p_{T} range, and discussed in Section 5.5.

5.1 Event and track selection

The analysis is carried out on a large dataset of pp collisions at $\sqrt{s} = 13.6$ TeV collected with the ALICE detector in 2022.

First, collision events are selected based on the distance of the reconstructed primary vertex from the nominal interaction point, in order to maximise the number of particles in the ITS acceptance. The primary vertex position is described by three coordinates in the ALICE framework, $\mathbf{V} = (V_x, V_y, V_z)$, where V_x and V_y describe the position on the transverse plane with respect to the LHC beam and V_z describes the position on the longitudinal axis. Only events with $|V_z| < 10$ cm are accepted. An example, for pp at $\sqrt{s} =$ 13.6 TeV collisions, is reported in Fig. 5.1.

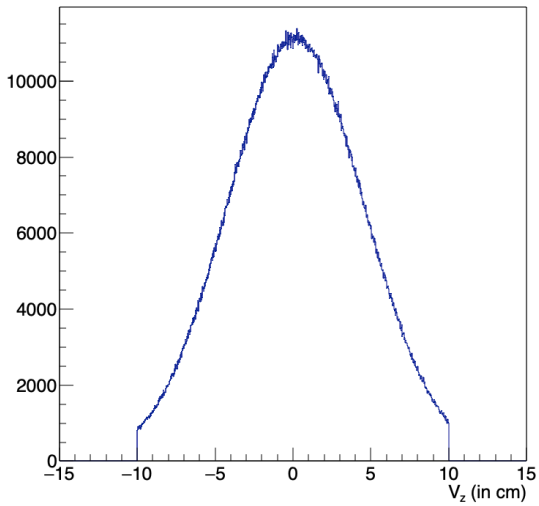

Figure 5.1: Distribution of the reconstructed vertex position along the Z direction (i.e. along the beam) in pp collisions at $\sqrt{s} = 13.6$ TeV. The events are selected with $|V_z| < 10$ cm.

The event selection has been performed with the standard event selection task `o2-analysis-event-selection`[1]. In particular, good events are required to have `sel8()` flag turned on. This tag require the event to trigger both FT0 scintillators on both of the side of the collision vertex.

The dataset used for the analysis (see Appendix A) is characterised by an interaction rate (IR) of around 500 kHz and a low pile-up probability ($\mu < 0.1$). The pile-up happens when in a single bunch-crossing event, more than one couple of protons collide. The probability of having k collision events in the same bunch crossing is described by the Poisson

[1] https://github.com/AliceO2Group/O2Physics/blob/master/Common/TableProducer/eventSelection.cxx

distribution,

$$p(k,\mu) = \frac{ke^{-\mu}}{k!}\,. \tag{5.1}$$

The number of events analysed after applying the event selection conditions is $4.63 \cdot 10^{11}$ (74% of the full statistic).

Tracks in the pseudorapidity region $|\eta| < 0.8$ are selected to use only the fiducial region in which the experiment provides full track reconstruction and particle identification based on information of the TPC and the TOF. Additionally, only tracks with $p/z > 0.3$ GeV/c are selected. In order to select good reconstruction-quality tracks, these are required to have at least 120 TPC space points and at least one hit in Inner Barrel of the ITS (ITS2-IB). In addition, as a consequence of the track-matching algorithm between ITS and TPC, only tracks with at least six ITS2 clusters get selected. Tracks with a minimum number of 70 out of 159 fired readout rows in the TPC are selected, while tracks with a ratio between the number of crossed rows and the number of findable clusters smaller than 80% are rejected. A representation of the TPC segmentation into rows and sectors is shown in Fig. 5.2. Only the tracks with χ^2 per ITS cluster smaller than 36 and χ^2 per TPC cluster available for the reconstruction smaller than 4 are selected. Finally, the selected tracks are required to be refitted both in TPC and ITS.

Similar track-quality selection criteria were also employed for similar analyses based on the Run 2 data and experience [23].

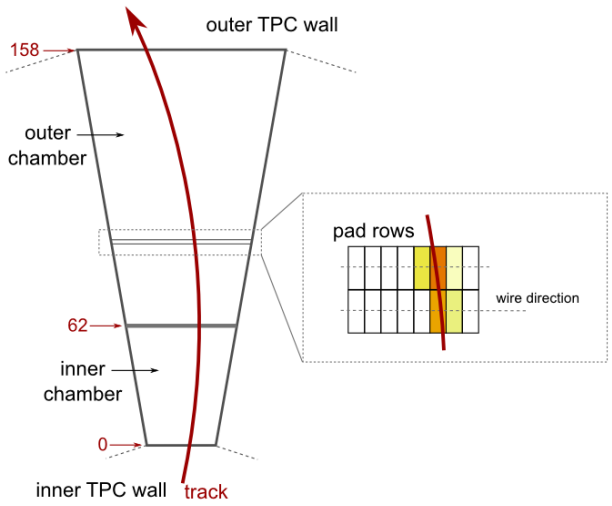

Figure 5.2: TPC readout segmentation into sectors and pad rows [130].

Primary helium (see Chapter 4) are characterised by a DCA distribution peaked at zero. Secondary helium nuclei are mainly produced via knock-out from the interactions of the primary particles with the material of the beam pipe and of the experimental apparatus. Only helium, and no antihelium, is produced from the interaction with the material, due to the conservation of the baryon number. Additional sources of secondary helium and antihelium are given by the decay of the hypertriton ${}^{3}_{\Lambda}\mathrm{H} \rightarrow {}^{3}\mathrm{He} + \pi$, with branching ratio

theoretically estimated to be 0.25 [131], and similarly for antimatter. However, since in pp collisions the production of light hypernuclear matter with three baryons is rare [132], this contribution can be neglected for these samples.

To reduce the contribution of the secondary helium, selections based on the distance of closest approach of the track to the primary vertex in the xy plane and along z separately are applied. The DCA selections are $|\mathrm{DCA}_{xy}| \leq 0.5$ cm and $|\mathrm{DCA}_z| \leq (4 \times 10^{-4} + 1.3 \times 10^{-2}/p_{\mathrm{T}})$ cm. The DCA_{xy} selection is parametrised as a function of p_{T} as the best precision is achieved in the xy plane.

The track selection setup is summarized in Tab. 5.1:

minimum number of crossed rows in TPC	$N_{\mathrm{cr,TPC}} \geq 70$
minimum number of clusters in TPC	> 120
ratio of number of crossed rows to findable clusters in TPC	$R_{\mathrm{TPC}} \geq 0.8$
maximum χ^2 per cluster in TPC	$\chi^2_{\mathrm{TPC}} < 4$
kink daughters	rejected
require ITS and TPC refits	true
minimum number of clusters in ITS2-IB	1
$\lvert\mathrm{DCA}_{xy}\rvert$	$\leq 4 \times 10^{-4} + 1.3 \times 10^{-2}/p_{\mathrm{T}}$ cm
$\lvert\mathrm{DCA}_z\rvert$	≤ 0.5 cm
minimum number of clusters in ITS	≥ 6
maximum χ^2 per cluster in ITS	$\chi^2_{\mathrm{ITS}} < 36$
$\lvert\eta_{\mathrm{track}}\rvert$	<0.8
$\lvert y\rvert$	<0.5

Table 5.1: List of track selection criteria for this analysis.

In addition, tracks that are supposed to have a TOF signal matched are required to pass the `hasTOF()` condition (namely having a *hit* in the TOF detector). With these selections of events and tracks, the PID signals in TPC and TOF are reported in Fig. 5.3 for the sample of pp collisions at $\sqrt{s} = 13.6$ TeV. In the figure on the left, the pion and kaon candidate signals were cut from the selection. After particle identification, the particles are selected to have rapidity $|y| < 0.5$.

5.2 Signal extraction

5.2.1 Antihelium signal

TPC PID

After the recalibration of the TPC response (see Section 4.1.1), the $^3\overline{\mathrm{He}}$ signal can be extracted by the recalibrated $\mathrm{N}^{\mathrm{TPC}}_{\sigma,i}$ vs p_{T} distributions. To extract the yield of $^3\overline{\mathrm{He}}$ from the $n\sigma_{\mathrm{TPC}}$ distribution, the global fit function used is given by

$$f^{\mathrm{TPC}}_{\mathrm{global}} = \mathrm{AsymmGauss}(^3\overline{\mathrm{He}}) + \mathrm{AsymmGauss}(\overline{\mathrm{d}}) + \mathrm{ExpBg}. \tag{5.2}$$

The anti-helium signal is fitted with an asymmetric Gaussian distribution function,

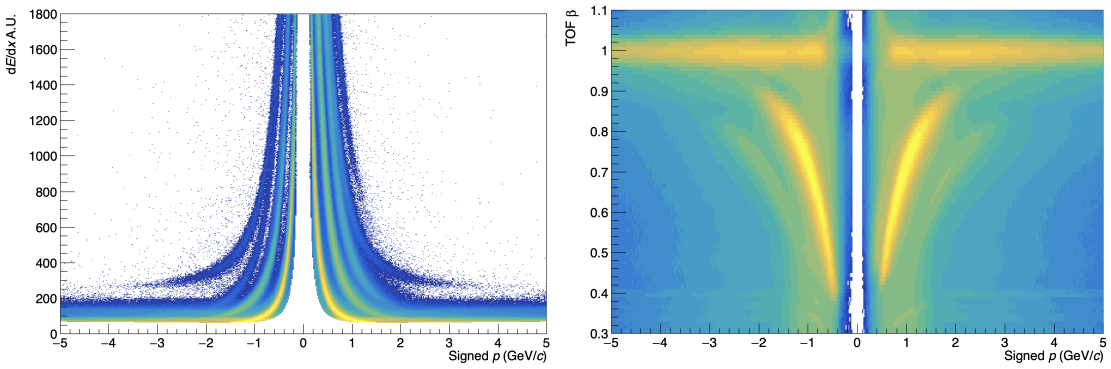

Figure 5.3: Performance of the TPC (left) and the TOF (right) detectors for PIDd sample of pp collisions at $\sqrt{s} = 13.6$ TeV. In the left plot, the pion and kaon candidates have been rejected, therefore, the visible bands are for protons, deuterons, helium nuclei and their antiparticles.

AsymmGauss($^3\overline{\text{He}}$), which is a Gaussian distribution with an exponential tail, defined as:

$$S(x; N, \mu, \sigma, n) \propto N \begin{cases} \exp\left[-\frac{1}{2}\left(\frac{x-\mu}{\sigma}\right)^2\right] & \text{for } x \leq \mu + n\sigma \\ \exp\left[-n\left(\frac{x-\mu}{\sigma} - \frac{n}{2}\right)\right] & \text{for } x > \mu + n\sigma \end{cases} \tag{5.3}$$

where N is the number of signal counts, μ and σ are the mean and the standard deviation of the gaussian respectively, while $n\sigma$ define the value at which the function becomes an exponential function. AsymmGauss($\overline{\text{d}}$) is an asymmetric Gaussian distribution function defined as Eq. 5.3, but centred in the mean $\text{N}_\sigma^{\text{TPC}}$ (^{3}He) value expected for the $\overline{\text{d}}$.

The background component is taken account by the function ExpBg, given by an exponential

$$\text{ExpBg} = ae^{bx} + c, \tag{5.4}$$

with a, b, c taken as free parameters. The fit is based on the χ^2 minimization. In each p_{T} bin, the fit is performed in a p_{T}-dependent range, $x_{low} < n\sigma_{\text{TPC}} < x_{up}$, with $x_{low} \in (-12, -6)$ and $x_{up} \in (6, 8)$.

Examples of fits are reported in Fig. 5.4 for one low and one intermediate p_{T} bins, whereas for the other bins of the analysis the fits are reported in Appendix B.

The parameters obtained from the fit to the TPC signal function for $^3\overline{\text{He}}$ as well as the reduced χ^2 values are reported in the left panel of Fig. 5.6, where it can be observed that the mean and pull of the $\text{N}_\sigma^{\text{TPC}}$ distributions are centred around zero and one[2], respectively. The mean values μ, even if centred around 0, nevertheless shows a p_{T} dependence which is almost linear in the $\mu = (-0.5, 0.5)$ range. This dependence is probably related to the tracking algorithm used in the reconstruction pass used in this analysis (`pass4`). The tracks were reconstructed by the algorithm treating all the tracks as they are pions (as pions are the most abundant hadrons produced in high energy collisions). This assumption is as

[2]By definition, a distribution in n_σ for a Gaussian-like PID response is expected to be a gaussian centred at $\mu = 0$ and with $\sigma = 1$, see Section 4.1.

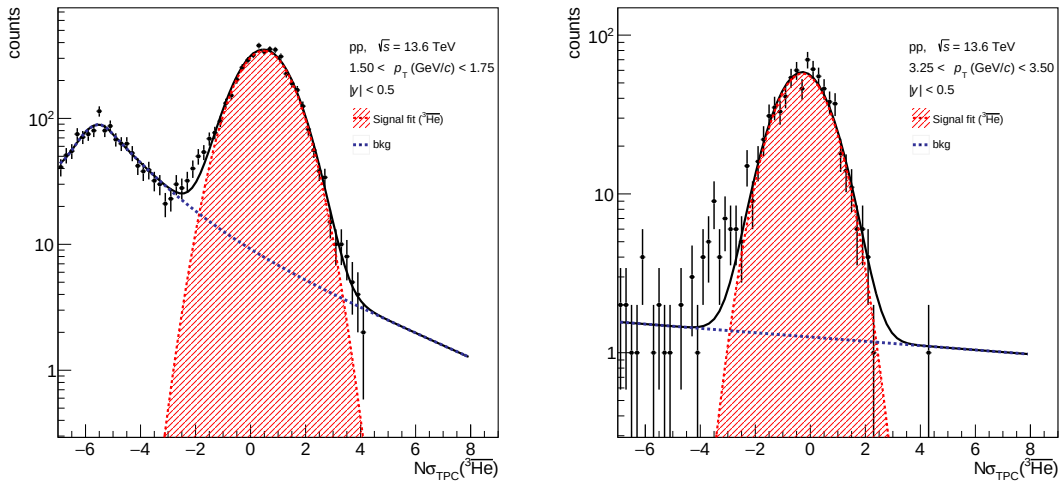

Figure 5.4: Examples of $^3\overline{\text{He}}$ yield extraction in pp collisions at $\sqrt{s} = 13.6$ TeV with TPC in two p_{T} bins. The $^3\overline{\text{He}}$ TPC-nσ distribution is fitted with the global function Eq. 5.2, which is shown with the black solid line. The data points are given by black markers, the red solid line represents the signal, the blue dashed line is the exponential background.

correct as high is the particle energy. For heavier particle (like nuclei) at low momentum, corrections are needed. The TPC calibration "tempers" partially this issues and the mean values are centred around zero, but still some divergences are expected. The good quality of the TPC response calibration is supported by the fact the the width are centred around unity, as expected in the ideal case. The reduced χ^2 values are between 0.7 and 2.5, with an higher value for $p_{\text{T}} \sim 2.25$ GeV/c.

The yields in each p_{T} bin are obtained from the integral of the $^3\overline{\text{He}}$ signal function calculated within the range $\mu \pm 5\sigma$, where μ and σ are those extracted from the fit. The raw yields are reported in the top panel of Fig. 5.7.

TOF PID

To perform particle identification with the TOF, the antihelium tracks are pre-selected within the $\pm 5\sigma_{TPC}$ range to reduce contamination of wrongly-associated TOF hits to TPC tracks (*mismatched* tracks). The signal of (anti)helium is extracted by calculating the mass squared of the candidate particle using the TOF-measured time-of-flight, the momentum and track length from the TPC (see Eq. 4.5 in Sec. 4.2). The $\Delta m^2_{\text{TOF}} = m^2_{\text{TOF}} - m^2_{^3\text{He}}$ distributions are fitted with global fit function:

$$f^{\text{TOF}}_{\text{global}} = \text{AsymmGauss}(^3\overline{\text{He}}) + \text{Bkg}\,. \tag{5.5}$$

The AsymmGauss($^3\overline{\text{He}}$) function is the signal of the $^3\overline{\text{He}}$, while the background Bkg is given by a first-degree polynomial function:

$$\text{Bkg} = ax + b \tag{5.6}$$

The non-Gaussian behaviour of the reconstructed mass distribution is a consequence of the almost identical behaviour observed in the $t_{\rm TOF}$ distribution [129]. The non-Gaussian tail on the right side of the peak was discovered after the first data with collisions were recorded and it was not observed during the test beams phase [129]. The origin of this non-Gaussian contribution was extensively discussed in the years and several explanations were proposed. One reason can be found in the residual miscalibrations that can induce a tail in the signal. Another contribution to the tail could be due to delayed signals that have origin from weak decays, creating a background correlated with the signal.

The fit is based on the χ^2 minimization. Examples of fits are reported in Fig. 5.5 for two $p_{\rm T}$ bins, whereas for other bins the fits are reported in Appendix B. The parameters obtained from the fit of the TOF signal for $^3\overline{\rm He}$ are reported in Fig. 5.6 (on the right panel), where it can be seen that the mean and width of the distributions are around 0.2 and 0.8, respectively.

The raw yield is then extracted using the bin counting technique: the signal is the sum of the histogram bin content in the range $(-5\sigma+\mu, 5\sigma+\mu)$, where μ and σ extracted from the fit. Raw yields obtained with this PID strategy are reported in Fig. 5.7 (at the lower panel). In the same figure, the yield extracted with bin counting has been compared with the yield extracted by integrating the fitting function in the range $\mu \pm 5\sigma$. In the bottom panel of Fig. 5.7, it can be observed that the ratio is compatible with unity.

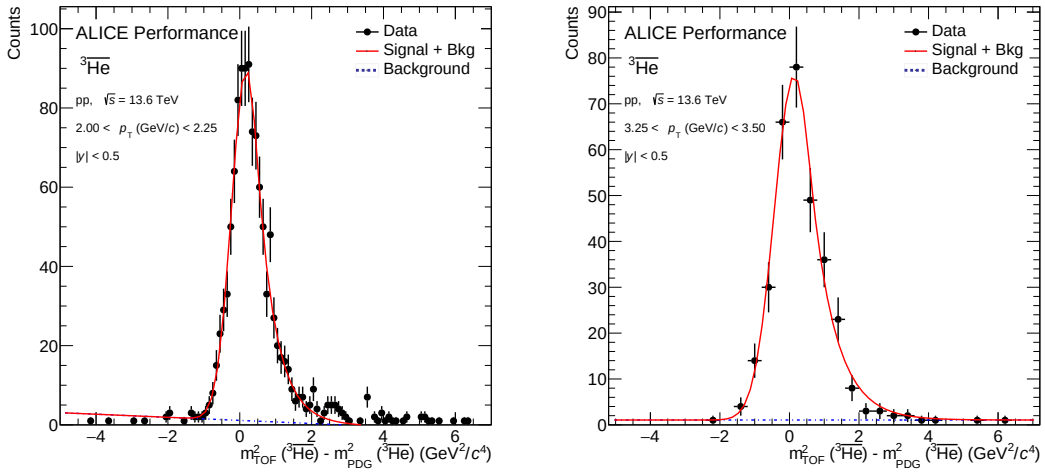

Figure 5.5: Examples of $^3\overline{\rm He}$ yield extraction in pp collisions at $\sqrt{s} = 13.6$ TeV with TOF in two $p_{\rm T}$ bins. The $^3\overline{\rm He}$ TOF-nσ distribution is fitted with the signal function which is shown with the red solid line. The data points are marked with black lines.

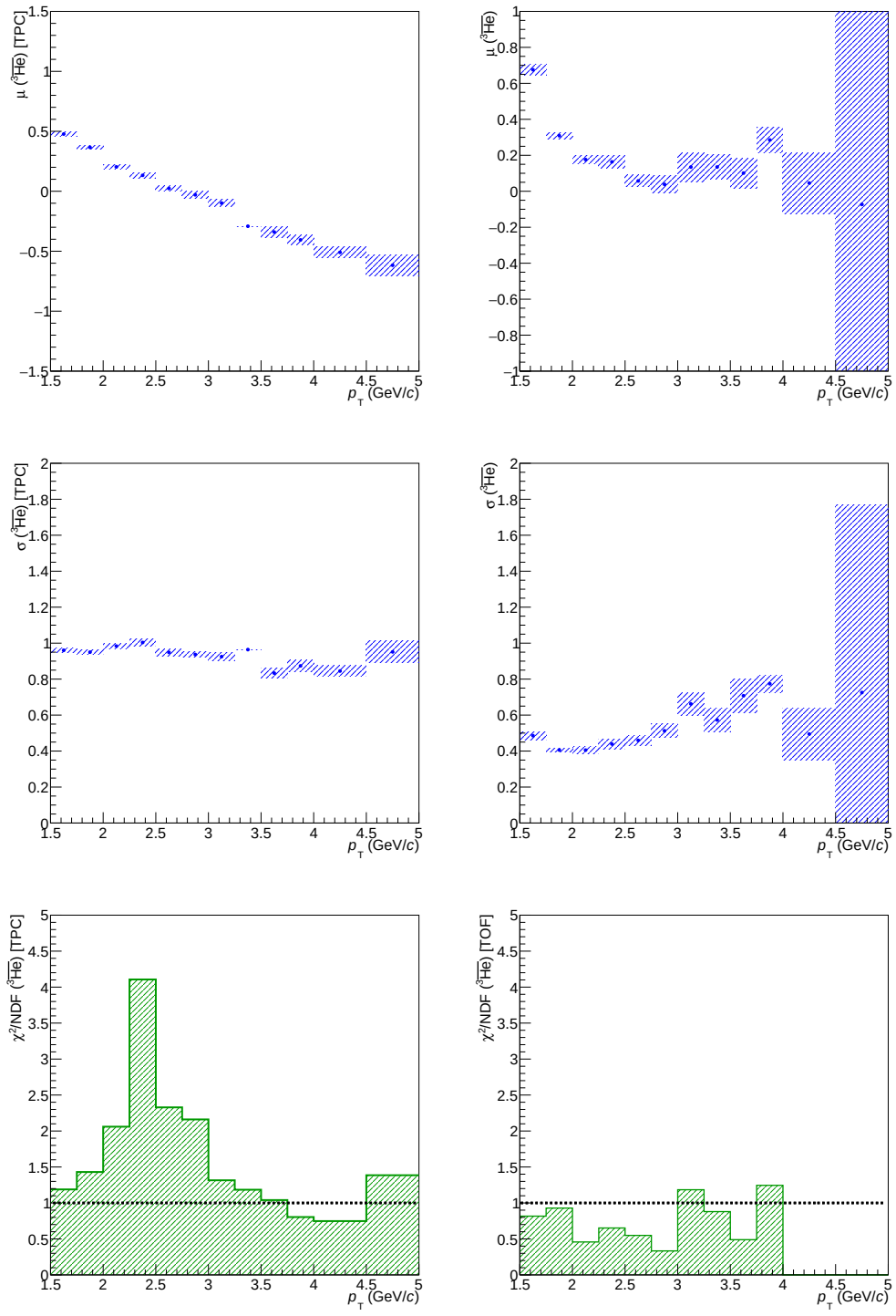

Figure 5.6: Parameters obtained from the fit of the signal of the $^3\overline{\mathrm{He}}$ in pp at 13.6 TeV. The mean values (top row), the width (central row) and the reduced χ^2 (bottom row) are shown for both the TPC (on left side) and the TPC+TOF (on the right side) PID.

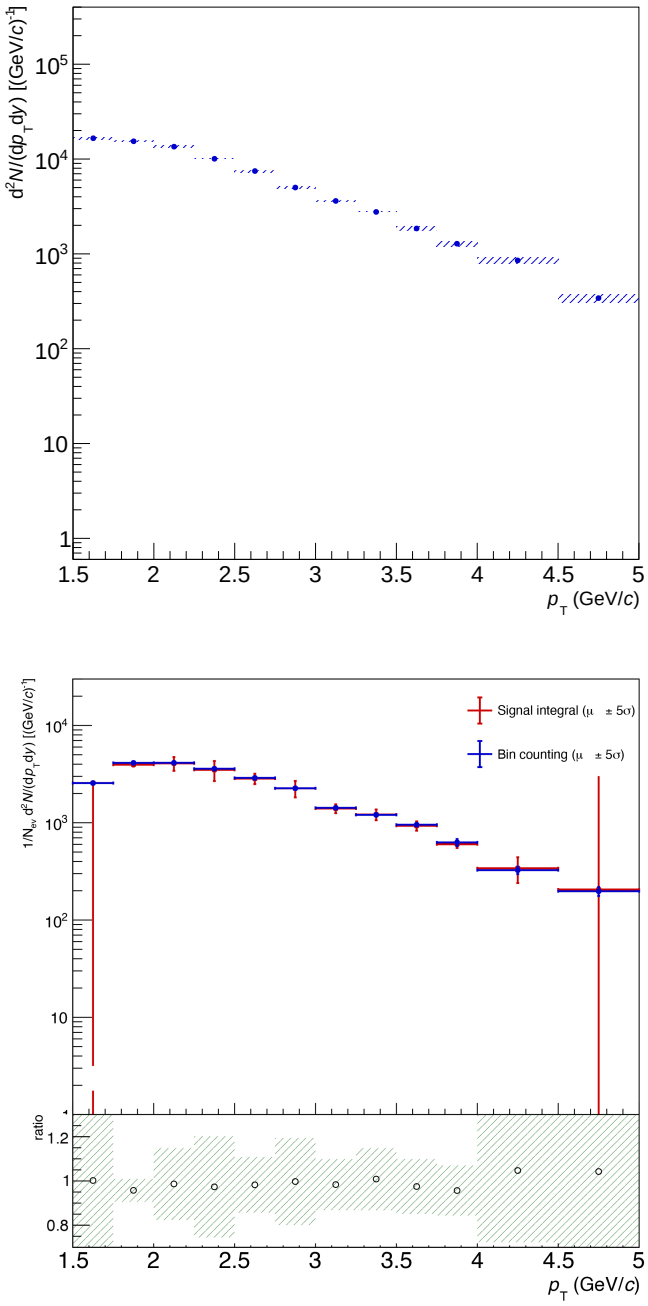

Figure 5.7: (On the top panel) Raw yields for $^3\overline{\mathrm{He}}$ extracted with TPC PID in pp at $\sqrt{s}$ = 13.6 TeV as a function of p_{T}. Boxes represent statistical uncertainties.
(On the bottom panel) Comparison between bin counting method (in blue) and signal function integration (in red) for $^3\overline{\mathrm{He}}$ yield extraction in pp collisions at $\sqrt{s}$ = 13.6 TeV. Bars represent statistical uncertainties. In the lower part of the panel, function integration over bin counting ratio is shown. This work.

5.2.2 Helium signal

TPC PID

To extract the yield of helium from the $n\sigma_{\mathrm{TPC}}$ distribution, the global fit function used is given by

$$f_{\mathrm{global}} = \mathrm{AsymmGauss}(^3\mathrm{He}) + \mathrm{AsymmGauss}(d) + \mathrm{AsymmGauss}(\alpha) + \mathrm{ExpBg}. \quad (5.7)$$

The ^{3}He signal is fit by the AsymmGauss(^{3}He) function, a Gaussian distribution with an exponential tail defined by Eq. 5.3. Two more asymmetric gaussians are used to describe the contamination from deuteron and alpha (^{4}He) signals (the alpha function is included only in the range $p_{\mathrm{T}} < 2$ GeV/c, where the signal is visible) and an exponential function, ExpBg as in Eq. 5.4, accounts for the background.

The anti-alpha signal was not observed in the $^3\overline{\mathrm{He}}$ TPC response (see Section 5.2.1). As explained in Chapter 2, the expected production of primary ^{4}He ($^4\overline{\mathrm{He}}$) particles in pp collisions at $\sqrt{s} = 13.6$ TeV is approximately one thousand times smaller with respect to that of ^{3}He ($^3\overline{\mathrm{He}}$). Due to knock-out processes (see Chapter 4), secondary positively-charged alpha particles are produced inside the detector and hence detected. These particles increase significantly the α (and ^{3}He) signal in the detectors and this explains why different fit functions are needed for positive and negative particles.

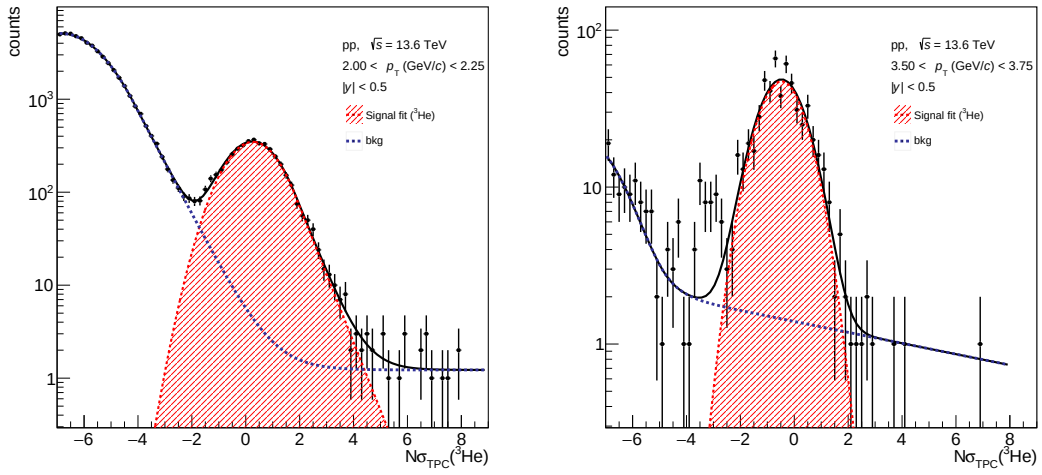

Figure 5.8: Examples of ^{3}He yield extraction in pp collisions at $\sqrt{s} = 13.6$ TeV with TPC in two p_{T} bins. The ^{3}He $\mathrm{N}_\sigma^{\mathrm{TPC}}$ distribution is fitted with the global function Eq. 5.7, which is shown with the black solid line. The data points are black markers, the red solid line represents the signal function and the blue dashed line is the backgorund.

In each p_{T} bin, the fit to the $\mathrm{N}_\sigma^{\mathrm{TPC}}$ distribution, based on the χ^2 minimization, is performed in a p_{T} dependent range, $x_{low} < \mathrm{N}_\sigma^{\mathrm{TPC}} < x_{up}$, with $x_{low} \in (-12, -6)$ and $x_{up} \in (6, 8)$. Examples of fits are reported in Fig. 5.8 for two p_{T} bins. The other bins are shown in Appendix B.

The mean values and width of the signal are shown in the left panel of Fig. 5.10, as also the reduced χ^2 distribution. The mean values are centred around 0 and show the p_{T}-dependence discussed in the previous section. The width of the $\mathrm{N}_{\sigma}^{\mathrm{TPC}}$ are compatible with unity within their uncertainties. The reduced χ^2 is very high in the first two bin and shows a tension for $p_{\mathrm{T}} \sim 2.5$ GeV/c. As it will be discussed in Section 5.6 in details, the first two bins are removed from the analysis results.

The yields in each p_{T} bin are obtained integrating the ^{3}He signal function calculated within the range $\mu \pm 5\sigma$, where μ and σ are those extracted from the signal function fit. The obtained raw yield is shown in the top panel of Fig. 5.11.

TOF PID

The signal extraction is performed combining a pre-selection with TPC and the a particle identification with TOF. The helium candidates are pre-selected within the $5\sigma_{TPC}$ range.

The raw yield of helium is extracted from $\Delta m^2_{\mathrm{TOF}}$. The distributions are fitted with an asymmetric Gaussian (Eq. 5.3). The fit is performed with `ROOT`, using the binned maximum likelihood method. The raw yield is then extracted using the bin counting technique: the signal is the sum of the histogram bin content in the range $(-5\sigma + \mu,\ 5\sigma + \mu)$, while the μ and σ extracted from the fit. The signal fit is shown for two different p_{T} bins in Fig. 5.9.

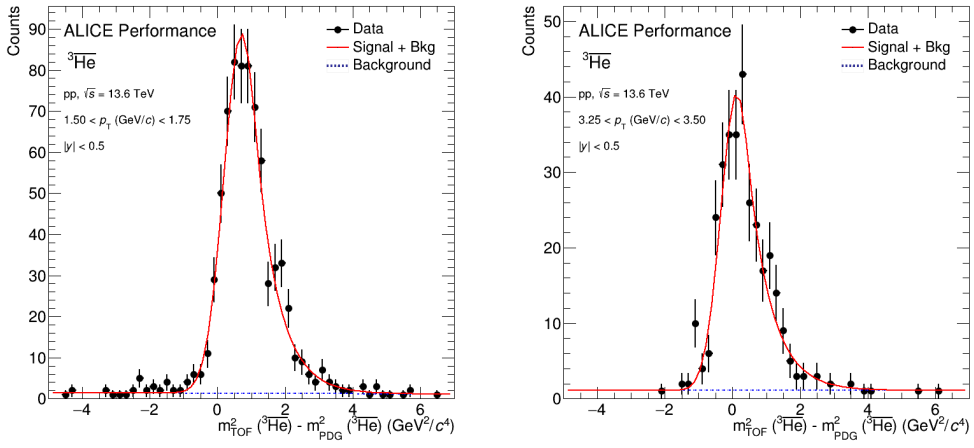

Figure 5.9: Examples of ^{3}He yield extraction in pp collisions at $\sqrt{s} = 13.6$ TeV with TOF in two p_{T} bins. The ^{3}He $\mathrm{N}_{\sigma}^{\mathrm{TOF}}$ distribution is fitted with the signal function which is shown with the red solid line, whereas the blue dashed line is the background. The data points are given by the black markers.

The values of μ, σ and the reduced χ^2 are shown in the right panel of Fig. 5.10. The mean values show a p_{T} dependence similar to the one observed in the TPC PID mean values, as the TOF PID is performed on a subset which is preselected by the TPC. This dependence supports the hypothesis that this behaviour is due to the approximation of all particle being tracked as pions in the reconstruction phase, which have significant effects at low p_{T} values.

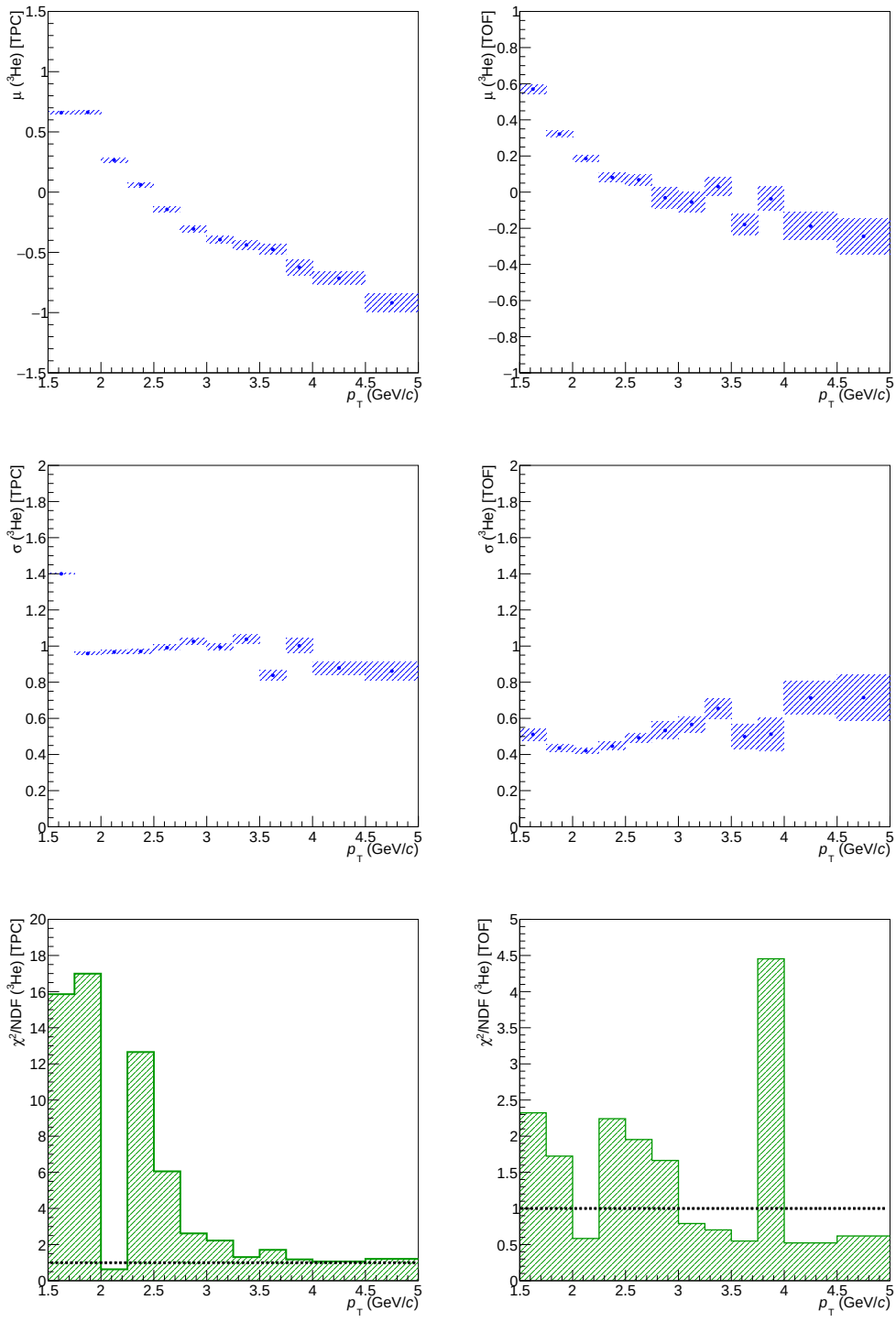

Figure 5.10: Parameters obtained from the fit of the signal of the $^3\overline{\mathrm{He}}$ in pp at 13.6 TeV. The mean values (top row), the width (central row) and the reduced χ^2 (bottom row) are shown for both the TPC (on left side) and the TPC+TOF (on the right side) PID.

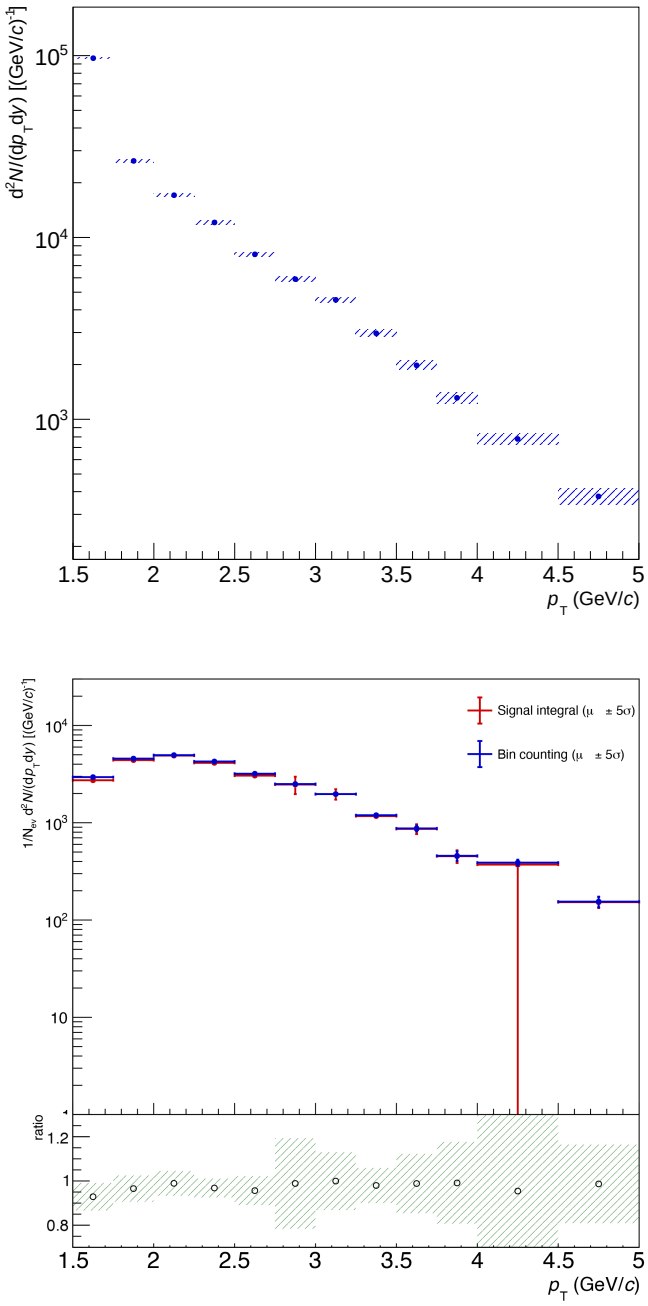

Figure 5.11: (On the top panel) Raw yields for $^3\overline{\mathrm{He}}$ extracted with TPC PID in pp at $\sqrt{s}$ = 13.6 TeV as a function of p_{T}. Boxes represent statistical uncertainties.
(On the bottom panel) Comparison between bin counting method (in blue) and signal function integration (in red) for $^3\overline{\mathrm{He}}$ yield extraction in pp collisions at $\sqrt{s}$ = 13.6 TeV. Bars represent statistical uncertainties. In the lower part of the panel, function integration over bin counting ratio is shown. This work.

The custom TPC calibration tempers this effect and the mean values are centred around zero. The width of the distribution is centred around ~ 0.6. The reduced χ^2 values are mostly below 2, except for a higher value at $p_{\mathrm{T}} = 3.75$ GeV/c.

Raw yields obtained with the described strategy are shown in the lower panel of Fig. 5.11. In the same figure, the yield extraction with bin counting has been compared with the yield extracted by integrating the fitting function in the range $\mu \pm 5\sigma$, with the ratio being compatible with unity.

The ratio of $^3\overline{\mathrm{He}}$ yields to the ^{3}He ones (antimatter/matter) is reported for both the TPC and the TPC+TOF analysis in the left panel of Fig. 5.12. In the right panel of Fig. 5.12 the TPC+TOF/TPC ratio is shown. The ratio shows a strong tension at lower p_{T} values for both ^{3}He and $^3\overline{\mathrm{He}}$ and reaches a constant value (~ 0.45) for $p_{\mathrm{T}} \geq 2.5$ GeV/c.

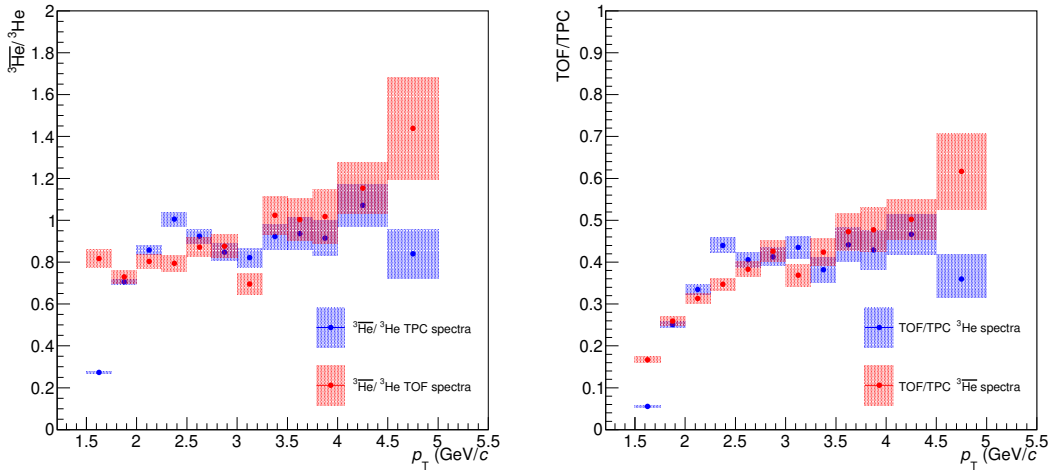

Figure 5.12: (Left) Comparison between the ratio of $^3\overline{\mathrm{He}}/^3$He raw yield estimated with TPC (in blue) and with TOF after TPC pre-selection (TPC+TOF, in red) in pp collisions at $\sqrt{s} = 13.6$ TeV. (Right) Comparison between the ratio of TPC+TOF/TPC for ^{3}He and $^3\overline{\mathrm{He}}$.

5.3 Corrections for (anti)helium-3

In order to correct the extracted raw yields of (anti)nuclei, several corrections are applied based on Monte Carlo (MC) simulations of pp collisions at $\sqrt{s}$ = 13.6 TeV, produced using `PYTHIA 8.3` [133] as event generator and `Geant4` [134] for the particle transport through the detector. More specifically, three MC datasets are employed, where the detector configuration and conditions during data taking are reproduced through an *anchoring* procedure. The first dataset, with $21.5 \cdot 10^6$ events, is a *general purpose* (GP) MC, featuring a perfect TPC calibration (no space charge effects in TPC, and thus no distorsions in tracking are reproduced) and ideal alignment of ITS and MFT. In addition to this, a second GP MC with $413.5 \cdot 10^6$ events is used. This MC is anchored to 2023 data and it doesn't reproduce the condition of the data taking, but it is used to extract deuteron DCA_{xy} distributions that can be used as a proxy for a secondary template. A third MC dataset with $19.4 \cdot 10^6$ generated events has injected signals of eight different species of nuclei, antinuclei and hypernuclei, one per event. As a consequence, a ^{3}He ($^3\overline{\mathrm{He}}$) particle is injected every eight generated event. These signals are injected with a uniform p_{T} distribution in the p_{T} range (0.2 - 10) GeV/c and in the $|y| < 1$ rapidity range. This MC is used mainly to estimate the reconstruction efficiency for the (anti)helium.

The $^3\overline{\mathrm{He}}$ raw yields are corrected to account for different factors:

- the shift between the generated p_{T} in Monte Carlo simulated data and the reconstructed p_{T} obtained by the measured rigidity (this effect is dubbed as p_{T}-*shift* in the following);
- the acceptance x efficiency ($A \times \epsilon$) of the detector;
- the contribution from secondary ^{3}He.

5.3.1 p_{T}-shift correction

The particles in the ALICE detector tracking algorithm are all treated as energy-losing charged pions, as these are the most abundant particles produced in the collisions. One of the side effects of this approach is that the real behaviour of heavier particles like nuclei during propagation is not perfectly reproduced. In particular, due to the large mass difference between nuclei and pions, this assumption biases the momentum estimation at low p_{T}, where the difference between the energy loss of pions and heavier particles is the largest. As no proper correction for this effect is implemented in the simulation, a p_{T}-shift is observed. In the MC dataset with (anti)(hyper)nuclei injection, the reconstructed momentum is systematically lower than the generated one, as observed comparing the generated and reconstructed (anti)particle p_{T} distribution. This effect has to be taken into account prior to estimate the $A \times \epsilon$ corrections from the MC. The shift has been estimated and corrected separately for both ^{3}He and $^3\overline{\mathrm{He}}$. The p_{T}-shift is visible in Fig. 5.13, where it is reported as a function of the reconstructed p_{T} The shift has been fitted with the following function

$$f_{p_{\mathrm{T}}} = Ae^{B+Cx} + D + Ex. \tag{5.8}$$

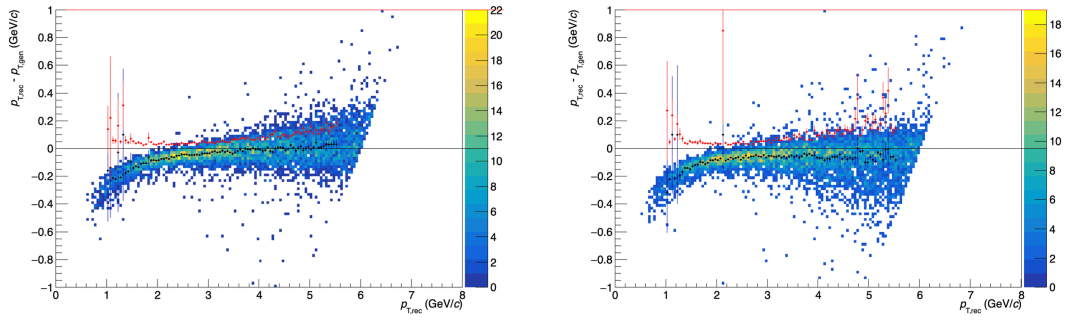

Figure 5.13: p_{T}-shift as a function of reconstructed p_{T} for ^{3}He (left) and $^{3}\overline{\mathrm{He}}$ (right), estimated with a nuclei-injected MC dataset. The mean values (in black) and the pull values (in red) of the profile fit is plotted on the distribution.

The parameters extracted from the fit are used to re-map the p_{T} values "on-the-fly" during the signal extraction, obtaining that the differences between generated p_{T} and reconstructed p_{T} are centred around zero, as in Fig. 5.14.

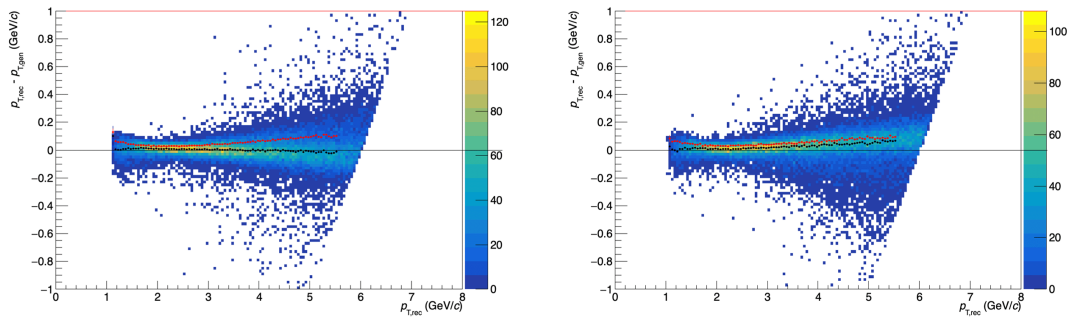

Figure 5.14: p_{T}-shift as a function of reconstructed p_{T} after the remapping. On the left the remapped ^{3}He p_{T}-shift is reported, on the right is the remapped $^{3}\overline{\mathrm{He}}$ p_{T}-shift. The mean values (in black) and the pull values (in red) of the profile fit is plotted on the distribution.

5.3.2 Acceptance × efficiency

The correction for acceptance and efficiency for light (anti)nuclei is necessary to account for the particles produced in the collisions that are undetected and untracked by the experimental apparatus.

From the simulation with (hyper)(nuclei)injection, the acceptance x efficiency ($A \times \epsilon$) for (anti)helium was estimated as the ratio between the reconstructed (anti)helium after the ITS+TPC(+TOF) reconstruction chain and the generated (anti)helium:

$$(A \times \epsilon)(^3\overline{\mathrm{He}}) = \frac{\text{number of reconstructed } ^3\overline{\mathrm{He}}}{\text{number of generated } ^3\overline{\mathrm{He}}}, \tag{5.9}$$

A selection for nuclei in the desired rapidity range $|y| < 0.5$ is applied both at the numerator and the denominator. The same method is used to estimate the efficiency for both the TPC analysis and the TPC+TOF analysis: in both cases, the reconstructed candidates are selected with the same track-quality criteria, including the same primary particle selections, as in data. For the TPC+TOF analysis, the selection includes a $5\sigma_{\mathrm{TPC}}$ selection and the requirement to have a hit in the TOF. The latter condition implies that the TPC-TOF matching efficiency is an ingredient entering in the final $A \times \epsilon$. The acceptance x efficiency is reported in Fig. 5.15 for both ^{3}He and $^3\overline{\mathrm{He}}$ and the two analyses.

The acceptance x efficiency plots show a *jumpy* behaviour. To limit this behaviour in the actual spectra correction, the efficiencies have been fit with a fit function

$$f = A \cdot \exp + B \cdot \mathrm{Pol1} + C \cdot 1/x. \tag{5.10}$$

The efficiencies used for correct the raw spectra are redefined taking the value of the fit function in a given p_{T} interval; the uncertainty on this value is taken from the efficiency obtained by the analysis task and used as the uncertainty of the refitted efficiency value. This technique smoothens the shape of the efficiency hence, the name of *efficiency smoothing*.

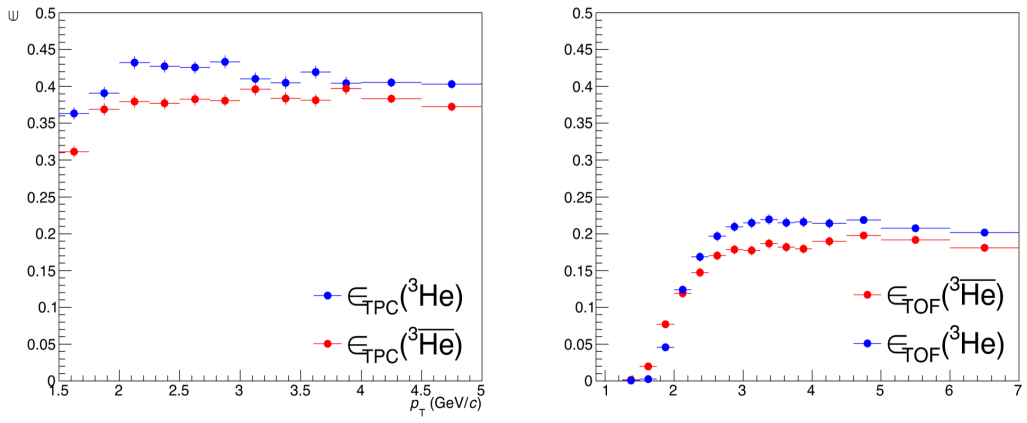

Figure 5.15: Acceptance x efficiency of ^{3}He (in blue) and $^3\overline{\mathrm{He}}$ (in red) for particle identified with TPC (left) and TPC+TOF (right) methods.

5.3.3 Primary helium fraction correction

The study of the production yield of (anti)helium in pp collisions is equivalent to the measurement of the yields of primary nuclei produced in the collision. At this purpose, the number of secondaries produced by other processes must be subtracted from the measured yield. As described in Section 5.1, secondary particles are mostly produced in the interaction of primary particles with the detector material via knock-out reactions and, due to the baryonic number conservation, only positive particles can be produced. Another origin of secondary helium is due to the hypertriton two-body weak decay:

$$^{3}_{\Lambda}\mathrm{H} \rightarrow ^{3}\mathrm{He} + \pi \tag{5.11}$$

The secondary helium contribution can be experimentally separated from that of primary nuclei using the distribution of the distance of closest approach of the tracks to the primary vertex of the collision in the transverse plance, DCA_{xy}. Primary helium nuclei are produced at the primary vertex, so they are expected to exhibit a peaked distribution centred at $\mathrm{DCA}_{xy} = 0$ cm. Secondary helium particles from material have a broader DCA_{xy} distribution, with a less pronounced peak centred at $\mathrm{DCA}_{xy} = 0$ cm.

To correct the measured ^{3}He yields for the primary fraction, a MC-based technique is used. A fit to the DCA_{xy} distribution is performed using histogram templates for the primary and the secondary helium. The primary DCA_{xy} template is obtained from a MC containing injected helium nuclei (LHC23j6c). The primary template consists in the DCA_{xy} distributions for the helium. The DCA_{xy} template for secondary helium nuclei from weak decay is obtained from the same MC used from the primary template. The distributions are scaled for the ratio between the measured hypertriton at $\sqrt{s} = 13.6$ TeV and the ^{3}He integrated yield measured at $\sqrt{s} = 13$ TeV [23]. As the yield dependence from the energy is at the TeV scale is mild, and the correction is small with respect to the knock-out contribution, this approximation is consistent. The measured yield for the hypertriton is obtained through private internal communication, as the measurement has not been published yet. Still, this choice is preferable to extrapolate the yield from different published analysis, as the available measurements are performed in different colliding system with severe difference in multiplicity with respect to this analysis. The distribution are scaled again for the branching ratio of the decay described in Eq. 5.11, that is 0.25 [131]. The scaling factor (w_{weak}) for the secondary nuclei from weak decay (w_{weak}) is then

$$w_{\mathrm{weak}} = \frac{\mathrm{d}N/\mathrm{d}y(^{3}_{\Lambda}H)}{\mathrm{d}N/\mathrm{d}y(^{3}\mathrm{He})} \times \mathrm{B.R.}(^{3}_{\Lambda}\mathrm{H} \rightarrow ^{3}\mathrm{He}\,\pi) \tag{5.12}$$

that, for pp collisions at $\sqrt{s} = 13.6$ TeV, is experimentally measured as

$$2.1 \times 10^{-9}/2.4 \times 10^{-7} \times 0.25 = 8.75 \times 10^{-3}\,.$$

The material DCA_{xy} template is obtained from two different GP MC datasets anchored to pp 13.6 TeV collisions in 2022 and 2023. The GP MC are used to avoid possible bias in the secondaries from material in (anti)nuclei-injected productions that could occur using MC with injection of (anti)nuclei. Since both GP MC have a low number of secondary (anti)helium, the use of different productions is needed to maximise the statistics. Moreover, the DCA_{xy} template chosen for the analysis is the DCA_{xy} distribution of secondary

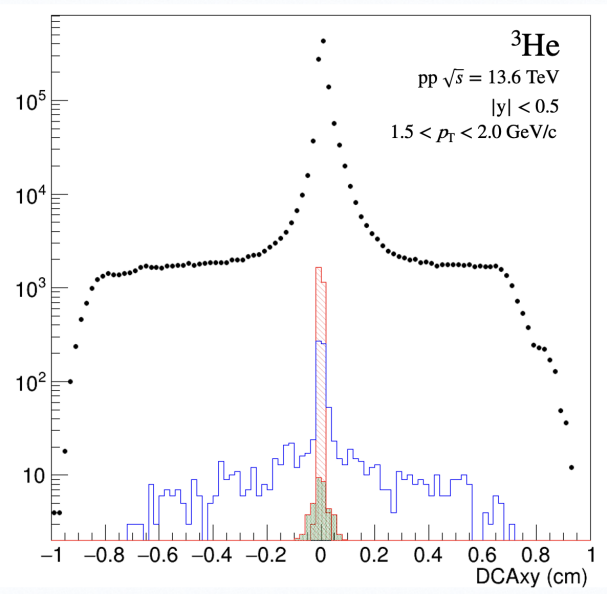

Figure 5.16: The DCA$_{xy}$ distribution of ^{3}He candidates in the p_{T} range (1.5, 2.0) GeV/c in data (black markers) is compared to the templates before the fit. The red and blue lines are the MC templates for primary and secondary nuclei from material, respectively. The green histogram is the template for secondaries from weak-decay. This is scaled by $w_{\mathrm{weak}} = 8.75 \times 10^{-3}$.

deuterons generated from knock-out, as the number of secondary helium candidates in the dataset used is still too low.

For all the templates, the PID is performed with a 5σ TPC selection, for both MC and data, for consistency. To have a pure set of templates, on the MC datasets the PID is performed requiring the PDG PID on the selected candidates. To estimate the primary fraction in the TPC+TOF spectra, additionally, one hit in the TOF is required.

As an example, the templates before the fit in the p_{T} range (1.5, 2.0) GeV/c are reported in Fig. 5.16.

The p_{T} bins used to extract the primary fraction are larger than the bins used in the analysis. This is necessary to maximise the statistics in every DCA$_{xy}$ bin value and minise the probability to have empty DCA$_{xy}$ bins, to prevent failures of the template fit.

The fit are performed in the (-0.5, 0.5) cm DCA$_{xy}$ range. In Fig. 5.17 the fit results for in the p_{T} range (1.5, 2.0) GeV/c is shown. Due to the low contribute of the weak-decay template (especially after the w_{weak} scaling), after the fit the weak-decay templates are negligible. For this reason, their contribution is removed from the estimation of the primary fraction estimate. This approximation could be discussed in a future iteration with a larger dataset.

The primary fraction is obtained by calculating the ratio between the fitted primary template and the sum of the fitted primary and secondary templates, then normalizing the ratio for the integral of the DCA$_{xy}$ distribution in the range of the DCA$_{xy}$ selection used for the analysis (which depends on the p_{T}, as shown in Tab. 5.1). The primary fraction

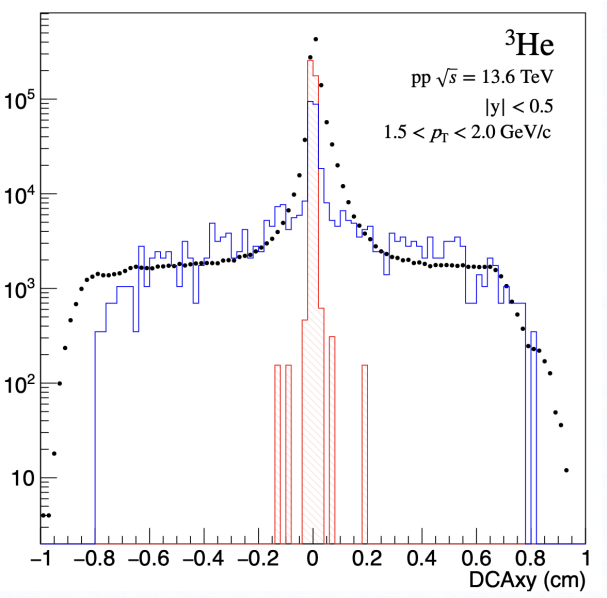

Figure 5.17: DCA$_{xy}$ distribution in the p_{T} range (1.5, 2.0) GeV/c, after the fit. The black markers are the data. The red line is fitted template for the primaries. The blue line the fitted template for secondaries from material. The weak-decay contributes are negligible and hence not plotted.

f_{prim} is espressed as

$$f_{prim} = \frac{\text{primaries}}{\text{primaries} + \text{secondaries}} \tag{5.13}$$

In the bins in which the fit failed for $p_{\mathrm{T}} > 4$ GeV/c due to low statistics (obtaining non-physical results as for instance a primary fraction greater than unity), the primary fractions has been set to 1. This choice is coherent with other analyses of (anti)nuclei in ALICE [23], as the secondary contamination for ^{3}He is expect to reach its maximum for $p_{\mathrm{T}}/z < 2$ GeV/c. The primary fractions estimated for TPC and TPC+TOF analyses as a function of p_{T}, reported in Fig. 5.18, are finally fitted with the function defined as

$$f_{prim}^{fit} = A \cdot \exp + B \cdot \mathrm{Pol1} + C \cdot 1/x \tag{5.14}$$

in order to estimate the primary fraction in the analysis bins, which are more granular. This correction is used in the analysis to correct the measured raw yield of the ^{3}He, while it is not used for $^3\overline{\mathrm{He}}$, as no secondary antiparticles are expected to be produced from material. As the (anti)hypertriton production is expected to be rare [66, 102, 132], the antihelium secondary contributions from weak decays are assumed negligible (a similar assumption was made in previous analyses [23]).

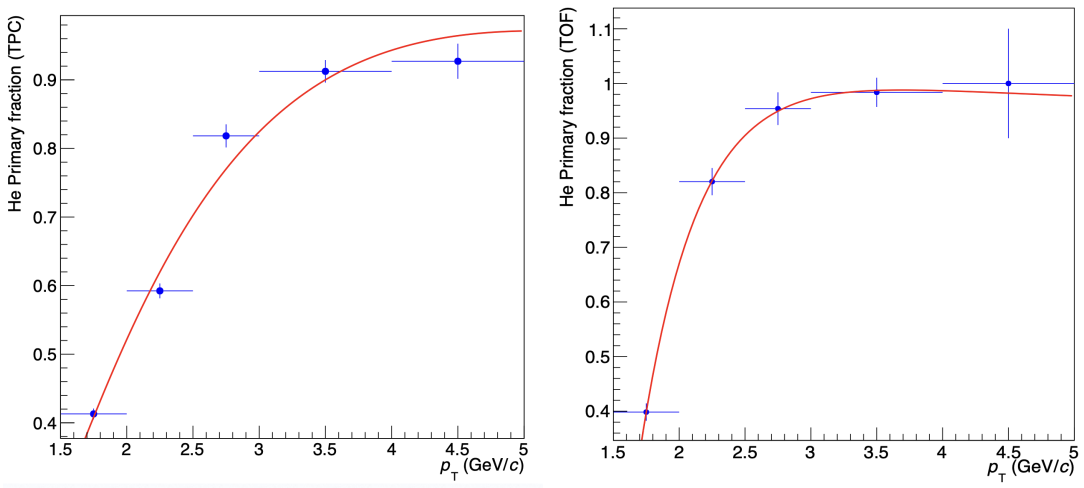

Figure 5.18: Primary fractions of the helium candidates as a function of p_{T} for the TPC (left) and TPC+TOF (right). The fractions are fit with the function defined in Eq. 5.14.

5.4 Systematic uncertainties

The possible sources of systematic uncertainties for the (anti)helium analysis can be classified on the basis of their origin. In Fig. 5.20, the different systematic uncertainties components are shown. The larger contribution is due to the track selection cuts.

One of the contribution to be considered is related to the selection of the event. Different limits for the vertex z position with respect to the nominal 10 cm cut have being considered, namely a stricter selection on $|V_z| < 8$ cm and a looser one on ($|V_z| < 12$ cm).

The largest contribution to the systematic uncertainties for both ^{3}He and $^3\overline{\mathrm{He}}$ is related to the track selection. The analysis is performed by varying the minimum number of findable clusters in the TPC from the default of 120 to 90 and 100, and the minimum number of ITS clusters from a defaults of 6 to 5 and 4. Another variation is performed requiring the tracks to be used in the reconstruction of the primary vertex (the so called `IsPVcontributor` cut). By varying the DCA selection using a fixed limit of $|\mathrm{DCA}_{xy}| < 0.08$ cm or 0.15 cm instead of a p_{T}-dependent selection, or using different fixed selection for DCA_z from the default $|\mathrm{DCA}_z| < 0.50$ cm to $|\mathrm{DCA}_z| < 1.20$ cm. Another contribution to the systematics can be found in the $\mathrm{N}^{\mathrm{TPC}}_{\sigma,i}$ preselection for the TPC+TOF PID analysis, varied from 5σ to 4σ and 3.5σ, which has effects on the measured TOF raw yield. These selections globally contribute to the uncertainty with an average value around 10% for $^3\overline{\mathrm{He}}$, as shown in Fig. 5.19, and an average value of approximately 15% for ^{3}He.

The choices made during the yield extraction procedure, such as extracting the raw signal in a certain $\mathrm{N}^{\mathrm{TPC}}_{\sigma,i}$ interval or the fit function used to extract a signal, are sources of additional systematic uncertainties. These have been accounted for, varying the $\mathrm{N}^{\mathrm{TPC}}_{\sigma,i}$ interval from a default of $5\mathrm{N}^{\mathrm{TPC}}_{\sigma,i}$ to 4 and 3.5. The background function for the TOF PID, instead, has been varied from a default Pol1 first polynomial function to a constant function Pol0 and to no background at all.

Additional systematics are inherited from previous Run 2 analyses. The uncertainty due

to the knowledge of the material budget of the detector, which affects the tracking efficiency, is inherited[3] from the measurement of (anti)helium in pp collisions at $\sqrt{s} = 13$ TeV [23]. There it was estimated with studies based on MC simulations of the interaction between the charged particles produced and the detector using `GEANT4`. This contribution consists of a 2% systematic uncertainty.

The contribution due to hadronic interaction cross section employed in the detector simulation is inherited and expected to be less than 2% for $^3\overline{\mathrm{He}}$ from a MC-based study [136].

All the contributions to the systematic uncertainties are tested using the Barlow criterion choosing a $1\sigma_{\mathrm{Barlow}}$ limit. The criterion is used to decide if a variation is significant or can be treated as a statistical fluctuation. The criterion uses the definition of the variable σ_{Barlow} as

$$\sigma_{\mathrm{Barlow}} = \sqrt{\delta^2_{centr} - \delta^2_{var}}\,, \tag{5.15}$$

where δ_{centr} is the default value and δ_{var} is the variation. A variation is considered in the systematic uncertainty evaluation only if

$$\Delta = \frac{N_{centr} - N_{var}}{\sigma_{\mathrm{Barlow}}} > 1\,.$$

The systematics uncertainties from variations of the selections are estimated, for all the p_{T} bins, as the semi-dispersions between default values and variations, for each considered case.

The fractional uncertainties that arise from all these variations are summarised for $^3\overline{\mathrm{He}}$ in pp 13.6 TeV collisions in Fig. 5.19 as a function of p_{T}. The total systematic uncertainties (red line in Fig. 5.20) are calculated summing in quadrature the contribution of each source and reach the value of 13% as a maximum for $^3\overline{\mathrm{He}}$. The green line in the same figure is the statistical uncertainty.

The systematic uncertainty is estimated in this work first for $^3\overline{\mathrm{He}}$. The relative systematic correction is then propagated to the ^{3}He spectra, adding up specific ^{3}He systematic corrections (like the systematic uncertainty due to the primary fraction estimation procedure). In the previous analysis in pp collisions at $\sqrt{s} = 13$ TeV, the systematic contribution for the primary fraction correction was included in the track selection and the systematic uncertainty for the track criteria variation was estimated up to a 15%. As this value is compatible with the total systematic uncertainties of this analysis (led by the track selection contribute), no additional contributes are added to the systematics.

[3]The replacement of ITS with ITS2 during the ALICE upgrade is expected to have reduced the material budget in front of the TPC; however, a precise assessment of the material budget requires a dedicated analysis [135], which is beyond the scope of this analysis and still ongoing within ALICE at the time of writing. Because of this, a conservative approach inheriting this source of systematic from previous analyses was chosen here.

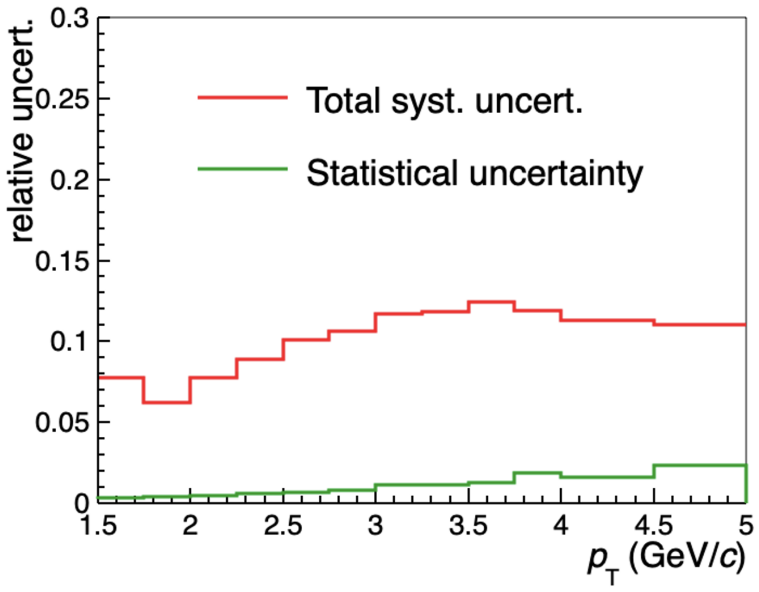

Figure 5.19: Fractional systematic uncertainties for the 13.6 TeV $^3\overline{\text{He}}$ analysis compared with the statistical uncertainties. Systematics are separated from statistical contributions via the Barlow test (selection at $1\sigma_{\text{Barlow}}$).

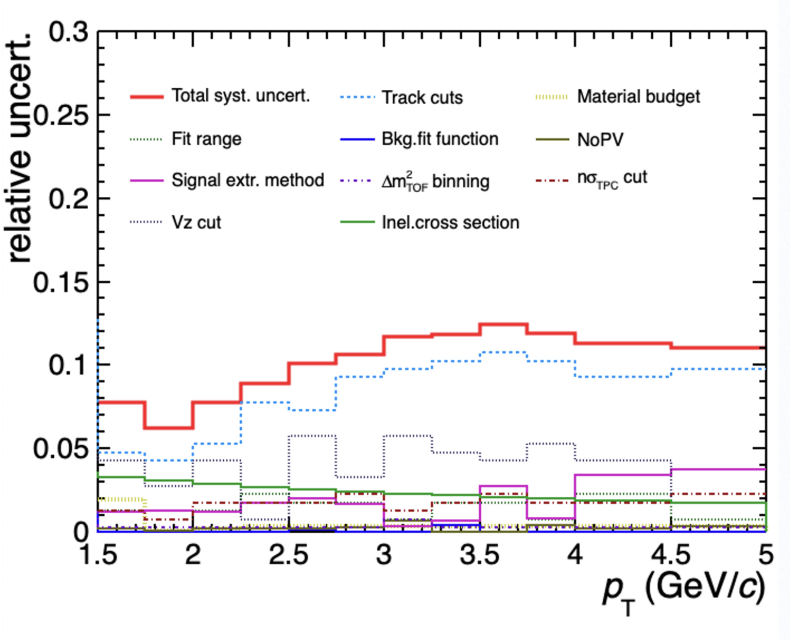

Figure 5.20: Fractional systematic uncertainties for the 13.6 TeV $^3\overline{\text{He}}$ analysis estimated from various sources are shown along with the total systematic uncertainty with a red line.

5.5 Production spectra

In this section, the results on the (anti)helium production in pp collisions at $\sqrt{s} = 13.6$ TeV are presented.

The p_{T} spectra of ^{3}He and $^3\overline{\mathrm{He}}$ are shown in Fig. 5.21, respectively in the upper and lower figure. The spectra are measured at midrapidity ($|y| < 0.5$) in the minimum bias pp collision data sample with the TPC and TPC+TOF analyses to provide a redundant, more solid measurement. This is the first measurement of (anti)helium production in pp collision at $\sqrt{s}$ =13.6 TeV by the ALICE Collaboration and the measurement at the highest collision energy so far. The previous high energy pp collision measurement was performed at $\sqrt{s}$ =13 TeV during the Run 2 data-taking campaign.
The production yields are normalised to the number of events, corrected for the acceptance, efficiency and feed-down contamination, as discussed in Chapter 5. The corrected yields are obtained as follows:

$$\frac{\mathrm{d}^2\mathrm{N}}{\mathrm{dp_T dy}} = \frac{1}{N_{ev}} \cdot \frac{\mathrm{d}^2\mathrm{N}}{\mathrm{dp_T dy}}\bigg|_{\mathrm{raw}} \times A \times \epsilon \times f_{prim} \tag{5.16}$$

The f_{prim} for $^3\overline{\mathrm{He}}$ is equal to unity for all the p_{T} bins as there are no contribution from spallation reactions from material for antinuclei.

The p_{T} spectra of $^3\overline{\mathrm{He}}$ and ^{3}He have also been compared, calculating the antimatter-over-matter ratio. In Fig. 5.22, in particular, the ratio using TPC (in blue markers) and TPC+TOF (in red markers) PID is shown. As discussed in Chapter 1, this ratio is expected to be compatible with unity, but in Fig. 5.22, a p_{T} dependent tension is observed for $p_{\mathrm{T}} < 2$ GeV/c, where the measured matter yield is higher than the antimatter. The reason behind these inconsistent values at low p_{T} is under investigation: one of the hypotheses is that with the employed reconstruction, the efficiency estimations performed in Chapter 5 did not account for all effects.

An additional comparison has been performed based on the ratio between the two particle identification techniques. In Fig. 5.23, the ratio between the p_{T}-spectra estimated using the TPC+TOF PID and the TPC-only PID is shown for both the ^{3}He (in blue) and the $^3\overline{\mathrm{He}}$ (in red).

For both species, a p_{T}-dependent tension is shown. For ^{3}He, the TPC+TOF analysis seems to overestimate the number of counts for $p_{\mathrm{T}} < 2$ GeV/c, while for higher p_{T} values, the ratio seems constant and is about 0.9. For $^3\overline{\mathrm{He}}$, the ratio is slightly higher and is about 0.95.

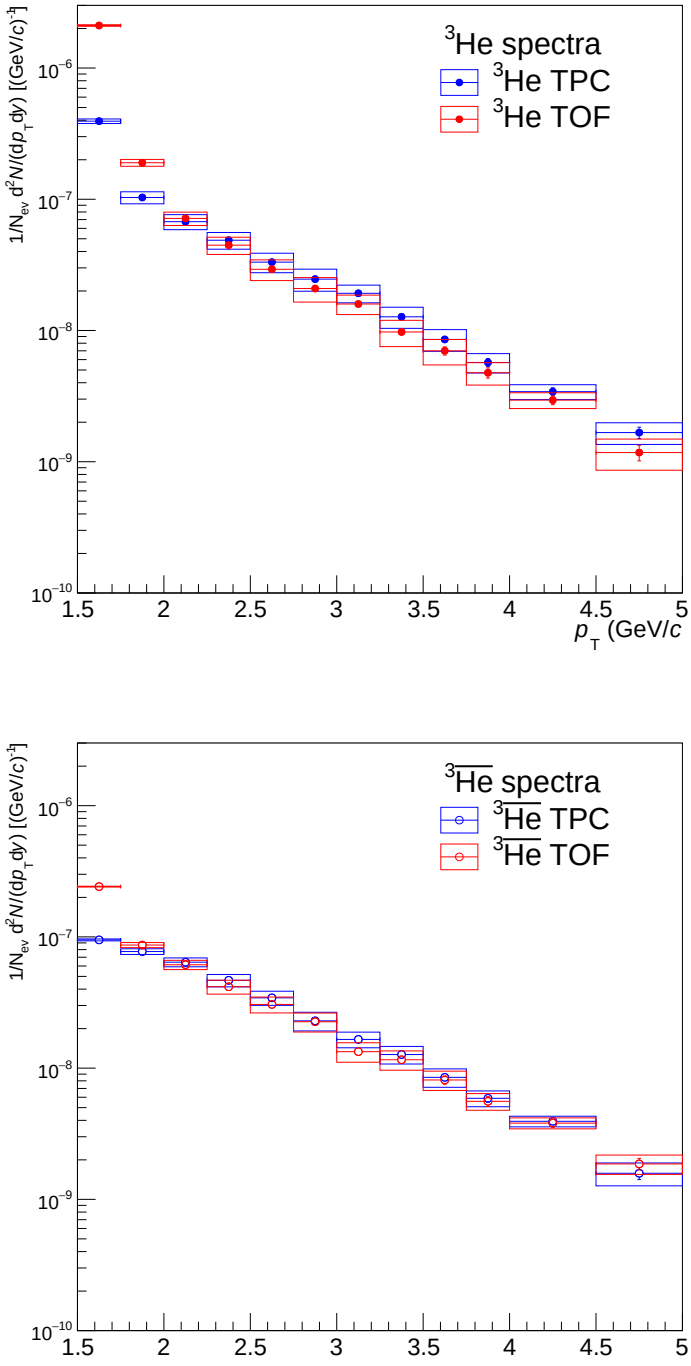

Figure 5.21: Spectra of ^{3}He (on the upper panel) and of $^3\overline{\text{He}}$ (on the lower panel) as measured in pp collisions at $\sqrt{s} = 13.6$ TeV in the p_{T} range (1.5 - 5) GeV/c. The spectra were measured using the TPC PID (in blue markers) and TPC+TOF PID (in red markers). This work.

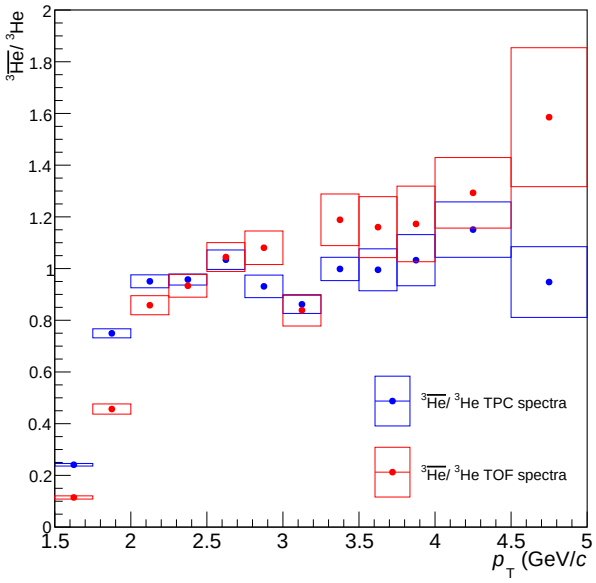

Figure 5.22: Antimatter-over-matter ratios as measured in pp collisions at $\sqrt{s}$ = 13.6 TeV in the p_T range (1.5 - 5) GeV/c. The ratios were measured using the TPC PID (in blue markers) and TPC+TOF PID (in red markers). This work.

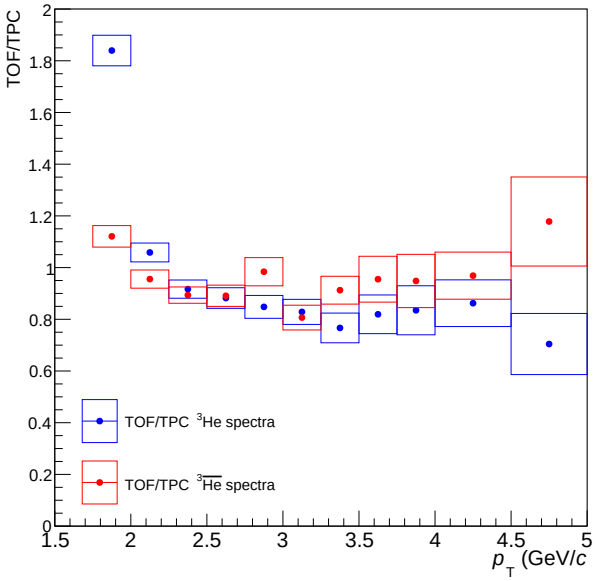

Figure 5.23: The TPC+TOF-to-TPC PID ratios as measured in pp collisions at $\sqrt{s}$ = 13.6 TeV in the p_T range (1.5 - 5) GeV/c. The ratios have been measured for the ^{3}He (in blue markers) and $^3\overline{\text{He}}$ (in red markers). This work.

5.6 Integral yield and ratios

In order to compute the p_{T}-integrated yields $\mathrm{d}N/\mathrm{d}y$ and the average transverse momentum $\langle p_{\mathrm{T}} \rangle$, the portion of the spectrum in the unmeasured p_{T} region cannot be neglected. Therefore, it is necessary to extrapolate the spectrum in the unmeasured p_{T} range. This is achieved by fitting the spectra with a Lévy-Tsallis [137] distribution expressed as

$$\frac{d^2N}{dy\,dp_T} = \frac{dN}{dy}\frac{p_T(n-1)(n-2)}{nC[nC+m(n-2)]}\left(1+\frac{m_T-m}{nC}\right)^{-n}, \tag{5.17}$$

where n, $\frac{\mathrm{d}N}{\mathrm{d}y}$ and C are the fit parameters, while m and m_T are respectively the mass and the transverse mass of the particle (e.g. the one of the helium). The Lévy-Tsallis function well describes the spectra of charged particle produced in pp collisions [138].
The first two measured points, covering the $p_{\mathrm{T}} = (1.5{-}2.0)$ GeV/c range, are not considered for the fit with the Lévy-Tsallis distribution and are dropped from the spectrum. This decision is due to the outlier nature of these points discussed previously in the antimatter-over-matter and TPC+TOF/TPC PID ratios (Fig. 5.22 and Fig. 5.23).

Due to the compatibility between the spectra obtained using the TPC and the TPC+TOF PID techniques in the $p_{\mathrm{T}} = (2.0 - 5.0)$ GeV/c range, as shown in Fig. 5.23, the final spectra for ^{3}He and $^3\overline{\mathrm{He}}$ are obtained as the weighted average of the two measurements. The averaging is carried out using the inverse of the squared uncertainties as weights, considering the statistical uncertainty as fully correlated. The extraction of the integrated quantities is then performed on the averaged results with the Lévy-Tsallis function.

The fit results for the ^{3}He and the $^3\overline{\mathrm{He}}$ spectra are shown in Fig. 5.24 and Fig. 5.25. The parameters extracted from the fit are reported on the legends in the figures. The same legends also report the fit χ^2/ndf.

The extracted yield, the $\langle p_{\mathrm{T}} \rangle$ and the percentage of yield extrapolated for $p_{\mathrm{T}} \leq 2$ GeV/c are summarised in Tab. 5.2. The values obtained for the sum of ^{3}He and $^3\overline{\mathrm{He}}$ in pp collisions at $\sqrt{s} = 13$ TeV [23] are also reported for comparison. The integrated values obtained with the current analysis are found to be compatible within 1σ with the 13 TeV published results.

Species	energy	$\langle \mathrm{d}N/\mathrm{d}y \rangle$	$\langle p_{\mathrm{T}} \rangle$	χ^2/ndf	Low p_{T} extr. fraction
^{3}He	13.6 TeV	$(2.98 \pm 0.28 \pm 0.75) \times 10^{-7}$	$1.30 \pm 0.04 \pm 0.21$	1.46/7	0.81 ± 0.31
$^3\overline{\mathrm{He}}$	13.6 TeV	$(2.79 \pm 0.25 \pm 0.54) \times 10^{-7}$	$1.28 \pm 0.04 \pm 0.21$	2.83/7	0.81 ± 0.23
$\frac{^3\mathrm{He}+^3\overline{\mathrm{He}}}{2}$	13 TeV	$(2.4 \pm 0.3 \pm 0.4) \times 10^{-7}$	-	-	-

Table 5.2: Values extracted from spectra fit with the Lévy-Tsallis function for both ^{3}He and $^3\overline{\mathrm{He}}$ on the weighted average obtained with the TPC and TPC+TOF analyses. The values of the integrated yield obtained at $\sqrt{s} = 13$ TeV for the sum of ^{3}He and $^3\overline{\mathrm{He}}$ are reported.

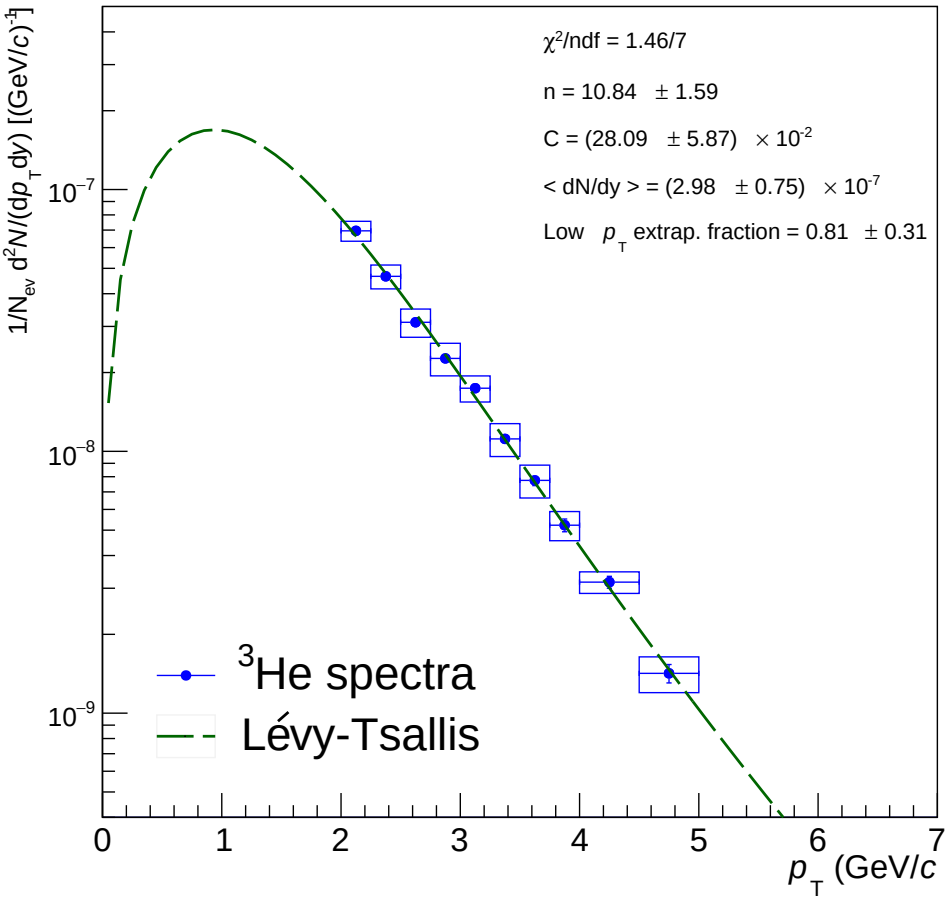

Figure 5.24: Spectra of ^{3}He produced in pp collisions at $\sqrt{s} = 13.6$ TeV, fitted with a Lévy-Tsallis function (in dashed green line). The parameters extracted from the fit and the χ^2/ndf are reported in the legend. This work.

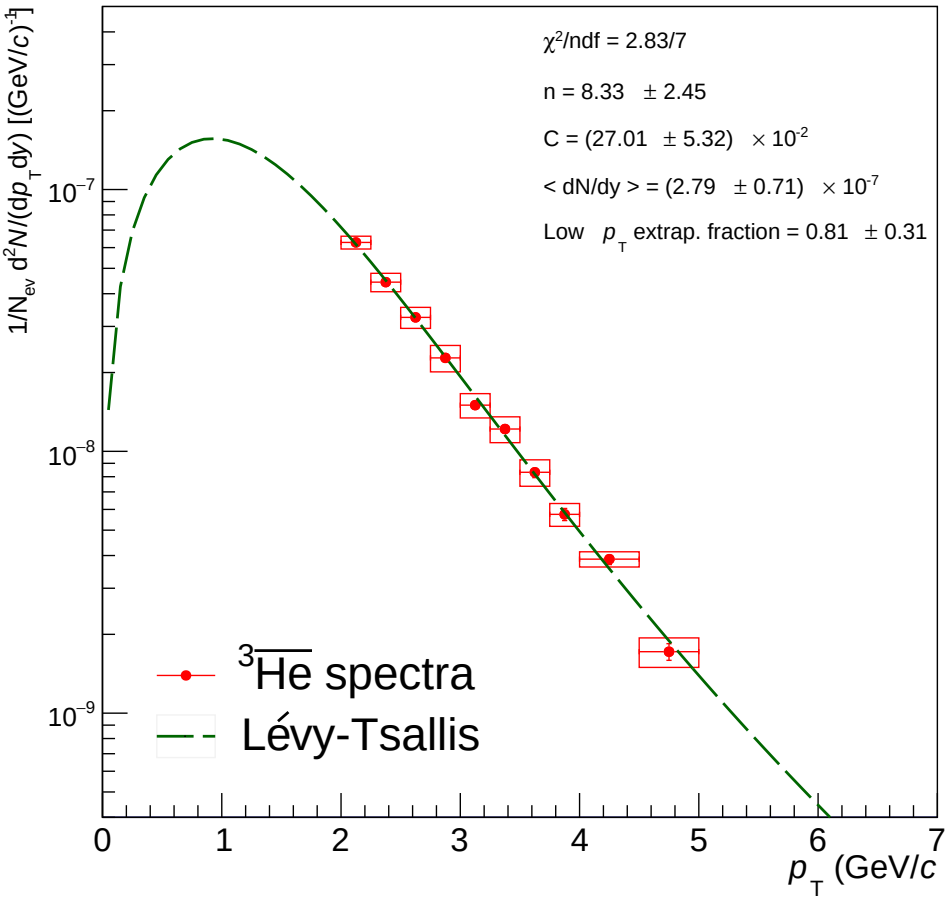

Figure 5.25: Spectra of $^3\overline{\mathrm{He}}$ produced in pp collisions at $\sqrt{s} = 13.6$ TeV, fitted with a Lévy-Tsallis function (in dashed green line). The parameters extracted from the fit and the χ^2/ndf are reported in the legend. This work.

It is important to note that the analysis of this thesis allowed us to discover some criticalities in the $\sqrt{s} = 13$ TeV published data on ^{3}He production spectra. It was found that the latter are overestimated due to the application of a wrong acceptance correction. Therefore, a reanalysis of the Run 2 data of pp collisions at $\sqrt{s} = 13$ TeV is used here for comparison. The comparison of the results obtained in $\sqrt{s} = 13.6$ TeV with the reanalysed Run 2 data is shown in Fig. 5.27 and Fig. 5.29. The ratios between the results of this analysis and the reanalysed Run 2 data are shown in Fig. 5.28 and Fig. 5.30. The error used for the ratio are the total errors (obtained summing in quadrature the statistical and systematic error), while the errors from the ratio are calculated assuming uncorrelated histograms.

The comparison also showcases the improvement of the ALICE performance after the LS2 upgrades. Due to the high statistics of the newer datasets, this preliminary analysis has a statistical uncertainty that is between 10 to 50 times smaller with respect to the previous measurements [23]. The comparison (for the $^3\overline{\text{He}}$ spectra) is shown in Fig. 5.26.

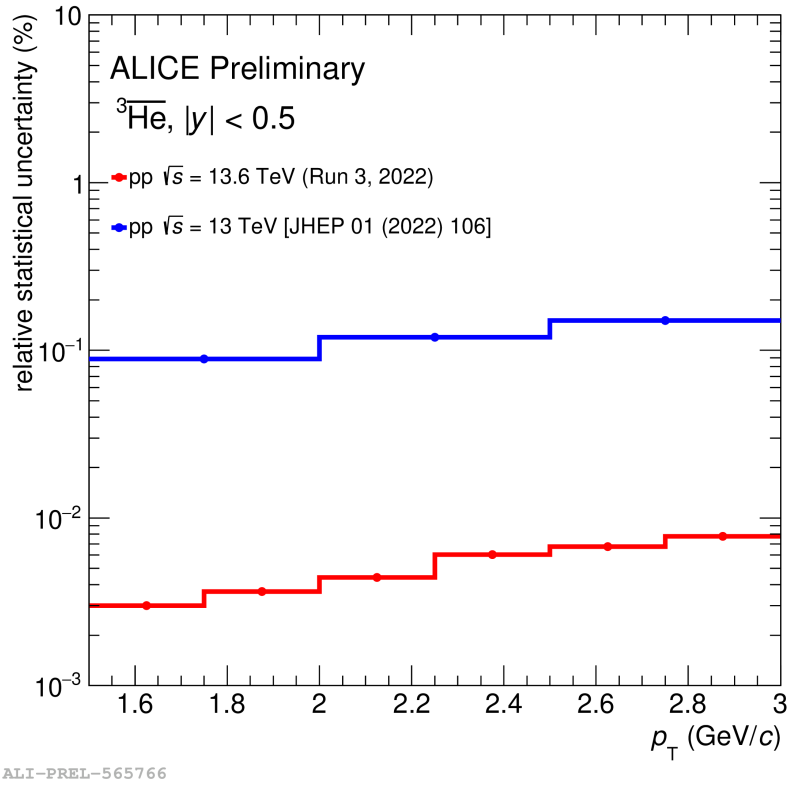

Figure 5.26: Relative statistical uncertainty in $^3\overline{\text{He}}$ produced in pp collisions at $\sqrt{s} = 13.6$ TeV in Run 2 (in blue) and in Run 3 (in red).

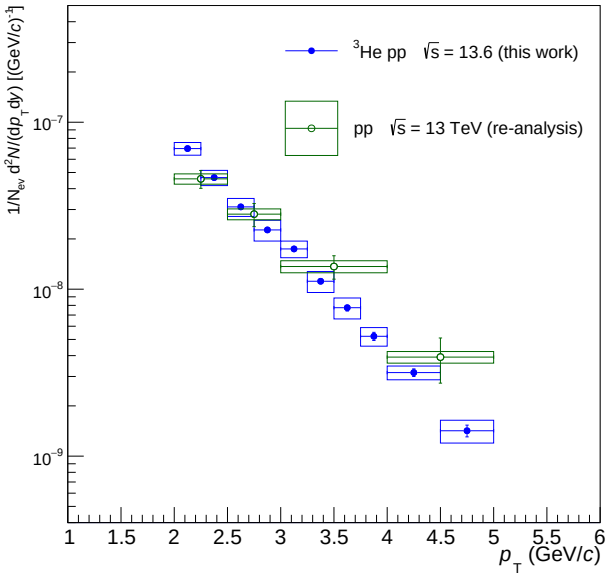

Figure 5.27: Comparison between the ^{3}He spectra produced in pp collisions at $\sqrt{s} = 13.6$ TeV (in blue) and the reanalysed helium spectra based on the published spectra (^{3}He +$^3\overline{\text{He}}$)/2 (in green). This work.

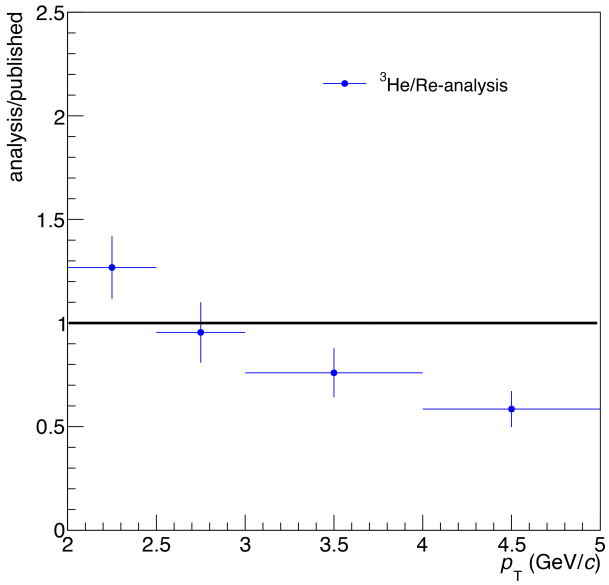

Figure 5.28: Ratio between the ^{3}He spectra (this work/reanalysed data).

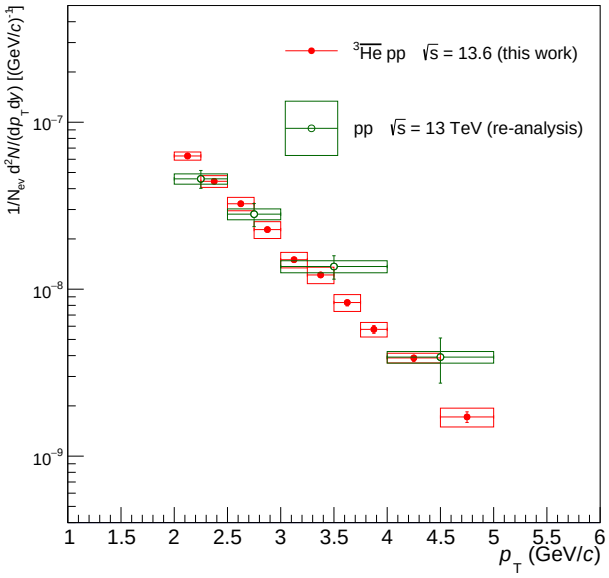

Figure 5.29: Comparison between the $^3\overline{\text{He}}$ spectra produced in pp collisions at $\sqrt{s}$ = 13.6 TeV (in red) and the reanalysed helium spectra based on the published spectra (^{3}He +$^3\overline{\text{He}}$)/2 (in green). This work.

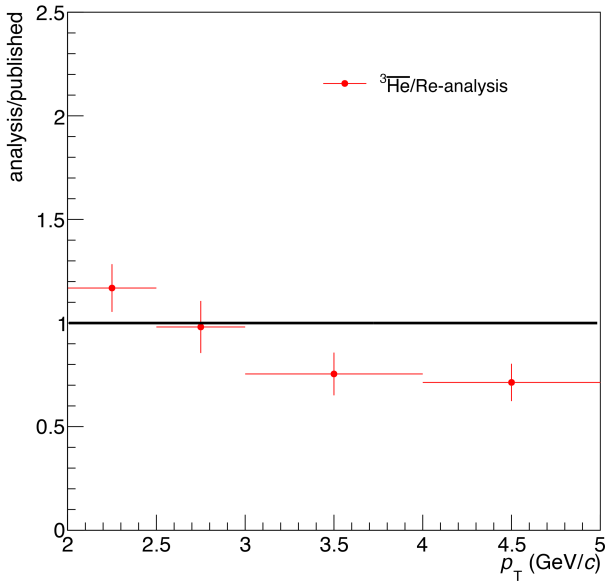

Figure 5.30: Ratio between the ^{3}He spectra (this work/reanalysed data).

5.7 Comparison to statistical hadronisation model predictions

The hadron abundances measured in relativistic high-energy collisions is described within the stastical hadronisation models (SHM). As discussed in Section 2.2, these models are based on the assumptions that particles are emitted from a chemically and thermally source at equilibrium. To predict the yields of hadrons produced in pp collisions, it is necessary to use a canonical statistical model (CSM) approach (see Section 2.2.2), which requires the exact conservation of baryon number, electric charge, and strangeness over a correlation volume V_c. The integrated yields measured in this analysis and the yield predicted by the Thermal-FIST package [90] are compared. By using the average charged particle multiplicity at midrapidity of the event sample, the chemical freeze-out temperature (T), the strangeness saturation parameter (γ_S), the system volume ($\mathrm{d}V/\mathrm{d}y$), and correlation volume (V_c) it is possible to estimate the yield for the ^{3}He (see Section 2.2.2). For extracting predictions for pp collisions at $\sqrt{s} = 13.6$ TeV, these parameters have been set to

$$T = 170.91 \text{ MeV} \quad ; \quad \gamma_S = 0.718 \quad ; \quad \mathrm{d}V/\mathrm{d}y = 16.992\,.$$

These values are obtained for a multiplicity $\mathrm{d}N_{\mathrm{ch}}/\mathrm{d}\eta = 7.08$ extrapolated from previous measurements at lower energies.

First, the correlation volume of the system is assumed to be equal to the system volume (V = V_c). The integrated primary yield of ^{3}He from the Thermal-FIST is $\mathrm{d}N/\mathrm{d}y$ (^{3}He) $= 2.763 \times 10^{-7}$. An error of the 10% is assumed for the sake of comparison with the measured yield. The estimation is then repeated assuming V = 1.6 V_c ($\mathrm{d}N/\mathrm{d}y$ (^{3}He) $= 9.16 \times 10^{-7}$) and V = 3 V_c ($\mathrm{d}N/\mathrm{d}y$ (^{3}He) $= 2.56 \times 10^{-6}$). The predictions with V = V_c shows a compatibility within 1 standard deviation (considering the combined uncertainty on the measurement and the prediction) for ^{3}He ($\sigma = 0.26$) and $^3\overline{\mathrm{He}}$ ($\sigma = 0.04$). The predictions with V = 1.6 V_c shows a discrepancy of 6 standard deviations for ^{3}He ($\sigma = 5.08$) and $^3\overline{\mathrm{He}}$ ($\sigma = 5.83$). The predictions with V = 3 V_c shows a compatibility discrepancy of 9 standard deviations for ^{3}He ($\sigma = 8.43$) and $^3\overline{\mathrm{He}}$ ($\sigma = 8.68$). Based on these considerations, the case where V = V_c is favoured by the data.

Chapter 6

Conclusions

This thesis presents the measurement of the (anti)helium yield at mid-rapidity in pp collisions at $\sqrt{s} = 13.6$ TeV with the ALICE detector. The analysis is performed on the complete 2022 pp collisions dataset. The measurement was performed using both the ALICE TPC and the TOF detectors. The (anti)nuclei PID was performed utilising both detectors to test the performance of the recently upgraded ALICE. This work is one of the first analyses performed after the beginning of the ALICE operations in the LHC Run 3.

The analysis is performed on a dataset selected to maximise the quality of the tracks and applying kinematic selection to improve the purity of the sample and to reduce the number of secondary particles. The main challenge is accounting for the detector and reconstruction effects by applying ad hoc recalibration procedures for the (anti)helium analysis. These efforts were needed to compensate for a p_{T}-shift effect between the transverse momentum generated in the simulated dataset and the one reconstructed in the data, and to recalibrate the response of the TPC detector to ensure that the species selected are coherent with the data measured.

To take account of the detector efficiency and the acceptance, a dataset of simulated MC data is used to extract the acceptance x efficiency vs p_{T} and eventually to correct the yields. An additional correction is needed for the ^{3}He yield, as a residual number of positive secondary particles. For this purpose, a primary fraction correction is applied. The systematic uncertainties study on the yields show that the major contributions are due to the track selections and the primary fraction correction. The systematic uncertainties estimated in this analysis are compatible with systematic uncertainties measured with the Run 2 data. It is noteworthy to observe the major improvement of Run 3 in the order of statistical uncertainties, which is 10 to 50 smaller with respect to Run 2, allowing for higher precision. The spectra obtained with the TPC and TPC+TOF PID techniques are consistent. For this reason, they are then combined, obtaining a single ^{3}He spectra and a single $^3\overline{\mathrm{He}}$ spectra. As a result, the (anti)helium-3 yields as a function of p_{T} is measured in the $p_{\mathrm{T}} = (2.0 - 5.0)$ GeV/c range. The combination allows for a further reduction of systematic uncertainties towards higher precision.

These spectra can be compared with those predicted by the theoretical models and previous ALICE measurements performed at lower energies. The spectra estimated in this analysis show a higher granularity with respect to the published spectra. The comparison with the published $\sqrt{s} = 13$ TeV data shows compatibility within 2σ for $p_{\mathrm{T}} < 4$ GeV/c.

The spectra are fitted with the Lévy-Tsallis function to determine the integrated yield in the whole p_{T} range. Compared to the integrated yields at $\sqrt{s} = 13.6$ TeV, both the ^{3}He and the $^3\overline{\mathrm{He}}$ are compatible within 1 standard deviation. The ratio of the two spectra is compatible (within the uncertainties) with unity. The results are here reported: dN/dy (^{3}He) $= (2.98 \pm 0.28 \pm 0.75) \times 10^{-7}$, dN/dy ($^3\overline{\mathrm{He}}$) $= (2.79 \pm 0.25 \pm 0.54) \times 10^{-7}$.

These results set the foundation for a more detailed study of (anti)helium-3 production at this energy. The sample used for this analysis corresponds to an integrated luminosity of 19 pb^{-1}, which represents about 10% of the target luminosity for Run 3 and 4. Additional $L = 56$ pb^{-1} have been collected in 2023 and 2024. This means that by extending this preliminary analysis to the latest data samples, the production of ^{3}He ($^3\overline{\mathrm{He}}$) can be characterised in a multi-differential way with measurements of multiplicity and rapidity dependence. Prior to this, it will be crucial to repeat the current analysis employing an improved reconstruction and calibration of the ALICE data, to which this work contributed. In particular, aspects such as an analysis of the effect of the particle hypothesis employed in tracking and a better characterisation of the contribution from secondary nuclei will be crucial to improve the precision of the measurement even further. Despite room for improvement in this preliminary measurement, these results successfully tested the performance of the upgraded ALICE apparatus and proved useful in spotting some criticalities in previous (anti)helium analyses. Next, the results on ^{3}He production spectra can be used to constrain formation models such as statistical hadronisation through the extraction of ^{3}He/p ratio and coalescence models by extracting B_3 parameter. In the longer term, this result and its natural extensions will contribute to clarifying the formation mechanisms of light antinuclei, with a potential application as input to the modelling for the production of cosmic antinuclei for indirect dark matter searches.

Appendix A

Datasets used in the analysis

Data This is the list of the pp collisions at $\sqrt{s}$ =13.6 TeV collected in 2022 that were used in this analysis. The data have a 500 kHz IR and a pile-up factor $\mu < 0.1$. The run number list follows for each period.

LHC22m apass4:
523142, 523148, 523182, 523186, 523298, 523306, 523308, 523309, 523397, 523399, 523401, 523441, 523541, 523559, 523669, 523671, 523677, 523728, 523731, 523779, 523783, 523786, 523788, 523789, 523792, 523797, 523821

LHC22o-test apass4:
527690, 527694, 527731, 527734, 527736

LHC22o apass4:
526463, 526465, 526466, 526467, 526468, 526486, 526505, 526512, 526525, 526526, 526528, 526559, 526596, 526606, 526612, 526639, 526641, 526647, 526649, 526713, 526714, 526715, 526716, 526719, 526720, 526776, 526886, 526938, 526963, 526964, 526966, 526967, 526968, 527015, 527016, 527028, 527031, 527033, 527034, 527038, 527039, 527041, 527057, 527076, 527109, 527237, 527240, 527259, 527260, 527261, 527262, 527349, 527446, 527518, 527523, 527821, 527825, 527826, 527828, 527848, 527850, 527852, 527863, 527864, 527865, 527869, 527871, 527895, 527898, 527899, 527902, 527963, 527976, 527978, 527979, 528021, 528026, 528036, 528094, 528097, 528105, 528107, 528109, 528110, 528231, 528232, 528233, 528263, 528266, 528292, 528294, 528316, 528319, 528328, 528329, 528330, 528332, 528336, 528347, 528359, 528379, 528381, 528386, 528448, 528451, 528461, 528463, 528530, 528531, 528534, 528537, 528543

LHC22p apass4:
528602, 528604, 528617, 528781, 528782, 528783, 528784, 528798, 528801

LHC22q apass4:
528991, 528997, 529003, 529005, 529006, 529009, 529015, 529035, 529037, 529038, 529039, 529043

LHC22r apass4:
529077, 529078, 529084, 529088, 529115, 529116, 529117, 529128, 529208, 529209, 529210, 529211, 529237, 529242, 529248, 529252, 529270, 529306, 529317, 529320, 529324, 529338, 529341

LHC22t apass4:
529450, 529452, 529454, 529458, 529460, 529461, 529462, 529542, 529552, 529554, 529662, 529663, 529664, 529674, 529675, 529690, 529691

MC The simulated MC dataset used for this analysis.

LHC23f4b2 (JIRA-O2-3876), a General Purpose (GP) MC anchored to apass4 of 13.6 TeV pp data at 500 kHz, without distortions and ITS/MFT ideal alignments. The number of generated events is 21.5 $\cdot 10^6$.

LHC23f4b2:
526463, 526465, 526467, 526486, 526505, 526512, 526525, 526526, 526528, 526559, 526596, 526606, 526612, 526639, 526641, 526647, 526649, 526713, 526719, 526776, 526886, 526938, 526964, 526967, 526968, 527016, 527028, 527034, 527038, 527039, 527041, 527057, 527076, 527109, 527237, 527240, 527260, 527446, 527518, 527523, 527821, 527825, 527826, 527828, 527848, 527850, 527852, 527863, 527864, 527865, 527869, 527871, 527895, 527898, 527899, 527902, 527976, 527978, 527979, 528021, 528026, 528036, 528105, 528107, 528109, 528110, 528232, 528233, 528263, 528266, 528292, 528294, 528316, 528319, 528328, 528329, 528332, 528336, 528347, 528359, 528379, 528381, 528386, 528448, 528451, 528461, 528463, 528531, 528534, 528537, 528543

LHC23k4f (JIRA-O2-4559), a General Purpose (GP) MC anchored to apass4 of 13.6 TeV pp data at 500 kHz collected in 2023. The number of generated events is 413.2 $\cdot 10^6$.

LHC23k4f:
535069, 535084, 535085, 535087, 535345, 535365, 535475, 535476, 535478, 535479, 535480, 535514, 535517, 535525, 535526, 535545, 535563, 535566, 535613, 535621, 535623, 535624, 535627, 535644, 535645, 535711, 535716, 535721, 535722, 535725, 535941, 535964, 535966, 535983, 535999, 536020, 536025, 536055, 536106, 536108, 536176, 536199, 536235, 536236, 536237, 536238, 536239, 536255, 536257, 536261, 536262, 536338, 536339, 536340, 536343, 536344, 536346, 536370, 536401, 536402, 536403, 536416, 536487, 536488, 536489, 536490, 536545, 536547, 536548, 536606, 536607, 536608, 536609, 536610, 536611, 536612, 536613, 536663, 536683, 536685, 536757, 536762, 536774, 536790, 536822, 536839, 536842, 536843, 536848, 536898, 536899, 536906, 536908, 536957, 536968, 536969, 536971, 537274, 537276, 537397, 537401, 537411, 537425, 537426, 537447, 537448, 537449, 537464, 537465, 537466, 537480, 537504, 537505, 537509, 537511, 537531, 537546, 537547, 537549, 537551, 537553, 537594, 537602, 537605, 537622, 537623, 537632, 537636, 537645, 537658, 537659, 537660, 537661, 537663, 537734, 537736, 537737, 537739, 537740, 537769, 537770, 537812, 537822, 537825, 537826, 537827, 537829, 537836, 537853, 537855, 537861, 537864, 537865, 537867,

537870, 537893, 537897, 537899, 537900, 537901, 537903, 537912, 537959, 537960, 537963, 537965, 538018, 538923, 538931, 538932, 538933, 538956, 538958, 538960, 538961, 538964, 538966, 538967, 538968, 538970, 539008, 539058, 539071, 539086, 539087, 539088, 539089, 539107, 539108, 539129, 539130, 539132, 539133, 539218, 539219, 539220, 539221, 539222, 539226, 539227, 539267, 539268, 539269, 539270, 539271, 539272, 539273, 539314, 539315, 539316, 539317, 539331, 539332, 539333, 539339, 539443, 539444, 539445, 539466, 539480, 539481, 539482, 539483, 539501, 539517, 539531, 539556, 539557, 539580, 539622, 539623, 539636, 539637, 539638, 539644, 539646, 539647, 539649, 539700, 539873, 539874, 539875, 539876, 539877, 539882, 539883, 539884, 539906, 539908

LHC23j6c (JIRA-O2-4200), a MC with injected (hyper)(anti)nuclei anchored to apass4 of 13.6 TeV pp data. The number of generated events is 19.4 $\cdot 10^6$.

LHC23j6c:
523182, 523186, 526463, 526465, 526466, 526467, 526468, 526486, 526505, 526525, 526526, 526528, 529077, 529078, 529084, 529088, 529450, 529452, 529454, 529458

Appendix B

Signal extraction

In this appendix all the fits used to extract the raw yield of the ^{3}He and the $^3\overline{\text{He}}$ are shown. The $\text{N}_\sigma^{\text{TPC}}$ and Δm^2_{TOF} distributions projected in bins of p_{T} are presented in this order.

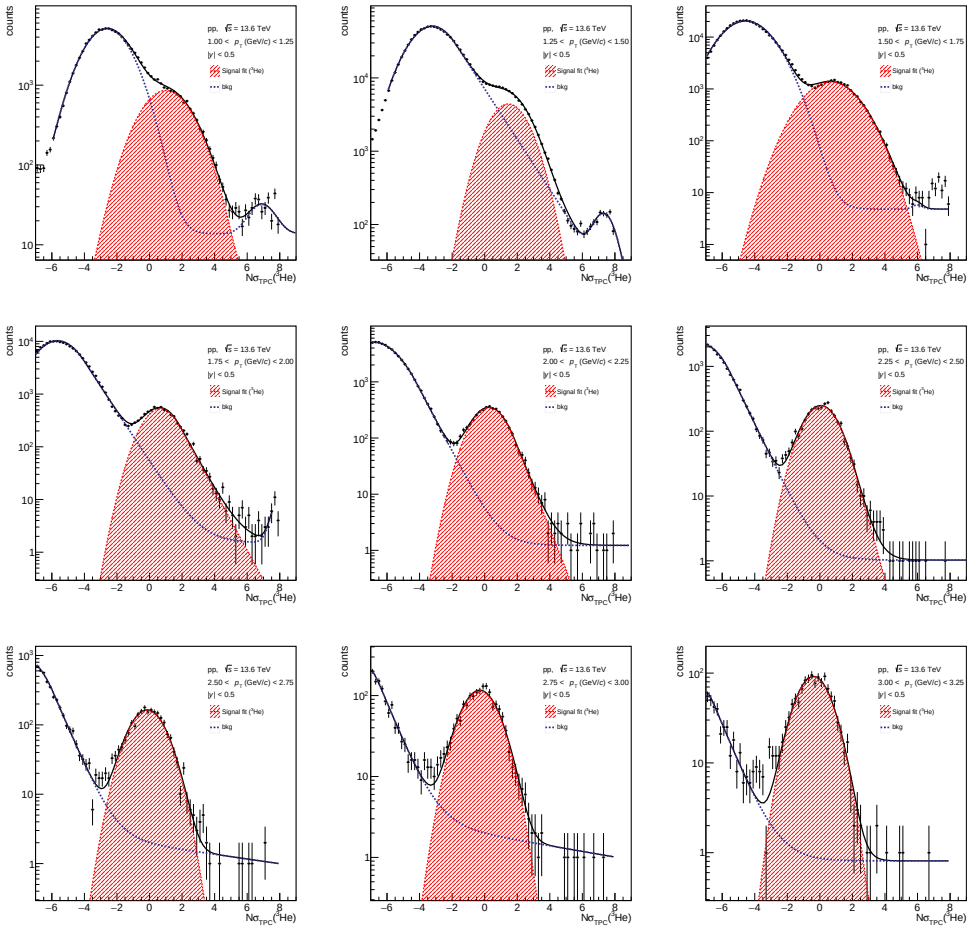

Figure B.1: ^{3}He signal from TPC-nσ distribution in pp collisions at $\sqrt{s}$ = 13.6 TeV is fitted with the global function which is shown in the blue black line. The data points are marked with black circles. The red line represents the signal and the blue line represents the background.

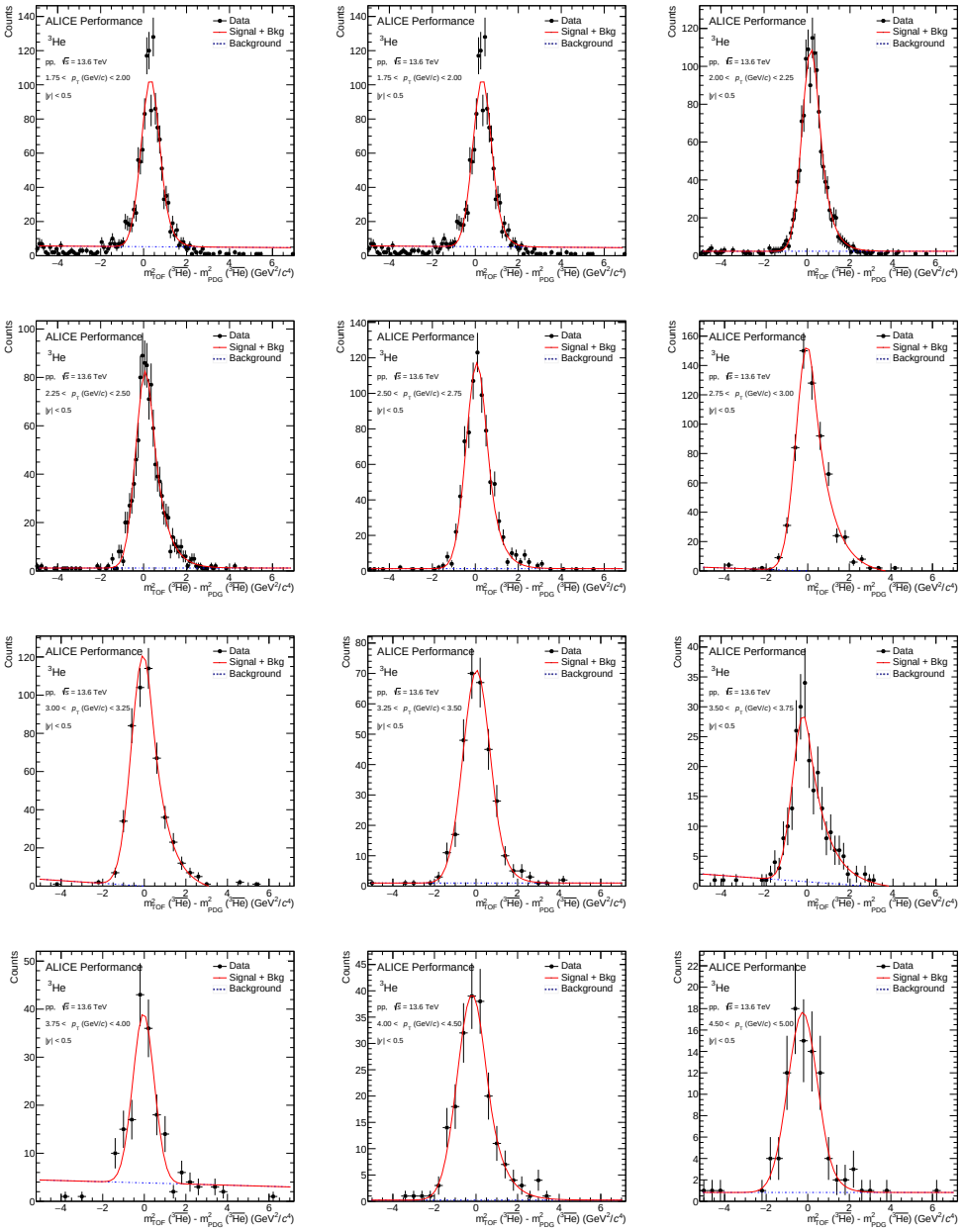

Figure B.2: ^{3}He signal from $\Delta m^2_{\mathrm{TOF}}$ distribution in pp collisions at $\sqrt{s} = 13.6$ TeV. The data points are marked with black circles. The red line represents the signal and the blue line represents the background.

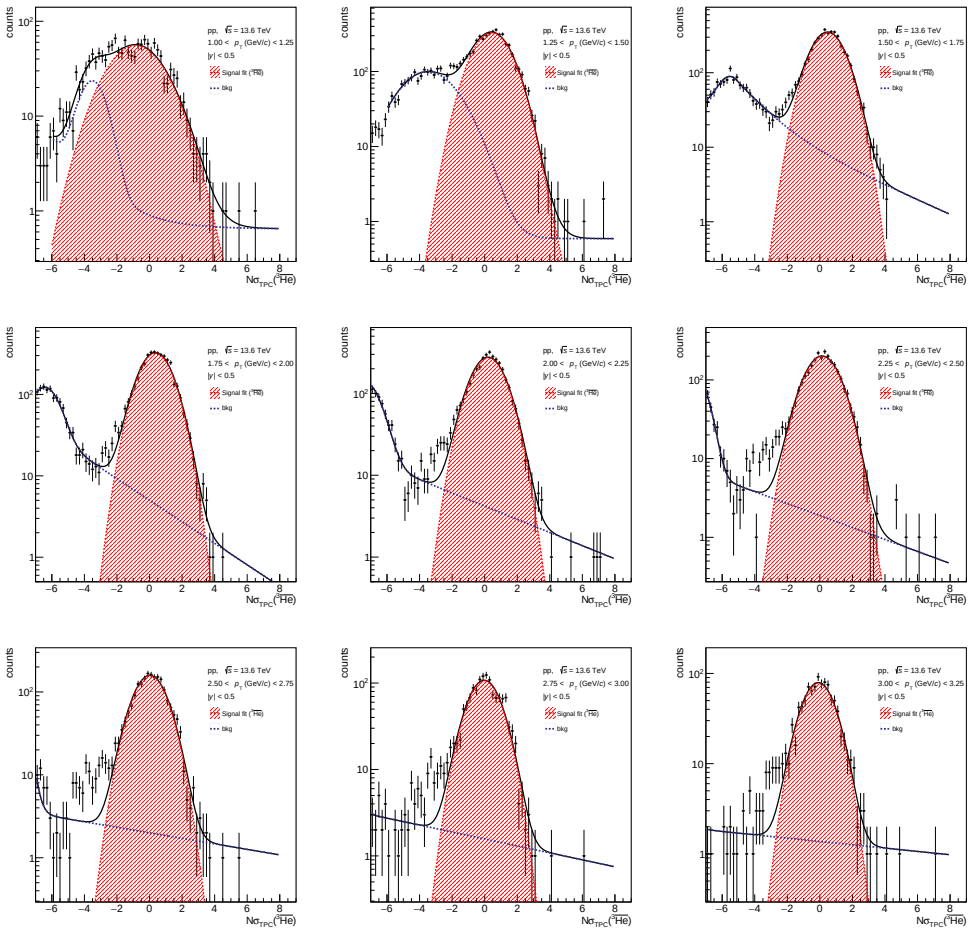

Figure B.3: $^3\overline{\text{He}}$ signal from TPC-nσ distribution in pp collisions at $\sqrt{s} = 13.6$ TeV is fitted with the global function which is shown in the blue black line. The data points are marked with black circles. The red line represents the signal and the blue line represents the background.

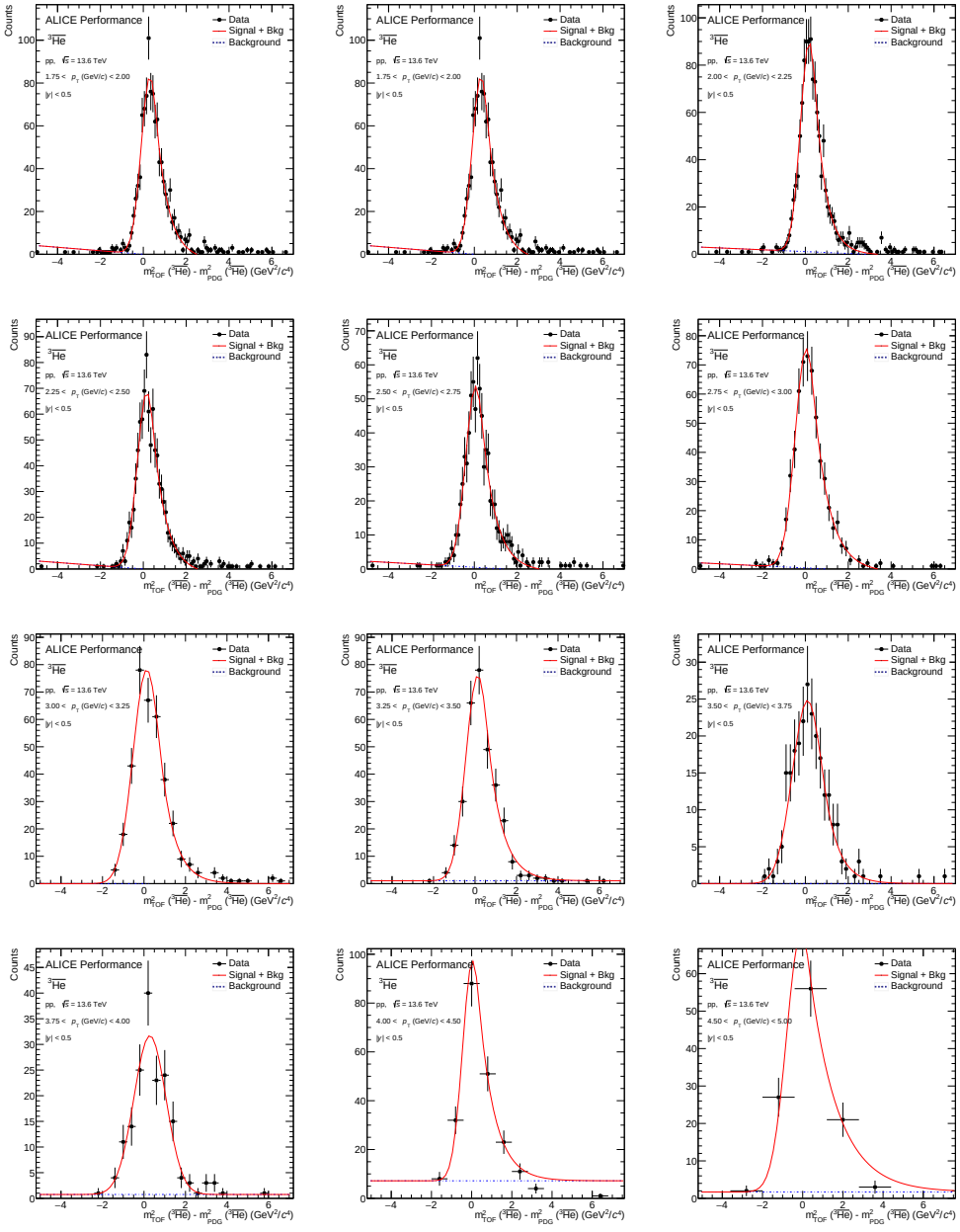

Figure B.4: $^3\overline{\mathrm{He}}$ signal from $\Delta m^2_{\mathrm{TOF}}$ distribution in pp collisions at $\sqrt{s} = 13.6$ TeV. The red line represents the signal and the blue line represents the background.

Bibliography

[1] A. Schuster, "Potential matter.—a holiday dream", Aug., 1898. https://doi.org/10.1038/058367a0.

[2] P. A. M. Dirac, "The quantum theory of the electron", *Proc. Roy. Soc. Lond. A* **117** (1928) 610–624.

[3] M. Thomson, *Modern Particle Physics*. Cambridge University Press, 2013.

[4] C. D. Anderson, "The Positive Electron", *Phys. Rev.* **43** (Mar, 1933) 491–494. https://link.aps.org/doi/10.1103/PhysRev.43.491.

[5] O. Chamberlain, E. Segrè, C. Wiegand, and T. Ypsilantis, "Observation of Antiprotons", *Phys. Rev.* **100** (Nov, 1955) 947–950. https://link.aps.org/doi/10.1103/PhysRev.100.947.

[6] **Particle Data Group** Collaboration, P. Zyla *et al.*, "Review of Particle Physics", *Progress of Theoretical and Experimental Physics* **2020** no. 8, (08, 2020) , https://academic.oup.com/ptep/article-pdf/2020/8/083C01/34673722/ptaa104.pdf. https://doi.org/10.1093/ptep/ptaa104. 083C01.

[7] D. E. Dorfan, J. Eades, L. M. Lederman, W. Lee, and C. C. Ting, "Search for Massive Particle", *Phys. Rev. Lett.* **14** (Jun, 1965) 999–1003. https://link.aps.org/doi/10.1103/PhysRevLett.14.999.

[8] D. E. Dorfan, J. Eades, L. M. Lederman, W. Lee, and C. C. Ting, "Observation of Antideuterons", *Phys. Rev. Lett.* **14** (Jun, 1965) 1003–1006. https://link.aps.org/doi/10.1103/PhysRevLett.14.1003.

[9] Y. Antipov *et al.*, "Observation of antihelium-3", *Nuclear Physics B* **31** no. 2, (1971) 235–252. https://www.sciencedirect.com/science/article/pii/0550321371902288.

[10] N. K. Vishnevsky *et al.*, "Observation of antitritium", *Yad. Fiz.* **20** (1974) 694–708.

[11] R. L. Golden, S. Horan, B. G. Mauger, G. D. Badhwar, J. L. Lacy, S. A. Stephens, R. R. Daniel, and J. E. Zipse, "Evidence for the Existence of Cosmic-Ray Antiprotons", *Phys. Rev. Lett.* **43** (Oct, 1979) 1196–1199. https://link.aps.org/doi/10.1103/PhysRevLett.43.1196.

[12] V. I. Kolesnikov, "Anti-nuclei and nuclei production in pb+pb collisions at cern sps energies", *Journal of Physics: Conference Series* **110** no. 3, (May, 2008) 032010. http://dx.doi.org/10.1088/1742-6596/110/3/032010.

[13] M. Harrison, T. Ludlam, and S. Ozaki, "RHIC project overview, journal = Nuclear Instruments and Methods in Physics Research Section A: Accelerators, Spectrometers, Detectors and Associated Equipment",. https://www.sciencedirect.com/science/article/pii/S016890020201937X.

The Relativistic Heavy Ion Collider Project: RHIC and its Detectors.

[14] **STAR** Collaboration, J. Adams *et al.*, "Experimental and theoretical challenges in the search for the quark gluon plasma: The STAR Collaboration's critical assessment of the evidence from RHIC collisions", *Nucl. Phys. A* **757** (2005) 102–183, arXiv:nucl-ex/0501009.

[15] **PHENIX** Collaboration, K. Adcox *et al.*, "Formation of dense partonic matter in relativistic nucleus-nucleus collisions at RHIC: Experimental evaluation by the PHENIX collaboration", *Nucl. Phys. A* **757** (2005) 184–283, arXiv:nucl-ex/0410003.

[16] **STAR** Collaboration, C. Adler *et al.*, "$\overline{\mathrm{d}}$ and $^3\overline{\mathrm{He}}$ Production in $\sqrt{s_{\mathrm{NN}}} = 130$ GeV Au+Au collisions", *Phys. Rev. Lett.* **87** (2001) 262301, arXiv:nucl-ex/0108022. [Erratum: Phys.Rev.Lett. 87, 279902 (2001)].

[17] **STAR** Collaboration, H. Agakishiev *et al.*, "Observation of the antimatter helium-4 nucleus", *Nature* **473** (2011) 353, arXiv:1103.3312 [nucl-ex]. [Erratum: Nature 475, 412 (2011)].

[18] B. Alper *et al.*, "Large angle production of stable particles heavier than the proton and a search for quarks at the CERN intersecting storage rings", *Physics Letters B* **46** no. 2, (1973) 265–268. https://www.sciencedirect.com/science/article/pii/0370269373907004.

[19] **British-Scandinavian-MIT Collaboration** Collaboration, W. M. Gibson *et al.*, "Production of deuterons and antideuterons in proton-proton collisions at the CERN ISR", *Lettere al Nuovo Cimento (1971-1985)* **21** no. 6, (1978) 189–194. https://doi.org/10.1007/BF02822248.

[20] **ALICE** Collaboration, S. Acharya *et al.*, "Production of deuterons, tritons, ^{3}He nuclei, and their antinuclei in ppcollisions at $\sqrt{s} = 0.9$, 2.76, and 7 TeV", *Phys. Rev. C* **97** (Feb, 2018) 024615. https://link.aps.org/doi/10.1103/PhysRevC.97.024615.

[21] **ALICE** Collaboration, E. Abbas *et al.*, "Mid-rapidity anti-baryon to baryon ratios in pp collisions at $\sqrt{s} = 0.9,\ 2.76$ and 7 TeV measured by alice", *The European Physical Journal C* **73** no. 7, (July, 2013) 2496. http://dx.doi.org/10.1140/epjc/s10052-013-2496-5.

[22] **ALICE** Collaboration, S. Acharya *et al.*, "Measurements of chemical potentials in Pb–Pb collisions at $\sqrt{s_{\mathrm{NN}}} = 5.02$ TeV", arXiv:2311.13332 [nucl-ex].

[23] **ALICE** Collaboration, S. Acharya *et al.*, "Production of light (anti)nuclei in pp collisions at $\sqrt{s} = 13$ TeV", *Journal of High Energy Physics* **106** (Jan, 2022) 1029–8479. https://doi.org/10.1007/JHEP01(2022)106.

[24] **ALICE Collaboration** Collaboration, S. Acharya *et al.*, "Measurement of the production and elliptic flow of (anti)nuclei in Xe-Xe collisions at $\sqrt{s_{\mathrm{NN}}} = 5.44$ TeV", *Phys. Rev. C* **110** (Dec, 2024) 064901. https://link.aps.org/doi/10.1103/PhysRevC.110.064901.

[25] **Particle Data Group** Collaboration, S. Navas *et al.*, "Review of particle physics", *Phys. Rev. D* **110** no. 3, (2024) 030001.

[26] A. H. G. Peter, "Dark Matter: A Brief Review", 2012.

[27] S. Hannestad, A. Mirizzi, G. G. Raffelt, and Y. Y. Y. Wong, "Neutrino and axion hot dark matter bounds after WMAP-7", *Journal of Cosmology and Astroparticle Physics* **2010** no. 08, (Aug, 2010) 001.

https://dx.doi.org/10.1088/1475-7516/2010/08/001.
[28] T. D. Brandt, "Constraints on MACHO dark matter from compact stellar systems in ultra-faint dwarf galaxies", *The Astrophysical Journal Letters* **824** no. 2, (Jun, 2016) L31. https://dx.doi.org/10.3847/2041-8205/824/2/L31.
[29] S. Dodelson and L. M. Widrow, "Sterile neutrinos as dark matter", *Phys. Rev. Lett.* **72** (Jan, 1994) 17–20. https://link.aps.org/doi/10.1103/PhysRevLett.72.17.
[30] G. Steigman and M. S. Turner, "Cosmological Constraints on the Properties of Weakly Interacting Massive Particles", *Nucl. Phys. B* **253** (1985) 375–386.
[31] L. Roszkowski, E. M. Sessolo, and S. Trojanowski, "Wimp dark matter candidates and searches—current status and future prospects", *Reports on Progress in Physics* **81** no. 6, (May, 2018) 066201. http://dx.doi.org/10.1088/1361-6633/aab913.
[32] H.-C. Cheng, J. L. Feng, and K. T. Matchev, "Kaluza-Klein Dark Matter", *Phys. Rev. Lett.* **89** (Oct, 2002) 211301. https://link.aps.org/doi/10.1103/PhysRevLett.89.211301.
[33] N. Fornengo, L. Maccione, and A. Vittino, "Dark matter searches with cosmic antideuterons: status and perspectives", *JCAP* **09** (2013) 031, arXiv:1306.4171 [hep-ph].
[34] M. Cirelli, N. Fornengo, M. Taoso, and A. Vittino, "Anti-helium from Dark Matter annihilations", *JHEP* **08** (2014) 009, arXiv:1401.4017 [hep-ph].
[35] C. B. Brauninger and M. Cirelli, "Anti-deuterons from heavy Dark Matter", *Phys. Lett. B* **678** (2009) 20–31, arXiv:0904.1165 [hep-ph].
[36] A. Hryczuk, I. Cholis, R. Iengo, M. Tavakoli, and P. Ullio, "Indirect Detection Analysis: Wino Dark Matter Case Study", *JCAP* **07** (2014) 031, arXiv:1401.6212 [astro-ph.HE].
[37] P. Doetinchem *et al.*, "Cosmic-ray antinuclei as messengers of new physics: Status and outlook for the new decade", *Journal of Cosmology and Astroparticle Physics* **2020** (08, 2020) 035–035.
[38] A. W. Strong, I. V. Moskalenko, and V. S. Ptuskin, "Cosmic-ray propagation and interactions in the galaxy", *Annual Review of Nuclear and Particle Science* **57** no. Volume 57, 2007, (2007) 285–327. https://www.annualreviews.org/content/journals/10.1146/annurev.nucl.57.090506.123011.
[39] M. Potgieter, "Solar Modulation of Cosmic Rays", *Living Reviews in Solar Physics* **10** (06, 2013) .
[40] L. J. Gleeson and W. I. Axford, "Solar Modulation of Galactic Cosmic Rays", *Astrophysical Journal* **154** (Dec, 1968) 1011.
[41] A. W. Labrador and R. A. Mewaldt, "Effects of Solar Modulation on the Low-Energy Cosmic-Ray Antiproton/Proton Ratio", *The Astrophysical Journal* **480** no. 1, (May, 1997) 371. https://dx.doi.org/10.1086/303960.
[42] M. Boschini, S. Della Torre, M. Gervasi, G. La Vacca, and P. Rancoita, "Propagation of cosmic rays in heliosphere: The HelMod model", *Advances in Space Research* **62** no. 10, (2018) 2859–2879. https://www.sciencedirect.com/science/article/pii/S0273117717302971. Origins of Cosmic Rays.
[43] A. W. Strong, I. V. Moskalenko, T. A. Porter, G. Jóhannesson, E. Orlando, and A. E. Vladimirov, "Galprop version 54 : Explanatory supplement", 2011. https://api.semanticscholar.org/CorpusID:131769805.

[44] I. V. Moskalenko, A. W. Strong, J. F. Ormes, and M. S. Potgieter, "Secondary Antiprotons and Propagation of Cosmic Rays in the Galaxy and Heliosphere", *The Astrophysical Journal* **565** no. 1, (Jan, 2002) 280. https://dx.doi.org/10.1086/324402.

[45] H. Fuke *et al.*, "Search for cosmic-ray antideuterons", *Phys. Rev. Lett.* **95** (2005) 081101, arXiv:astro-ph/0504361.

[46] **BESS** Collaboration, K. Sakai *et al.*, "Search for Antideuterons of Cosmic Origin Using the BESS-Polar II Magnetic-Rigidity Spectrometer", *Phys. Rev. Lett.* **132** no. 13, (2024) 131001.

[47] K. Abe *et al.*, "Search for antihelium with the bess-polar spectrometer", *Physical Review Letters* **108** no. 13, (Mar., 2012) . http://dx.doi.org/10.1103/PhysRevLett.108.131301.

[48] M. Boezio *et al.*, "PAMELA and indirect dark matter searches", *New Journal of Physics* **11** no. 10, (Oct, 2009) 105023. https://dx.doi.org/10.1088/1367-2630/11/10/105023.

[49] **PAMELA** Collaboration, O. Adriani *et al.*, "Ten years of PAMELA in space", *Riv. Nuovo Cim.* **40** no. 10, (2017) 473–522, arXiv:1801.10310 [astro-ph.HE].

[50] **Fermi LAT** Collaboration, M. Ackermann and et. al., "Measurement of Separate Cosmic-Ray Electron and Positron Spectra with the Fermi Large Area Telescope", *Phys. Rev. Lett.* **108** (Jan, 2012) 011103. https://link.aps.org/doi/10.1103/PhysRevLett.108.011103.

[51] **AMS** Collaboration, M. Aguilar *et al.*, "First Result from the Alpha Magnetic Spectrometer on the International Space Station: Precision Measurement of the Positron Fraction in Primary Cosmic Rays of 0.5–350 GeV", *Phys. Rev. Lett.* **110** (Apr, 2013) 141102. https://link.aps.org/doi/10.1103/PhysRevLett.110.141102.

[52] I. V. Moskalenko *et al.*, "Challenging Cosmic-Ray Propagation with Antiprotons: Evidence for a "Fresh" Nuclei Component?", *The Astrophysical Journal* **586** no. 2, (Apr, 2003) 1050. https://dx.doi.org/10.1086/367697.

[53] M. Simon, A. Molnar, and S. Roesler, "A New Calculation of the Interstellar Secondary Cosmic-Ray Antiprotons", *The Astrophysical Journal* **499** no. 1, (May, 1998) 250. https://dx.doi.org/10.1086/305606.

[54] F. Donato *et al.*, "Antiprotons from Spallations of Cosmic Rays on Interstellar Matter", *The Astrophysical Journal* **563** no. 1, (Dec, 2001) 172. https://dx.doi.org/10.1086/323684.

[55] V. S. Ptuskin, I. V. Moskalenko, F. C. Jones, A. W. Strong, and V. N. Zirakashvili, "Dissipation of Magnetohydrodynamic Waves on Energetic Particles: Impact on Interstellar Turbulence and Cosmic-Ray Transport", *The Astrophysical Journal* **642** no. 2, (May, 2006) 902. https://dx.doi.org/10.1086/501117.

[56] **AMS** Collaboration, "The AMS-02 Experiment website", 2025. https://ams02.space.

[57] **AMS** Collaboration, L. Accardo *et al.*, "High Statistics Measurement of the Positron Fraction in Primary Cosmic Rays of 0.5–500 GeV with the Alpha Magnetic Spectrometer on the International Space Station", *Phys. Rev. Lett.* **113** (Sep, 2014) 121101. https://link.aps.org/doi/10.1103/PhysRevLett.113.121101.

[58] **AMS** Collaboration, M. Aguilar *et al.*, "Towards Understanding the Origin of

Cosmic-Ray Positrons", *Phys. Rev. Lett.* **122** (Jan, 2019) 041102. https://link.aps.org/doi/10.1103/PhysRevLett.122.041102.

[59] S. Ting, "The first five years of the alpha magnetic spectrometer on the international space station.",. https://indico.cern.ch/event/592392/.

[60] R. A. Ong *et al.*, "The GAPS Experiment to Search for Dark Matter using Low-energy Antimatter", 2017. https://arxiv.org/abs/1710.00452.

[61] M. Kozai, "The GAPS experiment – a search for cosmic-ray antinuclei from dark matter", *Journal of Physics: Conference Series* **1468** no. 1, (Feb, 2020) 012049. https://dx.doi.org/10.1088/1742-6596/1468/1/012049.

[62] **GAPS** Collaboration, N. Saffold *et al.*, "Cosmic antihelium-3 nuclei sensitivity of the GAPS experiment", *Astropart. Phys.* **130** (2021) 102580, arXiv:2012.05834 [hep-ph].

[63] **GAPS** Collaboration, F. Rogers *et al.*, "Sensitivity of the GAPS experiment to low-energy cosmic-ray antiprotons", *Astropart. Phys.* **145** (2023) 102791, arXiv:2206.12991 [astro-ph.HE].

[64] R. Calabrese, "Signatures from primordial black hole evaporation", *Journal of Physics: Conference Series* **2429** no. 1, (Feb, 2023) 012033. https://dx.doi.org/10.1088/1742-6596/2429/1/012033.

[65] A. Andronic, A. Andronic, K. Redlich, *et al.*, "Decoding the phase structure of QCD via particle production at high energy", *Nature* **561** (2018) 321–330.

[66] V. Vovchenko, B. Dönigus, and H. Stoecker, "Multiplicity dependence of light nuclei production at LHC energies in the canonical statistical model", *Phys. Lett. B* **785** (2018) 171–174, arXiv:1808.05245 [hep-ph].

[67] S. T. Butler and C. A. Pearson, "Deuterons from High-Energy Proton Bombardment of Matter", *Phys. Rev.* **129** (Jan, 1963) 836–842. https://link.aps.org/doi/10.1103/PhysRev.129.836.

[68] J. I. Kapusta, "Mechanisms for deuteron production in relativistic nuclear collisions", *Phys. Rev. C* **21** (Apr, 1980) 1301–1310. https://link.aps.org/doi/10.1103/PhysRevC.21.1301.

[69] W. Greiner, S. Schramm, and E. Stein, *Quantum Chromodynamics*. Springer Berlin, Heidelberg, 12, 2006.

[70] J. N. Guenther, "Overview of the QCD phase diagram", *The European Physical Journal A* **57** (2021) 136. https://doi.org/10.1140/epja/s10050-021-00354-6.

[71] J. Rafelski, "Connecting QGP-Heavy Ion Physics to the Early Universe", *Nuclear Physics B - Proceedings Supplements* **243** (06, 2013) .

[72] A. Bazavov, H.-T. Ding, P. Hegde, O. Kaczmarek, F. Karsch, N. Karthik, E. Laermann, A. Lahiri, R. Larsen, S.-T. Li, S. Mukherjee, H. Ohno, P. Petreczky, H. Sandmeyer, C. Schmidt, S. Sharma, and P. Steinbrecher, "Chiral crossover in qcd at zero and non-zero chemical potentials", *Physics Letters B* **795** (2019) 15–21. https://www.sciencedirect.com/science/article/pii/S0370269319303223.

[73] A. Chodos, R. L. Jaffe, K. Johnson, C. B. Thorn, and V. F. Weisskopf, "New extended model of hadrons", *Phys. Rev. D* **9** (Jun, 1974) 3471–3495. https://link.aps.org/doi/10.1103/PhysRevD.9.3471.

[74] M. Miller, K. Reygers, S. Sanders, and P. Steinberg, "Glauber modeling in high-energy nuclear collisions", *Annual Review of Nuclear and Particle Science* **57**

no. 1, (Nov, 2007) 205–243. http://dx.doi.org/10.1146/annurev.nucl.57.090506.123020.

[75] **ALICE** Collaboration, S. Acharya *et al.*, "The ALICE experiment: a journey through QCD", *Eur. Phys. J. C* **84** no. 8, (2024) 813, arXiv:2211.04384 [nucl-ex].

[76] "Evolution of collisions and QGP". https://particlesandfriends.wordpress.com/2016/10/14/evolution-of-collisions-and-qgp/. Particles and friends - Wordpress.

[77] U. W. Heinz, "Concepts of heavy ion physics", in *2nd CERN-CLAF School of High Energy Physics*, pp. 165–238. 7, 2004. arXiv:hep-ph/0407360.

[78] F. Becattini, "An introduction to the statistical hadronization model", 2009. https://arxiv.org/abs/0901.3643.

[79] R. Hagedorn, "Statistical thermodynamics of strong interactions at high energies", *Nuovo Cimento, Suppl.* **3** (1965) 147–186. https://cds.cern.ch/record/346206.

[80] G. Brown, J. Stachel, and G. Welke, "Pions from resonance decay in Brookhaven relativistic heavy-ion collisions", *Physics Letters B* **253** no. 1, (1991) 19–22. https://www.sciencedirect.com/science/article/pii/037026939191356Z.

[81] **HotQCD** Collaboration, A. Bazavov, T. Bhattacharya, C. DeTar, H.-T. Ding, S. Gottlieb, R. Gupta, P. Hegde, U. M. Heller, F. Karsch, E. Laermann, L. Levkova, S. Mukherjee, P. Petreczky, C. Schmidt, C. Schroeder, R. A. Soltz, W. Soeldner, R. Sugar, M. Wagner, and P. Vranas, "Equation of state in $(2+1)$-flavor QCD", *Phys. Rev. D* **90** (Nov, 2014) 094503. https://link.aps.org/doi/10.1103/PhysRevD.90.094503.

[82] S. Borsanyi, Z. Fodor, J. N. Guenther, R. Kara, S. D. Katz, P. Parotto, A. Pasztor, C. Ratti, and K. K. Szabó, "Qcd crossover at finite chemical potential from lattice simulations", *Phys. Rev. Lett.* **125** (Jul, 2020) 052001. https://link.aps.org/doi/10.1103/PhysRevLett.125.052001.

[83] V. Vovchenko and H. Stoecker, "Analysis of hadron yield data within hadron resonance gas model with multi-component eigenvolume corrections", *J. Phys. Conf. Ser.* **779** no. 1, (2017) 012078, arXiv:1610.02346 [nucl-th].

[84] T. Umeda, S. Aoki, S. Ejiri, T. Hatsuda, K. Kanaya, H. Ohno, and Y. Maezawa, "Equation of state in 2+1 flavor QCD with improved Wilson quarks by the fixed scale approach", *Phys. Rev. D* **85** (May, 2012) 094508. https://link.aps.org/doi/10.1103/PhysRevD.85.094508.

[85] A. Andronic, P. Braun-Munzinger, J. Stachel, and H. Stocker, "Production of light nuclei, hypernuclei and their antiparticles in relativistic nuclear collisions", *Phys. Lett. B* **697** (2011) 203–207, arXiv:1010.2995 [nucl-th].

[86] V. Vislavicius and A. Kalweit, "Multiplicity dependence of light flavour hadron production at LHC energies in the strangeness canonical suppression picture", arXiv:1610.03001 [nucl-ex].

[87] F. Becattini, "A Thermodynamical approach to hadron production in e+ e- collisions", *Z. Phys. C* **69** no. 3, (1996) 485–492.

[88] V. Vovchenko, B. Dönigus, and H. Stoecker, "Canonical statistical model analysis of pp, p–Pb, and Pb–Pb collisions at energies available at the CERN Large Hadron Collider", *Phys. Rev. C* **100** no. 5, (2019) 054906, arXiv:1906.03145 [hep-ph].

[89] V. Vovchenko, M. I. Gorenstein, and H. Stoecker, "Finite resonance widths influence the thermal-model description of hadron yields", *Phys. Rev. C* **98** no. 3, (2018) 034906, arXiv:1807.02079 [nucl-th].

[90] V. Vovchenko and H. Stoecker, "Thermal-fist: A package for heavy-ion collisions and hadronic equation of state", *Computer Physics Communications* **244** (Nov, 2019) 295–310. http://dx.doi.org/10.1016/j.cpc.2019.06.024.

[91] P. Koch, B. Müller, and J. Rafelski, "Strangeness in relativistic heavy ion collisions", *Physics Reports* **142** no. 4, (1986) 167–262. https://www.sciencedirect.com/science/article/pii/0370157386900967.

[92] J. Rafelski, "Strange anti-baryons from quark-gluon plasma", *Physics Letters B* **262** no. 2, (1991) 333–340. https://www.sciencedirect.com/science/article/pii/037026939191576H.

[93] **ALICE** Collaboration, S. Acharya *et al.*, "Multiplicity dependence of (anti-)deuteron production in pp collisions at $\sqrt{s} = 7$ TeV", *Phys. Lett. B* **794** (2019) 50–63, arXiv:1902.09290 [nucl-ex].

[94] **ALICE** Collaboration, J. Adam *et al.*, "${}^{3}_{\Lambda}\mathrm{H}$ and ${}^{3}_{\Lambda}\overline{\mathrm{H}}$ production in Pb-Pb collisions at $\sqrt{s_{\mathrm{NN}}} = 2.76$ TeV", *Phys. Lett. B* **754** (2016) 360–372, arXiv:1506.08453 [nucl-ex].

[95] **ALICE** Collaboration, S. Acharya *et al.*, "Measurement of deuteron spectra and elliptic flow in Pb–Pb collisions at $\sqrt{s_{\mathrm{NN}}} = 2.76$ TeV at the LHC", *Eur. Phys. J. C* **77** no. 10, (2017) 658, arXiv:1707.07304 [nucl-ex].

[96] R. Scheibl and U. W. Heinz, "Coalescence and flow in ultrarelativistic heavy ion collisions", *Phys. Rev. C* **59** (1999) 1585–1602, arXiv:nucl-th/9809092.

[97] F. Bellini and A. P. Kalweit, "Testing production scenarios for (anti-)(hyper-)nuclei and exotica at energies available at the cern large hadron collider", *Physical Review C* **99** no. 5, (May, 2019) . http://dx.doi.org/10.1103/PhysRevC.99.054905.

[98] A. Shebeko, P. Papakonstantinou, and E. Mavrommatis, "The one-body and two-body density matrices of finite nuclei with an appropriate treatment of the center-of-mass motion", *The European Physical Journal A* **27** no. 2, (Feb., 2006) 143–155. http://dx.doi.org/10.1140/epja/i2005-10247-3.

[99] J. L. Nagle, B. S. Kumar, D. Kusnezov, H. Sorge, and R. Mattiello, "Coalescence of deuterons in relativistic heavy ion collisions", *Phys. Rev. C* **53** (Jan, 1996) 367–376. https://link.aps.org/doi/10.1103/PhysRevC.53.367.

[100] F. Bellini, K. Blum, A. P. Kalweit, and M. Puccio, "Examination of coalescence as the origin of nuclei in hadronic collisions", *Phys. Rev. C* **103** no. 1, (2021) 014907, arXiv:2007.01750 [nucl-th].

[101] Z. Zhang and C. M. Ko, "Hypertriton production in relativistic heavy ion collisions", *Physics Letters B* **780** (2018) 191–195. https://www.sciencedirect.com/science/article/pii/S0370269318301904.

[102] K.-J. Sun, C. M. Ko, and B. Dönigus, "Suppression of light nuclei production in collisions of small systems at the large hadron collider", *Physics Letters B* **792** (May, 2019) 132–137. http://dx.doi.org/10.1016/j.physletb.2019.03.033.

[103] R. Hanbury Brown and R. Q. Twiss, "A Test of a new type of stellar interferometer on Sirius", *Nature* **178** (1956) 1046–1048.

[104] K. Blum, K. C. Y. Ng, R. Sato, and M. Takimoto, "Cosmic rays, antihelium, and an old navy spotlight", *Phys. Rev. D* **96** no. 10, (2017) 103021, arXiv:1704.05431

[astro-ph.HE].

[105] S. E. Koonin, "Proton Pictures of High-Energy Nuclear Collisions", *Phys. Lett. B* **70** (1977) 43–47.

[106] **ALICE** Collaboration, B. Abelev *et al.*, "Charged kaon femtoscopic correlations in *pp* collisions at $\sqrt{s}$=7 TeV", *Phys. Rev. D* **87** (Mar, 2013) 052016. https://link.aps.org/doi/10.1103/PhysRevD.87.052016.

[107] V. Vovchenko, K. Gallmeister, J. Schaffner-Bielich, and C. Greiner, "Nucleosynthesis in heavy-ion collisions at the LHC via the Saha equation", *Phys. Lett. B* **800** (2020) 135131, arXiv:1903.10024 [hep-ph].

[108] V. Vovchenko and V. Koch, "Centrality dependence of proton and light nuclei yields as a consequence of baryon annihilation in the hadronic phase", *Phys. Lett. B* **835** (2022) 137577, arXiv:2210.15641 [nucl-th].

[109] **CERN** Collaboration, "The CERN website", 2025. https://www.home.cern/science/accelerators/accelerator-complex. The accelerator-complex page.

[110] **ALICE** Collaboration, S. Acharya *et al.*, "ALICE upgrades during the LHC Long Shutdown 2", *JINST* **19** no. 05, (2024) P05062, arXiv:2302.01238 [physics.ins-det].

[111] G. Aglieri Rinella, "The ALPIDE pixel sensor chip for the upgrade of the ALICE Inner Tracking System", *Nuclear Instruments and Methods in Physics Research Section A: Accelerators, Spectrometers, Detectors and Associated Equipment* **845** (2017) 583–587. https://www.sciencedirect.com/science/article/pii/S0168900216303825. Proceedings of the Vienna Conference on Instrumentation 2016.

[112] W. Snoeys, "CMOS monolithic active pixel sensors for high energy physics", *Nuclear Instruments and Methods in Physics Research Section A: Accelerators, Spectrometers, Detectors and Associated Equipment* **765** (2014) 167–171. https://www.sciencedirect.com/science/article/pii/S0168900214008596. HSTD-9 2013 - Proceedings of the 9th International "Hiroshima" Symposium on Development and Application of Semiconductor Tracking Detectors.

[113] S. Senyukov, J. Baudot, *et al.*, "Charged particle detection performances of CMOS pixel sensors produced in a 0.18μm process with a high resistivity epitaxial layer", *Nuclear Instruments and Methods in Physics Research Section A: Accelerators, Spectrometers, Detectors and Associated Equipment* **730** (2013) 115–118. https://www.sciencedirect.com/science/article/pii/S0168900213002945. Proceedings of the 9th International Conference on Radiation Effects on Semiconductor Materials Detectors and Devices.

[114] **ALICE** Collaboration, B. Abelev *et al.*, "Technical Design Report for the Upgrade of the ALICE Inner Tracking System", tech. rep., 2014. https://cds.cern.ch/record/1625842.

[115] **ALICE** Collaboration, B. Abelev *et al.*, "Upgrade of the ALICE Time Projection Chamber", tech. rep., 2013. https://cds.cern.ch/record/1622286.

[116] "CERN EP-DT-DD Micro-Pattern Technologies", tech. rep. https://ep-dep-dt.web.cern.ch/micro-pattern-technologies.

[117] A. Akindinov, A. Alici, P. Antonioli, S. Arcelli, Y. Baek, M. Basile, G. Cara Romeo, L. Cifarelli, F. Cindolo, A. De Caro, D. De Gruttola, S. De Pasquale,

M. Fusco Girard, C. Guarnaccia, D. Hatzifotiadou, H. Jung, W. Jung, D. Kim, D. Kim, H. Kim, J. Kim, S. Kiselev, G. Laurenti, K. Lee, S. Lee, M. Luvisetto, D. Malkevich, A. Margotti, R. Nania, A. Nedosekin, F. Noferini, P. Pagano, A. Pesci, R. Preghenella, G. Russo, M. Ryabinin, E. Scapparone, G. Scioli, A. Silenzi, M. Tchoumakov, K. Voloshin, M. Williams, B. Zagreev, C. Zampolli, and A. Zichichi, "Construction and tests of the mrpc detectors for tof in alice", *Nuclear Instruments and Methods in Physics Research Section A: Accelerators, Spectrometers, Detectors and Associated Equipment* **602** no. 3, (2009) 658–664. https://www.sciencedirect.com/science/article/pii/S0168900208019578. Proceedings of the 9th International Workshop on Resistive Plate Chambers and Related Detectors.

[118] D. Falchieri, "DRM2: the Readout Board for the ALICE TOF Upgrade", *PoS* **TWEPP-17** (2018) 081.

[119] M. Slupecki, "The Fast Interaction Trigger for the ALICE Upgrade", 2020. https://cds.cern.ch/record/2741462. Presented 12 Jun 2020.

[120] H. M. Rytkonen, "Event plane determination with the new ALICE FIT detector", *PoS* **ICHEP2020** (2021) 814.

[121] M. Slupecki, "Fast Interaction Trigger for ALICE upgrade", *Nuclear Instruments and Methods in Physics Research Section A: Accelerators, Spectrometers, Detectors and Associated Equipment* **1039** (2022) 167021. https://www.sciencedirect.com/science/article/pii/S0168900222004466.

[122] B. M. *et al.*, "A systematic study to characterize fine-mesh PMTs in high magnetic fields", *Nuclear Instruments and Methods in Physics Research Section A: Accelerators, Spectrometers, Detectors and Associated Equipment* **572** no. 1, (2007) 465–467. https://www.sciencedirect.com/science/article/pii/S016890020602153X. Frontier Detectors for Frontier Physics.

[123] **ALICE** Collaboration, S. Evdokimov, "Diffraction physics with ALICE at the LHC", in *30th International Workshop on High Energy Physics: Particle and Astroparticle Physics, Gravitation and Cosmology: Predictions, Observations and New Projects*, pp. 83–90. 2015. arXiv:1412.7300 [hep-ex].

[124] **ALICE** Collaboration, A. Villatoro Tello, "AD, the ALICE diffractive detector", *AIP Conf. Proc.* **1819** no. 1, (2017) 040020.

[125] **ALICE** Collaboration, S. Acharya *et al.*, "Future high-energy pp programme with ALICE",. https://cds.cern.ch/record/2724925.

[126] P. Buncic, M. Krzewicki, and P. Vande Vyvre, "Technical Design Report for the Upgrade of the Online-Offline Computing System",.

[127] **ALICE** Collaboration, S. Acharya *et al.*, "The ALICE Transition Radiation Detector: construction, operation, and performance", *Nucl. Instrum. Meth. A* **881** (2018) 88–127, arXiv:1709.02743 [physics.ins-det].

[128] L. Rolandi, W. Riegler, and W. Blum, *Particle detection with Drift Chambers*. Springer Berlin, Heidelberg, 08, 2008.

[129] A. Akindinov *et al.*, "Performance of the ALICE Time-Of-Flight detector at the LHC", *Eur. Phys. J. Plus* **128** (2013) 44.

[130] A. Maire, "ALICE TPC sectors and pad rows". General Photo, 2011.

[131] H. Kamada, J. Golak, K. Miyagawa, H. Witala, and W. Gloeckle, "Pi mesonic decay of the hypertriton", *Phys. Rev. C* **57** (1998) 1595–1603, arXiv:nucl-th/9709035.

[132] **A Large Ion Collider Experiment, ALICE** Collaboration, S. Acharya *et al.*, "Hypertriton Production in p-Pb Collisions at $\sqrt{s_{NN}}$=5.02 TeV", *Phys. Rev. Lett.* **128** no. 25, (2022) 252003, arXiv:2107.10627 [nucl-ex].

[133] C. Bierlich *et al.*, "A comprehensive guide to the physics and usage of PYTHIA 8.3", *SciPost Phys. Codeb.* **2022** (2022) 8, arXiv:2203.11601 [hep-ph].

[134] **GEANT4** Collaboration, S. Agostinelli *et al.*, "GEANT4–a simulation toolkit", *Nucl. Instrum. Meth. A* **506** (2003) 250–303.

[135] **ALICE** Collaboration, S. Acharya *et al.*, "Data-driven precision determination of the material budget in ALICE", *JINST* **18** no. 11, (2023) P11032, arXiv:2303.15317 [physics.ins-det].

[136] **ALICE** Collaboration, A. Calivá and I. Vorobyev, "Systematic uncertainties on (anti)(hyper)nuclei absorption - ALICE internal note". 2021.

[137] C. Tsallis, "Possible generalization of Boltzmann-Gibbs statistics", *Journal of Statistical Physics* **52** (07, 1988) 479–487.

[138] C.-Y. Wong and G. Wilk, "Tsallis Fits to p_T Spectra for pp Collisions at LHC", *Acta Phys. Polon. B* **43** (2012) 2047–2054, arXiv:1210.3661 [hep-ph].